

UNIVERSITY OF OKLAHOMA

GRADUATE COLLEGE

SPACE APPLICATION OF NOVEL SOLAR CELLS

A DISSERTATION

SUBMITTED TO THE GRADUATE FACULTY

in partial fulfillment of the requirements for the

Degree of

DOCTOR OF PHILOSOPHY

By

HADI AFSHARI
Norman, Oklahoma
2023

SPACE APPLICATION OF NOVEL SOLAR CELLS

A DISSERTATION APPROVED FOR THE
HOMER L. DODGE DEPARTMENT OF PHYSICS AND ASTRONOMY

BY THE COMMITTEE CONSISTING OF

Dr. Ian R. Sellers, Chair

Dr. Bayram Saparov

Dr. Mike Santos

Dr. Lloyd A. Bumm

Dr. Arne Schwettmann

Acknowledgments

I am deeply appreciative for the opportunity to have worked on renewable energies, specifically photovoltaic solar cells, for the past six years. This field has made a significant impact on the world, and I am grateful for the chance to contribute to its advancement.

Throughout my PhD program, I have enjoyed expanding my knowledge in science and technology. I am thankful to everyone and everything that has contributed to shaping my intellect over the past six years.

I extend my sincere gratitude to my supervisor, Prof. Ian R. Sellers, for his invaluable guidance, support, and encouragement throughout my graduate studies. His expertise and insights have played a crucial role in the successful completion of this research.

I also want to express my appreciation to the members of my committee for providing valuable feedback and suggestions that have significantly improved the quality of this work.

My colleagues and friends have provided me with unwavering support and inspiration throughout this journey. I would like to thank Shashi Sourabh, Brandon Durant, Vince Whiteside, Hamidreza Esmaeilpour, Sergio Chacon, Collin Brown, Yang Cheng, Yang Gang, Megh Khanal, Hasan Ahmed, Sethu Jayasree, Chad Cunningham, Jeo Gose, Gaurav Nirala, Jugal Talukdar, Alex Rybiki, Cinthia Pack, Ashley Price, and Deborah Schoenberger for their invaluable assistance and for always being there to listen and offer guidance.

I am grateful to the University of Oklahoma for providing the necessary resources and facilities that enabled me to complete this research.

Lastly, I want to thank my wife and daughter for their constant love and support. Their encouragement and belief in me have been an endless source of motivation and strength.

Table of Contents

List of Figures	ix
List of Tables	xiii
Abstract	xiv
Chapter 1. Introduction: Solar Energy and Solar Cells.....	1
1.1 Clean Energy.....	1
1.2 Solar Energy and the Sun’s Spectrum	2
1.3 Solar Energy the Fuel to Space Economy.....	3
1.4 Semiconductors.....	5
1.5 The p-n Junction	7
1.6 Solar Cells and Photovoltaics	8
1.6.1 First Generation Photovoltaics: Crystalline Solar Cells	8
1.6.2 Second Generation Photovoltaics: Thin Film Solar Cells	9
1.6.2I Copper Indium Gallium Diselenide (CIGS) Solar Cells	9
1.6.3 Third Generation Photovoltaics	12
1.6.3I Metal Halide Perovskite Solar Cells.....	12
1.7 Solar Cells Characterization Techniques	14
1.7.1 Current Density-Voltage (J-V) Measurements	14
1.7.2 J-V Measurements Experimental Setup.....	17
1.7.3 External Quantum efficiency (EQE) Analysis.....	18
1.7.4 EQE Measurement experimental Setup.....	19
1.7.5 Photoluminescence Spectroscopy	20
1.7.6 Photoluminescence Experimental Setup.....	20
1.8 Solar Cell Capacitance Simulator Modeling, SCAPS	21

1.9 Stopping and Range of Ions in Matter, SRIM	23
1.10 Space Environment Information System	24
1.11 References.....	24
Chapter 2. Thin Film CIGS Solar Cells for Space Applications	30
2.1 Relaxed and Metastable States of the CIGS	31
2.2 CIGS Metastability in Space Conditions	33
2.3 LILT Conditions of the Outer Planets	36
2.4 Electroluminescence of the CIGS Solar Cells	40
2.5 Concentrated Photovoltaic Measurements.....	42
2.6 Time Dependent Light Soaking Measurements.....	47
2.7 Effect of Proton Irradiation.....	48
2.8 SCAPS Simulation.....	54
2.9 Conclusions.....	57
2.10 References.....	58
Chapter 3. Electron Radiation Tolerance of GaAs _{1-x} Sb _x Solar Cells.....	63
3.1 Starin Management	64
3.2 Impact of Electron Irradiation on the Solar Cells	67
3.3 Change in the Pattern of the Temperature Dependent J-V	74
3.4 Performance Under LILT Conditions of the Planets	75
3.5 Conclusions.....	78
3.6 References.....	79
Chapter 4. Excitons and Carrier Extraction in Perovskite Solar Cells	83
4.1 Discrepancy Between EQE and J-V Measurements.....	87
4.2 Ionization of Excitons in Temperature Dependent PL	90

4.3 Ionization of Excitons in Temperature Dependent EQE	95
4.4 Comparing Ionization of Excitons Observed in PL and EQE	96
4.5 Temperature Dependence of the Exciton Binding Energy	97
4.6 Conclusions.....	99
4.7 References.....	99
Chapter 5. High Temperature Stability of FACsPb(IBrCl) ₃ Perovskite Solar Cells	103
5.1 Solar Cell Design for High Temperature Tolerance	104
5.2 High Temperature Effects Upon Photovoltaic Performance	109
5.3 Effects of High Temperature on the Radiative Emission	111
5.4 Improved Performance at High Temperature: Effect of Local Heating	113
5.5 Dependence of Absorber Thickness to High Temperature Stress	115
5.6 J-V Experiments Under More Practical Conditions	117
5.7 Assessment of the Temperature Coefficients in Perovskite Solar Cells.....	120
5.8 Conclusions.....	122
5.9 References.....	123
Chapter 6. Radiation Tolerance of FACsPb(IBrCl) ₃ Perovskite Solar Cells.....	129
6.1 Proton Irradiation of the Solar Cells with Varied Energies and Fluences	131
6.2 Elemental Analysis of the Irradiation Effect	134
6.3 Spectroscopic Analysis of the Effect of Irradiation.....	135
6.4 Self-Healing of the Irradiation-Induced Defects.....	137
6.5 Marginal Non-Radiative Recombination Centers Seen in the Dark J-V	141
6.6 A High Temperature Study of the Irradiated Solar Cells	142
6.7 Thermal Activation of the Irradiation Induced Defects.....	144
6.8 Conclusions.....	145

6.9 References	146
Summary and Outlook	151
List of Publications	154

List of Figures

Fig. 1.1 Sun spectrum on the ground AM 1.5, and at the top of the atmosphere	3
Fig. 1.2 N-type, intrinsic and p-type semiconductor	6
Fig. 1.3 Schematic of a p-n junction showing different regions including neutral p and n regions and depletion region designated with D.....	7
Fig. 1.4 Structure of the CIGS solar cell showing all the constituent layers	10
Fig. 1.5 The band diagram of the CIGS solar cell	12
Fig. 1.6 Typical structure of a perovskite solar cell.....	13
Fig. 1.7 Dark and light J-V graph of the solar cell showing important points on the light curve related to the PV parameters	16
Fig. 1.8 An actual image of the J-V measurement set up showing Sun simulator, reference cell, temperature controller and the mounting stage.....	18
Fig. 1.9 An actual image of the EQE measurement set up showing monochromator, detector, temperature controller and the mounting stage.....	19
Fig. 1.10 An actual image of the PL system	21
Fig. 1.11 SCAPS user interface	23
Fig. 2.1 An Example of the crossover of dark and light J-V graphs.....	32
Fig. 2.2 V_{OC} and FF values extracted from J-V experiments.....	35
Fig. 2.3 Comparison of the relaxed and metastable states in the CIGS solar cells using J-V measurements.....	39
Fig. 2.4 Current injection dependent electroluminescence at temperatures (a) 80 K, (b) 100 K, (c) 263 K and (d) 300 K	41
Fig. 2.5 Temperature dependent electroluminescence.....	42
Fig. 2.6 Concentration dependent J-V measurements of CIGS solar cells in the relaxed and metastable states.....	44
Fig. 2.7 V_{OC} and PCE values extracted from CPV measurements.....	46
Fig. 2.8 Time dependent light soaking effect on the J-V measurements	48

Fig. 2.9 Light J-V of the Reference and irradiated samples under LILT conditions of planets	50
Fig. 2.10 Comparing the EQE of the reference and irradiated samples	52
Fig. 2.11 Stopping and range of ions in matter (SRIM), simulating the trajectories of protons in the CIGS solar cell	53
Fig. 2.12 The Structure of the CIGS solar cell and the SCAPS simulation of the structure	54
Fig. 2.13 Grading profile of the CIGS absorber band gap via tuning Ga and In composition factors.....	55
Fig. 2.14 Effect of irradiation illustrated via Comparison of the PV experiments and SCAPS simulations	56
Fig. 3.1 Schematic illustration of the structure of the GaAsSb based solar cell.....	65
Fig. 3.2 Simulated energy band alignments for the structure	66
Fig. 3.3 Temperature dependent PL of the solar cell before and after irradiation.....	70
Fig. 3.4 J-V and EQE of the GaAs _{1-x} Sb _x solar cell before and after electron irradiation at (a) 80 K and 300 K.....	71
Fig. 3.5 Temperature dependent J-V before and after irradiation.....	74
Fig. 3.6 J-V and EQE measurements before and after irradiation at temperatures of the planets Saturn, Jupiter, and Mars	77
Fig. 4.1 Structure and energy band alignment of the Perovskite solar cell	85
Fig. 4.2 J-V response as a function of temperature accompanied with Diagrammatic representations of the extraction of charge carriers	86
Fig. 4.3 EQE and J-V measured between 90 K and 300 K with two different illumination intensities	88
Fig. 4.4 Light J-V of the Cs _{0.05} FA _{0.79} MA _{0.16} Pb(I _{0.83} Br _{0.17}) ₃ perovskite solar cell at 150 K under low and high illumination intensities.....	89
Fig. 4.5 The photoluminescence of the solar cell as a function of temperature	90
Fig. 4.6 Temperature dependent dark J-V of the solar cell from 85 K up to 300 K.....	93
Fig. 4.7 Heat map of the temperature dependent photoluminescence	94
Fig. 4.8 The normalized EQE of the solar cell at 77 K and 300 K.....	95

Fig. 4.9 Comparison of the EQE at the absorption edge with PL.....	96
Fig. 4.10 Arrhenius analysis using PL-integrated intensity and J_{sc}	97
Fig. 5.1 Schematic of perovskite solar cell and its J-V performance	105
Fig. 5.2 J-V data from three batches of the solar cells studied for over 18 months.....	107
Fig. 5.3 Temperature dependent J-V measurements for the FACsPb(IBrCl) ₃ solar cell from 300 K up to 490 K.....	109
Fig. 5.4 Temperature dependence of the remaining factors for PV parameters	110
Fig. 5.5 Power dependent photoluminescence at 295 K.....	112
Fig. 5.6 Plot of the remaining factors for room temperature PV parameters post heating	113
Fig. 5.7 Dark J-V of FACsPb(IBrCl) ₃ solar cell before heating and after exposure to 490 K	115
Fig. 5.8 Temperature dependent J-V from 300 K up to 490 K for an optimized FACsPb(IBrCl) ₃ perovskite solar cell with a 400 nm absorber layer.....	116
Fig. 5.9 Temperature dependent external quantum efficiency for FACsPb(IBrCl) ₃ between 300 K and 490 K.....	117
Fig. 5.10 Temperature dependent J-V from 300 K to 490 K under constant illumination at 1-Sun AM 1.5G, holding the cell at V_{oc} and J_{sc} between scans	118
Fig. 5.11 Temperature dependence of the temperature coefficient between 350 K and 490 K...121	
Fig. 6.1 Schematics of different types of stresses imposed on the perovskite solar cell	131
Fig. 6.2 Trajectory of the protons in the perovskite solar cells.....	132
Fig. 6.3 SRIM simulated estimation of the density of vacancies.....	134
Fig. 6.4 Comparison of the normalized PL of the traveler cell and irradiated cells	136
Fig. 6.5 The remaining factor of PV parameters as a function of energy of protons	138
Fig. 6.6 Light J-V plot of the solar cells irradiated with high energy protons.....	139
Fig. 6.7 The dark J-V graph of FACsPb(IBrCl) ₃ perovskite solar cells pre-irradiation , right after irradiation and two months after irradiation	141
Fig. 6.8 Temperature dependent light J-V plot of FACsPb(IBrCl) ₃ solar cell irradiated with high energy protons.....	143

Fig. 6.9 Comparison of the remaining factors of PV parameters as a function of temperature ..144

List of Tables

Table 2.I. Intensity, temperature, relaxed and metastable V_{OC} and FF values for the CIGS solar cell in the LILT conditions of each planet.....	58
Table 2.II. Intensity, temperature, relaxed and metastable V_{OC} and FF values for the CIGS solar cell in the LILT conditions of each planet.....	79
Table 5.I. presenting temperature coefficient of various solar cell technologies. The temperature coefficient of the triple halide perovskite solar cell at three temperatures also included to compare with other technologies	14

Abstract

Multiple solar cell technologies from three different generations of photovoltaic cells were studied for space applications. The GaAsSb, crystalline first-generation solar cells were studied under low-intensity-low-temperature (LILT) space conditions. In order to examine performance of the cells in energetic irradiation environments this system was exposed to electron irradiation of 1 MeV. Improvement in the carrier extraction was observed in short wavelength regime in the external quantum efficiency (EQE) measurements after electron irradiation. Transmission electron microscope (TEM) images indicated enhanced crystallinity near the top of the cells, coinciding with the region that short wavelength incident light is absorbed. The Cu(InGa)Se₂ (CIGS), thin film second generation solar cells were studied under space LILT conditions. These conditions included low Sun intensity at the outer planets in the solar system and their respective temperatures. The unencapsulated CIGS cells were irradiated with 1.5 MeV protons of varying fluence, resulting in significant damage to the performance of the cells. The damage rooted in irradiation induced defects which diffused toward the grain boundaries and resulted in reduced shunt resistance. The degradation manifested more pronounced at low temperatures of the outer planets. A Fresnel lens concentrating system was suggested for the CIGS solar cells to compensate for low light intensity of the outer planets. This concentrating system has a remarkable effect on improving the efficiency of the cells at the planets with dim conditions. Multiple structures of the perovskite solar cells, third generation photovoltaics, were studied in extreme space conditions of irradiation and temperature. Proton irradiation induced defect states inside the perovskite solar cells compromised the performance of the cells. Although, after two months of keeping samples in the dark we observed self-healing in the perovskite cells, resulting in performance of the cells to become very similar to the pre-irradiation conditions. We observed

that for irradiation with 1 MeV and extreme fluence level of 4×10^{14} (1/cm²) the solar cell stopped functioning after a few months. Through modifications in architecture of the FACsPb(I₂BrCl)₃ solar cells, very high temperature, 490 K (217 °C), performance of the perovskite solar cells was achieved with 70% of the room temperature efficiency. The modifications to the FACsPb(I₂BrCl)₃ perovskite solar cell included: First, use of a double cation (FACs) composition which improves the stability of the perovskite absorber layer. Second, a transparent conductive back contact was used to prevent metal migration or iodine-metal corrosion. Finally, an alumina-based nanolaminate was applied on top of the cell to prevent thermal decomposition due to loss of volatile species. The investigation of these solar cell technologies under extreme space conditions resulted in finding the weak points and also hidden capacities of these systems. In the case of CIGS solar cells grain boundaries facilitate shunting after irradiation. In perovskite solar cells aside from the stability problem, samples showed very high radiation tolerance and extremely good performance at temperatures more than 200 °C.

Chapter 1

Introduction. Solar Energy and Solar Cells

1.1 Clean Energy

Given the strong link between carbon dioxide levels in the atmosphere and atmospheric temperature, reducing carbon emissions is now considered a crucial factor in modern industry. Over the last century, industrial activities have caused atmospheric carbon dioxide levels to rise from 280 ppm to more than 400 ppm [1, 2]. Although renewable energy's contribution to the power sector has risen in recent years, most of our electricity still comes from traditional non-renewable sources, such as oil and coal, which cause environmental damage. Therefore, utilizing modern, renewable and clean energy sources that replenish themselves becomes crucial in reducing our impact on the environment [3]. Furthermore, renewable energy resources offer greater energy security compared to fossil fuels.

Solar power may be the only clean energy option that can provide a major portion of our future's energy consumption, as it has the largest resource compared to other renewables [4]. The Earth receives close to 173,000 TWh of energy from the Sun every hour through electromagnetic radiation. In this regard the main solar energy harvest technology, photovoltaics, has come a long way over more than half a century, evolving from a technology mainly used to power satellites in space to one that is commonly used to power every day activities on the ground [4].

1.2 Solar Energy and the Sun's Spectrum

The radiation emitted by the Sun closely resembles that of a black body radiator with a temperature of approximately 5,800 K [1]. During sunlight's journey through the atmosphere, various chemicals interact with the sunlight, leading to the absorption of specific wavelengths of light. This process alters the amount of light that eventually reaches the Earth's surface. Water vapor plays a particularly active role in this process, generating numerous absorption bands across a wide range of wavelengths, while molecular nitrogen, oxygen, and carbon dioxide also contribute to this phenomenon. The air mass coefficient (AM) indirectly shows the amount of attenuation of light reaching earth. In practice, mass coefficient does this by considering the angle of incident light and calculating the different path lengths illuminations travel in the atmosphere. The air mass can be calculated using the following equation, where the θ is the angle between the position of the Sun and the normal vector of the ground at any location [5, 6]:

$$AM = \frac{1}{\cos \theta} \cdot \quad (1)$$

Another important function of the air mass coefficient is to define the illumination standards for photovoltaic tests. To ensure a fair comparison between solar cells measured at different times and locations, it is crucial to consider variations in both the power and spectrum of the incident light, as these factors can significantly impact a solar cell's efficiency. Therefore, a standard spectrum and power density have been established for radiation outside the Earth's atmosphere and at the Earth's surface.

Above the atmosphere the standard Sun spectrum is shown by AM0 with an intensity of close to 1.361 kW/m^2 . At the Earth's surface, the standard spectrum is referred to as AM1.5G, with an

intensity of about 1 kW/m^2 . Figure 1 illustrates the spectrum of direct sunlight at AM0 and AM1.5 and compares it with the radiation distribution of a blackbody at 6000 K.

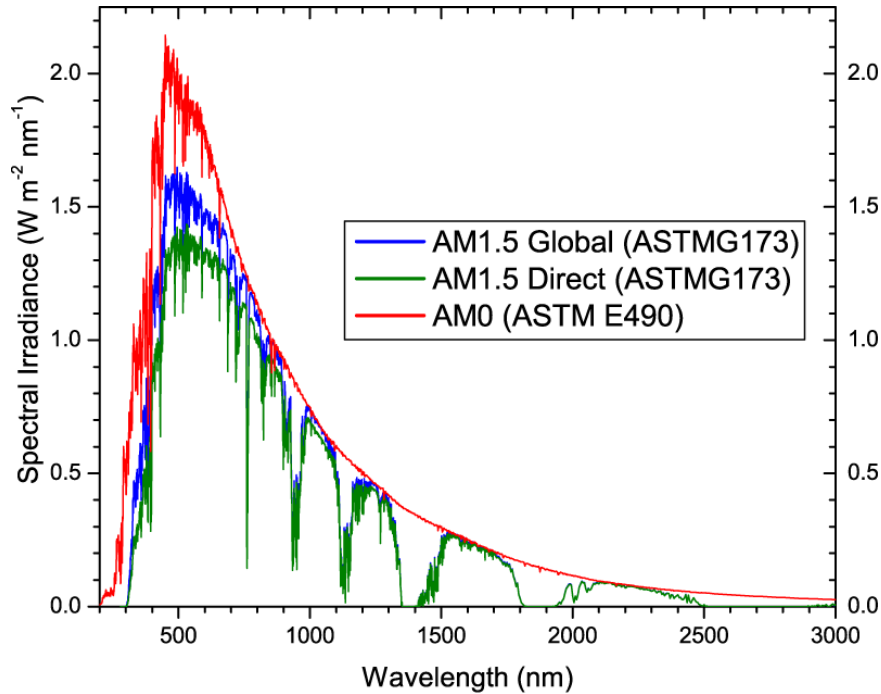


Figure 1. Sun spectrum on the ground including AM 1.5 Global shown with blue color and AM 1.5 Direct spectrum presented with green color. The Sun spectrum at the top of the atmosphere is shown with red [7].

1.3 Solar Energy, the Fuel to Space Economy

In the present day, our lives heavily rely on satellites. These orbiting objects enable us to use navigation apps such as Google Maps, access television programs, mobile services, and receive up-to-the-minute weather updates. These are just a few of the concrete benefits that satellites offer us. In addition, satellites play a crucial role in monitoring climate change, making them one of the most essential tools at our disposal. The space economy, which generated over \$400 billion in revenue in 2020, owes much of its success to satellites, which serve as the foundation of this rapidly growing sector. We have now fully entered the commercial space age. So, how do

satellites generate power in the vastness of space? The answer is through the use of solar panels and solar energy [8, 9].

With the advancement and increased efficiency of solar panels, the number of satellites orbiting the Earth is very rapidly increasing. From the inception of the space satellite industry, photovoltaic solar energy has been the primary source of power for spacecraft. Silicon solar cells were initially used in space applications, despite their limitations, such as lower efficiencies and significant radiation damage. The III-V materials opened up the path for enhancement of cells using multiple-junction solar cells. A successful example is the triple junction cells of GaInP/GaAs/Ge layers on a Germanium base, the most used cell structure for space applications [10, 11].

To improve properties of solar panels for space applications efforts are not only focused on III-V crystalline materials, but there is also important research testing alternative systems such as perovskites [12] and other thin film technologies [13]. The unique properties of perovskite solar cells including their high specific power and tunable band gap, make them a promising system for space applications [12]. In the thin film category CIGS solar cells represent a novel thin solar cell for space use, an alternative to the higher fabrication costs of III-V solar cells [13-16].

The dependability of photovoltaic devices is vital for their use in space environments. In this regard, it is necessary to run accelerated lifetime testing of the cells in space conditions. For space solar panels, it is necessary to adhere to standard procedures for qualification for different space missions. The American Institute of Aeronautics (AIAA) has established guidelines for this purpose AIAA S-111 and AIAA S-112A, which defines the quality requirements for space solar cells and related electrical parts [17-20].

1.4 Semiconductors

Semiconductors are the base of all modern electronic devices. They can be elemental, such as silicon (Si) or complex compounds like copper indium gallium diselenide (CIGS). In these material systems, a periodic potential produces energy bands [21]. As the temperature increases, electrons gain energy and their probability to occupy higher energy continuum states increases, as described by the Fermi-Dirac distribution $f(E)$:

$$f(E) = \frac{1}{e^{(E-E_F)/kT} + 1}. \quad (2)$$

Where k is Boltzmann's constant, E is the energy of an electron, and T the absolute temperature. The bands in a semiconductor are occupied until they reach the Fermi energy (E_F), which is the energy level where the probability of an electron occupying a state is 50% at equilibrium. In semiconductors, the bandgap (E_g) is defined as the energy difference between the maximum of the valence band (E_v) and minimum of the conduction (E_c) band. When an energy greater than or equal to E_g is incident on the semiconductor, an electron is excited into the conduction band, where it can freely move and create a current (in presence of an electric field), leaving behind an empty energy state known as a hole. Holes carry a charge opposite to that of an electron and exist only as an electron vacancy [21].

The position of the Fermi level with respect to the conduction and valence bands determines the conductivity of a material. When the conduction and valence bands overlap, facilitating easy current conduction, we have a metal or conductor. When the Fermi level is between the valence and conduction energy bands, the material is a semiconductor. When the band gap is very large preventing the transition of electrons between the bands, we have an insulator. By introducing dopant (impurity) concentrations, the Fermi energy level can be changed, [21, 22]. When the

impurity atoms are added to the semiconductor material, they replace some of the atoms in the crystal lattice. A semiconductor material becomes p-type when it is doped with impurity atoms that have fewer valence electrons than the host semiconductor atoms. The Fermi energy level in a p-type semiconductor is closer to the valence band. Similarly, a semiconductor material becomes n-type when it is doped with impurity atoms that have excess valence electrons than the host semiconductor atoms. The Fermi energy level in a n-type semiconductor is closer to the conduction band. [21, 22]. Figure 2 illustrates the two types of semiconductors next to an intrinsic semiconductor which is not doped.

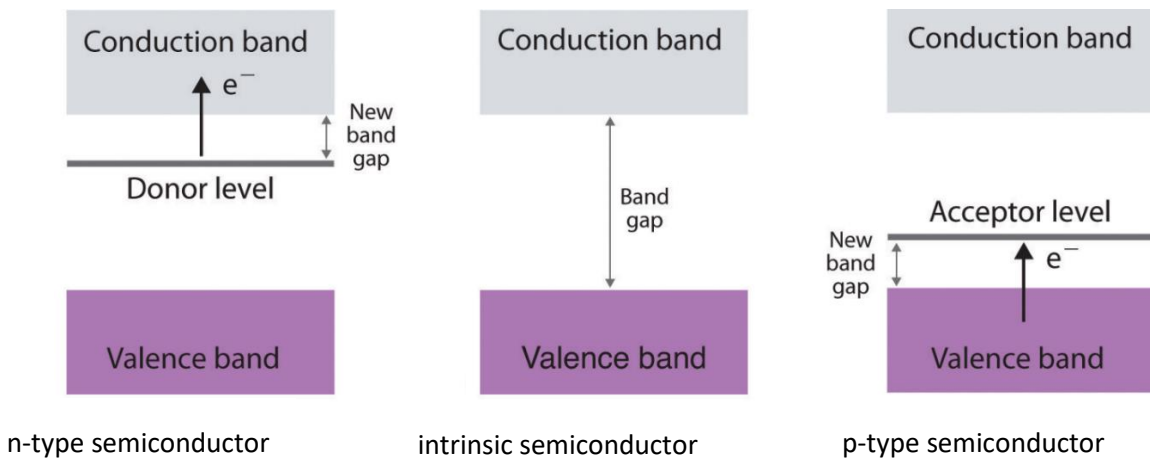


Figure. 2. From left to right n-type, intrinsic and p-type semiconductor. The figure shows donor and acceptor energy levels due to doping of the semiconductor [23].

The concentration of either electrons or holes in the semiconductor depends on the effective density of states, and temperature, and is expressed as:

$$n = N_c e^{(E_F - E_C)/kT} . \tag{3}$$

and

$$p = N_v e^{(E_v - E_F)/kT} . \quad (4)$$

Here N_V and N_C are the effective density of states for valence and conduction band respectively [21, 22].

1.5 The p-n Junction

When a p-n junction is formed by bringing together n-type and p-type systems, a large charge density gradient is created across the junction. Then the excess electrons from the n-type material diffuse to the p-type material, and vice versa for holes. During this process, the migrating electrons leave behind positively charged ions in the n-type side of the junction, while the migrating holes expose negatively charged atoms on the p-type side of the junction. As a result, an electric field is established (known as a built-in potential) that counteracts the diffusion of the electrons and holes, leading to an equilibrium state (see Figure 3). This creates an area near the p-n junction depleted from free charge carriers referred to as the depletion region as shown in the Figure 3 below [21, 24].

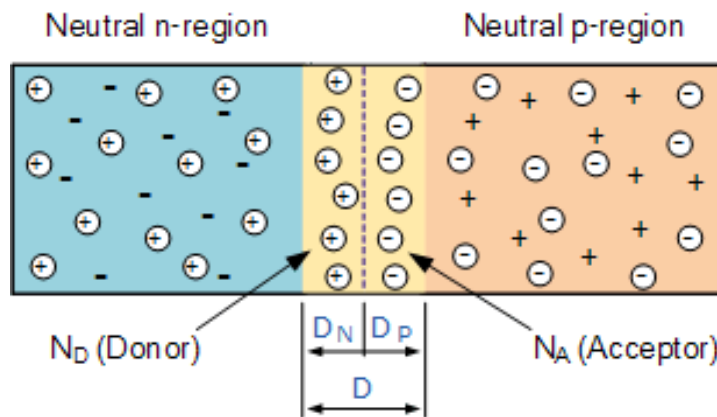


Figure 3. Schematic of a p-n junction showing different regions including neutral p and n regions and depletion region designated with D. The Depleted region in p side is D_p and in n side it is shown as D_n [25].

1.6 Solar Cells and Photovoltaics

The process of direct generation of electricity from solar radiation or light is photovoltaics (PV). Solar cells convert sunlight to electricity based on the photovoltaic effect. Typically, a solar cell contains a p-n junction using the light absorbing semiconductor materials that are matched to the solar spectrum. When solar radiation is absorbed by a semiconducting material, an electron is excited to the conduction band, leaving behind a hole in the valance band. In some semiconductors, the electrons and holes are Coulombically bound, which is called exciton. The excitons can be ionized into separate electrons and holes, which then can be collected at the electrodes to generate electricity. In recent decades, a wide range of PV technologies and materials have been introduced. PV technologies can be classified into different classes based on the materials and structural design [26, 27].

1.6.1 First Generation Photovoltaics: Crystalline Solar Cells

Photovoltaic technologies were initially based on highly purified crystalline materials such as Silicon (c-Si). This generation of the cells suffered from high production cost and low absorption coefficient in the case of Si, since Si is an indirect band gap material. Despite these limitations, c-Si has dominated the PV industry for decades, with improved cell size and production processes developed and implemented on an enormous scale. In 2018, silicon wafer-based technology accounted for over 90% of the PV market. In addition to c-Si, inorganic semiconductors with a direct band gap, such as GaAs, GaAlAs, GaInAsP, InSb, and InP, are also used in solar cells. GaAs is commonly used in concentrator modules and space-industry due to its high heat resistance, and high cell efficiency, compared to Si solar cells. However, the

material cost and manufacturing process of GaAs-based materials can be expensive compared to Si-based solar cells [28, 29].

1.6.2 Second Generation PV: Thin-Film Solar Cells

The second generation of solar cells is the thin-film technology, which can be flexible while utilizing thin layers to absorb incident solar radiation with less absorber material [30]. The main reason behind the development of thin-film solar cells was to reduce production costs by using less absorber material and less energy intensive production processes [30]. Some of the main thin-film solar cells are (CdTe), copper indium selenide (CIS), and copper indium gallium diselenide (CIGS) based solar cells [30, 31].

1.6.2.I Copper Indium Gallium Diselenide (CIGS) Solar Cells

$(\text{Cu}(\text{In}, \text{Ga}, \text{Al})(\text{Se}, \text{S})_2)$, compounds known as CIGS have tunable bandgaps ranging from 1 eV (CuInSe_2) to 3 eV (CuAlS_2), and very high absorption coefficient. The absorber layer in CIGS can be fabricated through techniques such as co-evaporation, and electro-deposition. The CIGS-based solar cells are formed from stacked thin layers deposited on a substrate. The constituent layers are molybdenum (Mo) electrode, CIGS absorber, CdS as buffer layer, and electrode (ZnO:Al) as another electrode, see figure 4. An extra MoSe_2 layer (not shown in the structure) forming naturally in the back contact interface is the main reason Mo is chosen for the back contact since the MoSe_2 helps the formation of an ohmic layer between CIGS and Mo facilitating collection of the carriers at this end. Since these basic layers and their functionality is more or less similar for most of solar cells (not the material but the role that each layer serves), here each layer is introduced separately [13, 32, 33].

Figure 4 shows the typical structure of a CIGS solar cell. These systems comprise a significant portion of the research described in this thesis, and their role in the performance and degradation of this type of cell is critical to understanding their potential for space applications. As such the architectures of these CIGS devices are considered more comprehensively below.

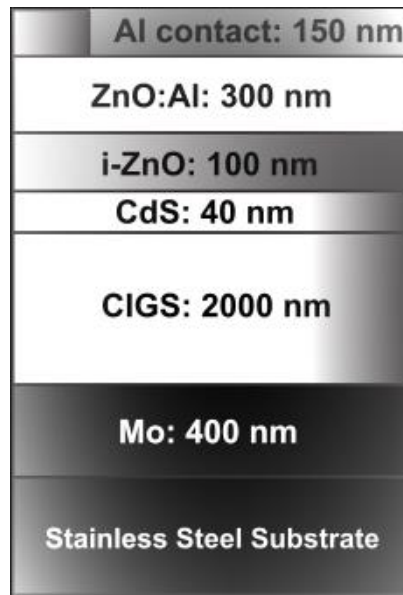


Figure 4. Structure of the CIGS solar cell showing all the constituent layers.

Substrate: The insulating Soda-lime glass is typically the preferred substrate for reasons including: stability needed to tolerate deposition of next layers. Its thermal expansion coefficient is close to CIGS material. More recently advanced CIGS cells use flexible stainless steel substrates [33].

Molybdenum back contact: deposited onto a glass substrate, serves as the back electrode and is responsible for collecting the carriers. A highly conductive interfacial layer of MoSe₂ between Mo and CIGS helps the extraction of carriers from this electrode [32].

CIGS absorber layer: CIGS is typically a p-type semiconductor, with high doping concentration resulting from defects such as copper vacancies. Changing the composition factor of the Gallium and Indium allows tuning of the band gap for this system between 1.014 eV (CIS) and 1.697 eV (CGS). Aside from the deposition techniques, what makes CIGS suitable for thin category is the high absorption coefficient and the direct band gap which is optimized around 1.2 eV. This makes it possible to harvest most of incident Sun radiation with a 2-micrometer layer of the CIGS absorber material [32, 33].

The buffer layer CdS: CdS buffer layer commonly deposited through a chemical bath serves as the n-type side in the p-n heterojunction solar cells between the CIGS and CdS. This heterojunction facilitates the drift of electron and hole towards the respective contacts, while also improving the quality of the CIGS through passivating surface defects on the absorber [13, 32, 33].

Window layer iZnO/ZnO:Al: Deposited through sputtering, the dual-layer stack of intrinsic zinc oxide and aluminum-doped zinc oxide forms the upper electrode acting as a window or surface passivation layer and serves to exert force on electron and hole towards desired contacts [33].

Band structure of CIGS: Figure 5 [19] shows the band structure of the typical architecture of a CIGS solar at the junction. the figure shows acceptor and donor states specifically accumulating at CIGS/CdS interface. The ($V_{Cu} - V_{Se}$) divacancy defects shown in the figure have been suggested to cause metastability in performance of these cells [33].

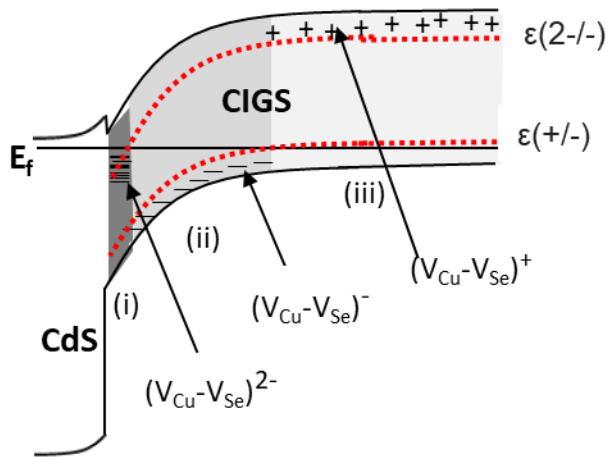


Figure 5. The band diagram of the CIGS solar cell showing the band offsets at the CIGS/CdS interface and bending in the junction region.

1.6.3 Third Generation Photovoltaics

Third-generation photovoltaics encompasses a wide range of protocols, such as multi-junction concentrating PV and emerging PV technologies that require further basic research and development such as hot carrier solar cells [24] or quantum dot intermediate band devices [24]. These emerging technologies often use innovative techniques and materials to achieve PV material properties that can be highly suitable for solar energy harvest. Some of these properties are tunable band, ultra-high absorption coefficient, and ambipolar charge transport. Some of the emerging technologies include inorganic semiconducting quantum dot cells, organic cells, and organic-inorganic hybrid perovskite cells [27].

1.6.3I Metal Halide Perovskite Solar Cells

Figure 6 depicts the typical device configuration of a perovskite solar cell, which comprises a metal halide perovskite layer sandwiched between an electron transporting layer (ETL, which is designed to collect electrons while blocking holes) and a hole transporting layer (HTL, designed

to collect holes and block electrons). Perovskite solar cell research follows the same pattern of finding novel direct band gap materials with high absorption coefficient reducing the photovoltaic materials and production cost of the solar cells. In addition to these features, solution-based deposition techniques allow a faster industrial scale production of these systems. The very thin layer of perovskite is enable to absorb almost all the incident light creating electron and hole pairs, which are then transported via charge transport layers to the respective electrodes [34].

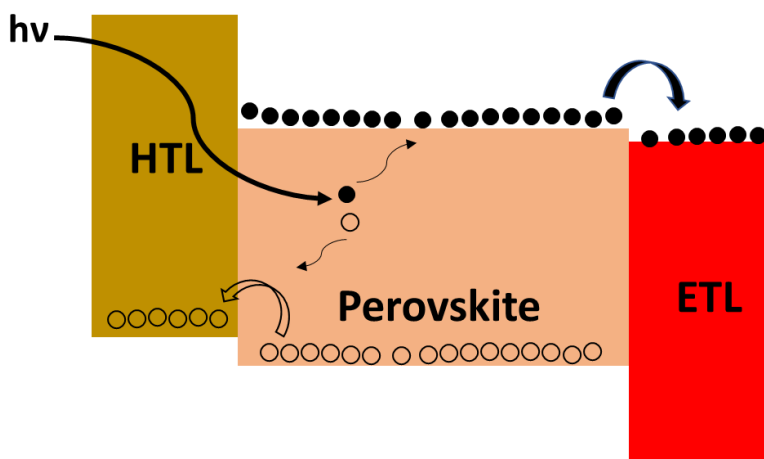


Figure 6. Typical structure of a perovskite solar cell. After absorbing photons by the perovskite absorber layer electron-hole pairs are generated. The electrons and holes are then collected at the electron transport and hole transport layer, respectively.

In terms of efficiency, perovskite solar cells have reached close to their practical limit in a very short time. Although, the investment on Perovskite solar cells is much higher compared to the early silicon solar cells. The short history of perovskite solar cells is very informative about this technology and evolution of the structure and the role of the constituent layers *and* interfaces. Their history starts with replacement of lead halide for dye molecules in dye-sensitized solar cells in 2006 [32,33]. The next cell was a liquid based solar cell with an electrolyte bath for

charge separation. In 2009, the first paper on halide perovskites in solar cells, reported an efficiency of about 4% [35, 36].

In the 2010 decade the perovskite community exploded in terms of quality of research and number of researchers. This led to progress in all aspects of perovskite solar cell design and materials. Various architecture, materials and composition factors were tested for the constituent elements of the perovskite layer. Numerous transporting layers were introduced/investigated. The outcomes were multiple successful transport layers such as spiro-MeOTAD, polymeric poly(triarylamine) (PTAA) and electron transport layers such as SnO₂ and TiO₂. The efficiency of the perovskite solar cells in 2020 had already passed 20% with improvements in stability and fabrication techniques. Today, the efficiency of the perovskite cells are more than 25% and it continues to improve [35, 36].

1.7 Solar Cell Characterization Techniques

1.7.1 Current Density-Voltage (J-V) Measurements

As discussed in the introduction, photovoltaics refers to the production of an electric current and voltage in a material upon exposure to sunlight. The basic structure of a solar cell is the p-n junction, which creates a built-in electric potential forcing minority electrons and holes towards the intended electrodes. When photons are absorbed by the solar cell, electrons are stimulated into a higher-energy state (conduction band in semiconductors), generating electron-hole pairs which are then extracted from the cell by means of the built-in electric field. When there is no illumination or under dark conditions, a solar cell operates like a conventional p-n diode. This means that the J-V characteristics of a solar cell can be interpreted using the diode equation [6]:

$$I_{dark}(V) = I_0 \left[\exp\left(\frac{qv}{k_B T}\right) - 1 \right]. \quad (5)$$

Here, k_B , T , J_0 , and are the Boltzmann constant, lattice temperature and dark saturation current density, respectively.

The illumination of the solar cell generates additional carriers that increase the flow of charge, resulting in a photogenerated current denoted as I_L . this current exists even when there is no external voltage applied ($V=0$). As a result, the diode equation used for solar cells is altered under illumination as:

$$I = I_0 \left[\exp\left(\frac{qv}{k_B T}\right) - 1 \right] - I_L \cdot \quad (6)$$

An example of the response of an I - V curve associated with the aforementioned equation/behavior is displayed in Figure 7. The shape of the diode characteristic under illumination is the same as the dark characteristic, but there is a negative shift of current as a result of the photogenerated minority current, I_L . This produces photovoltaic power generation which can be obtained using the equation [6].

$$P = I \cdot V = I_0 \left[\exp\left(\frac{qv}{k_B T}\right) - 1 \right] \cdot V - I_L \cdot V \cdot \quad (7)$$

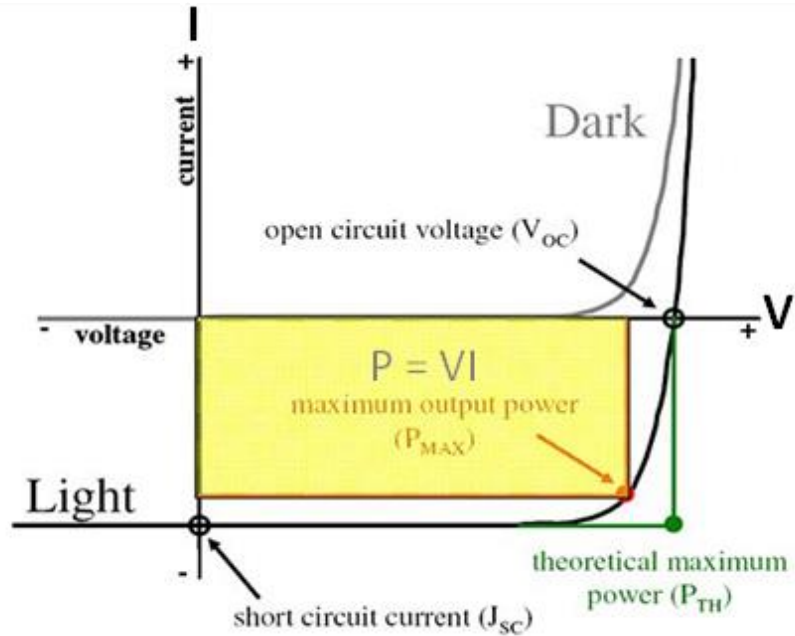


Figure 7. Dark and light J-V graph of the solar cell showing important points on the light curve related to the PV parameters of the cell [37].

Figure 7 shows the J-V results of an illuminated solar cell along with that of a dark J-V characteristics. For the illuminated cell at $V = 0$, the extracted current density is non-zero and is referred to as the short circuit current density (J_{sc}), indicating the maximum amount of current generated in the cell. As the bias voltage is increased, ideally the extracted current density remains relatively constant until a certain point, beyond which the current density drops suddenly, as the diode switches on and majority current competes with minority charge transport. Additionally, at a specific bias voltage known as the open circuit voltage (V_{oc}), the extracted current density is zero. The output power of a solar cell is determined by multiplying the maximum photocurrent density (J_{max}) with the maximum photo-voltage (V_{max}). Both at the open circuit voltage (V_{oc}), and short circuit current conditions the output power is zero. The generated power by solar cell is used in the calculation of the power conversion efficiency (PCE) as described in: [6]

$$PCE = \frac{P_{max}}{P_{in}} . \quad (8)$$

Another important parameter for solar cell electrical characterization is the fill factor (FF). The FF is calculated by dividing the maximum power (P_{max}) by the product of the J_{SC} and V_{OC} [6]

$$FF = \frac{V_{max} \cdot J_{max}}{V_{OC} \cdot J_{SC}} . \quad (9)$$

1.7.2 Current-Voltage Measurements – Experimental Setup

The PV properties of solar cells are studied with J-V measurements under the AM 1.5G (or AM0) solar spectrum, using Newport Oriel Sol2A solar simulator. The Keithley 2400 multimeter is used to provide bias to the test cells while measuring the extracted current from the device at the same time. For the temperature dependent experiments, the J-V characteristics of the solar cells are performed over a temperature range of 77 K (using liquid Nitrogen) to 350 K via a Linkam THMS600E cryostat connected to a Linkam LNP95 cooling system. An actual photo of the J-V measurement system is shown in Figure 8.

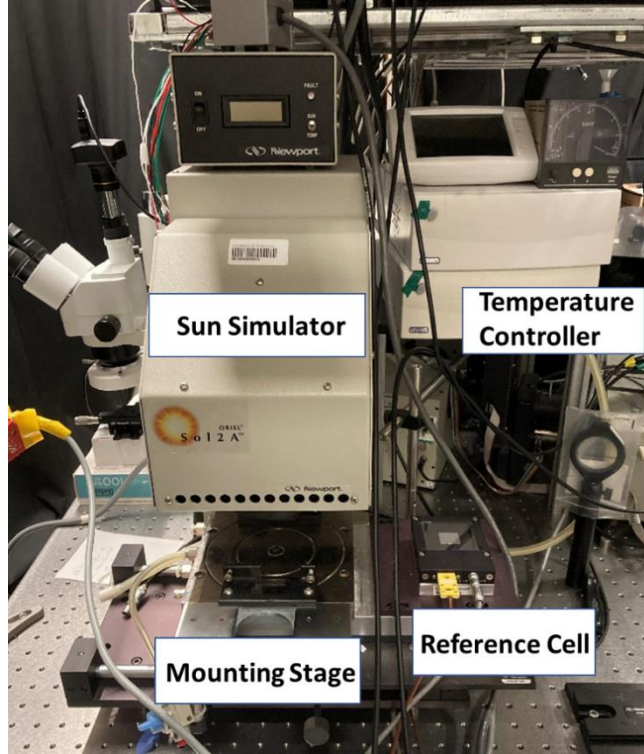


Figure 8. An actual image of the J-V measurement set up showing Sun simulator, reference cell, temperature controller and the mounting stage.

1.7.3 External Quantum Efficiency (EQE) Analysis

A standard approach used to evaluate the extracted photocurrent efficiency as a function of the wavelength of absorbed light in the solar cells is called external quantum efficiency (EQE). This technique measures the number of electrons (or holes) generated and extracted as electrical current, per photon incident on the system. Indeed, there are two versions of this parameter; internal quantum efficiency (IQE) which considers absorbed photons for calculating efficiency and External Quantum Efficiency (EQE) which considers the incident illumination on the solar cell for calculating efficiency. We use mainly EQE in this thesis which can be expressed as: [6]

$$EQE(\lambda) = \frac{\# \text{ extracted electrons}}{\# \text{ incident photons}}. \quad (10)$$

The integration of the device EQE multiplied by the incident light flux (the solar spectrum) enables the calculation of the total charge extraction under illumination (J_{sc}). In this regard, the relationship between J_{sc} and EQE is:

$$J_{sc} = q \int \Phi(\lambda) \text{EQE}(\lambda) d\lambda \cdot \quad (11)$$

Where q is coulomb charge and $\Phi(\lambda)$ is the wavelength dependent photon flux [6].

17.4 EQE Measurements – Experimental Setup

The Oriel Cornerstone 260 monochromator and Merlin digital lock-in amplifier systems are used for EQE measurements. For illumination purposes we use either a quartz tungsten halogen (QTH) lamp or a Xenon light. To measure the incident light intensity Si detector is used for the wavelength range of 300 nm to 1100 nm and Ge detector for 700 nm to 1800 nm. The temperature-dependence of EQE can be investigated from 77 K (with use of liquid nitrogen) to 350 K, using the same Linkam cryostat setup as described for J-V measurements. An actual photo of the EQE measurement system is shown in Figure 9.

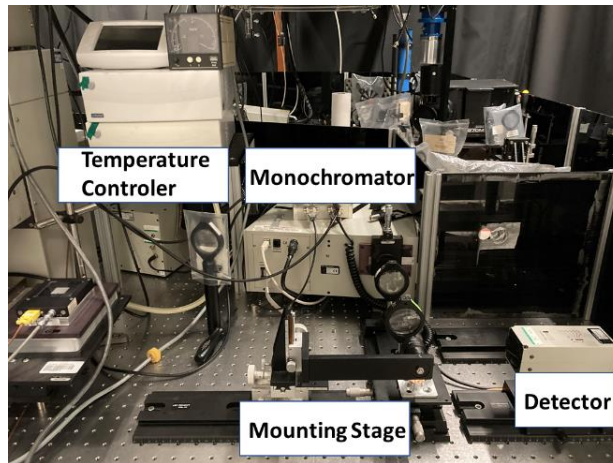


Figure 9. An image of the EQE measurement set up showing monochromator, detector, temperature controller and the mounting stage.

1.7.5 Photoluminescence Spectroscopy

When a semiconductor absorbs a photon, it excites an electron from the valence band to the conduction band (except if the energy of the photon is absorbed as heat or the electron is excited to a defect energy level). Soon after this photoexcitation, ideally the charges relax to the minimum energy level available in the conduction band at the band edge. Subsequently, electron-hole pairs may recombine radiatively emitting a photon with energy close to the band gap or non-radiatively, transferring the kinetic energy to other electrons or releasing the energy in form of heat. Detecting the emitted photon as photoluminescence (PL) and mapping it against the wavelength, therefore, offers information about the characteristics of the band gap and/or localized and defect states in a semiconductor. The power and temperature-dependent PL spectroscopy provides a comprehensive optical examination of dynamics of absorption and emission in various environments. This is crucial for understanding of the behavior of photogenerated carriers and the underlying physics in semiconductor materials and structures [38].

1.7.6 Photoluminescence - Experimental Setup

The PL of samples is mainly measured under vacuum and in very low temperatures, since most (if not all) semiconductors have brighter emission at very low temperatures. After mounting the sample into a Janis SHI-4-5 closed-cycle cryostat, a turbo molecular pump pumps down the pressure to $\sim 1 \times 10^{-5}$ torr and a helium compressor cools the sample to 4.2 K. A heater element joined with a copper cold finger controlled by a Lakeshore model 335 temperature controller is used to vary the temperature of the sample. To perform PL measurements on different semiconductor materials, lasers with different wavelengths are used depending on the band gap

of the target material. Some of the lasers used include: He-Ne lasers (632.8 nm), He-Cd lasers (325 or 442 nm), as well a 1064 nm DPSS laser. Borosilicate crown Newport lenses and borofloat mirrors are used to direct and focus the laser beam onto the cell in a cryostat. The emitted light then is directed into a Princeton Instruments Acton SP2500 spectrometer where the emission is then dispersed and detected using either an air-cooled Si charge-coupled system working in the range of 300 nm to 1100 nm, and a liquid nitrogen cooled InGaAs linear array for the range of 750 nm to 1600 nm. After proper alignment and optimizing the optical path for maximum signal acquisition, the Winspec data acquisition program is used to monitor and record the PL data. An actual photo of the photoluminescence measurement system is shown in Figure 10.

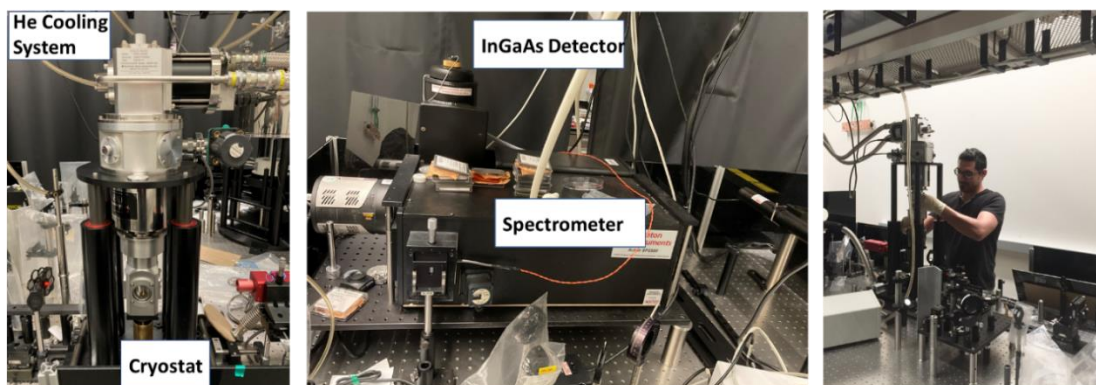


Figure 10. An image of the PL system showing Janis SHI-4-5 closed-cycle cryostat and He cooling system (left), spectrometer and InGaAs detector (middle) and the graduate student preparing the system (right).

1.8 Solar Cell Capacitance Simulator Modeling, SCAPS

To better understand the dynamics of the defect state densities and their role on the PV performance of the solar cells a solar cell capacitance simulator (SCAPS) program is used.

SCAPS is a one-dimensional solar cell simulation program developed at the University of Gent [39]. The main capabilities of the SCAPS include:

- Stacking multiple semiconductor layers forming the target solar cell,
- Model all the physical parameters required for solar cell/semiconductor simulations,
- Simulating the defect density and recombination profiles in each layer of the cell and at the interfaces,
- Modeling the work function of electrodes,
- Illumination with different spectra (AM0, AM1.5D, AM1.5G),
- Illumination of the device from front or back contact side,
- Calculate the energy band diagram, I - V curve, capacitance – voltage (C-V) curve, EQE, with temperature [39].

The SCAPS user interface is shown in Figure 11.

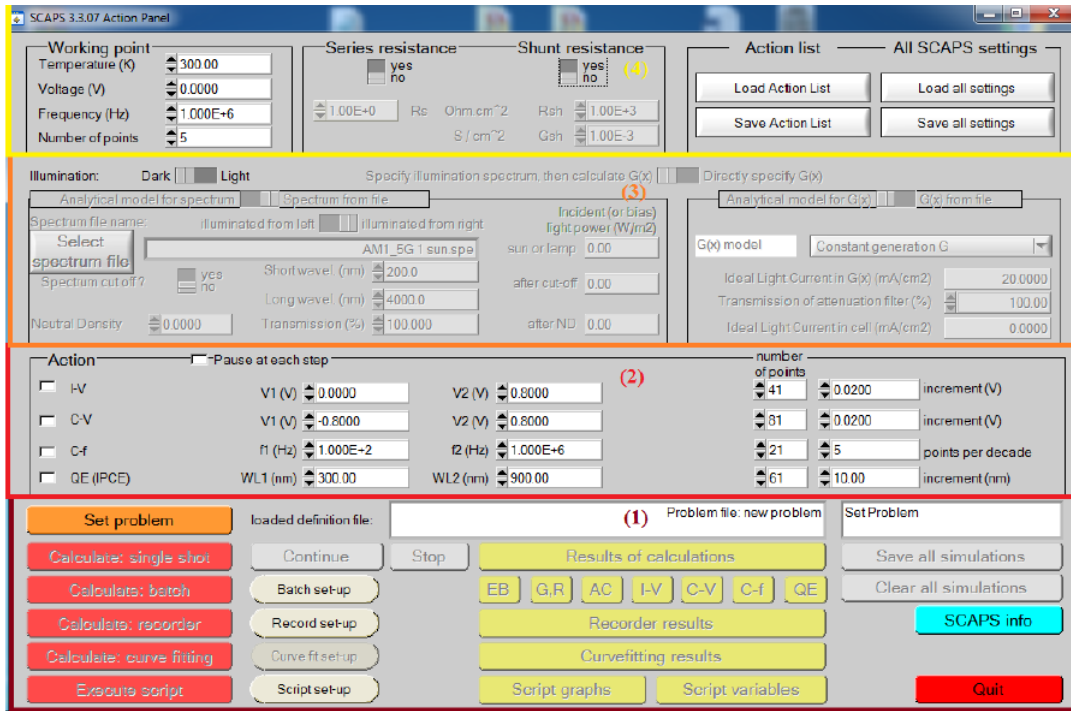


Figure 11. SCAPS interface showing 4 different panels: (1) Problem Definition Panel, (2) Action Panel, (3) Illumination Panel, and (4) Working Point Panel for simulation of solar cells.

1.9 Stopping and Range of Ions in Matter, SRIM

One of the major goals of the research described in this dissertation was to investigate the interaction between high energy particles (radiation) and solar cell materials, as well as to evaluate the radiation tolerance of various solar cell technologies. To achieve this, high energy electron and proton beams have been used to irradiate the cells in this work. To track the interactions of the incident particles with host materials and the trajectory of these particles in the system the stopping and range of ions in matter (SRIM-2013) simulation code is employed to simulate the effects of the irradiation on the cells. This code utilizes a Monte-Carlo random number generator simulation based on the binary collision approximation to model ion-solid interactions. [40] To determine the implant depth profile and estimate the total damage caused by the irradiation (including vacancies and displaced atoms), "full cascade" calculations are

performed for a large number of ions (~ 100,000). SRIM also calculates the projected range (R_p) and longitudinal straggling of the protons. Experimental tests have shown good overall agreement between SRIM predictions and experimental results for light ions (H, He), with less than a 5% error observed across all investigated targets [33]. The nuclear stopping power at low energy (20 keV and below) is a crucial factor in SRIM calculations, as low energy stopping events dominate the end-of-range stopping [40, 41].

1.10 Space Environment Information System

The Hazardous Space environment hosts many types of particles and irradiation including: solar particles, cosmic rays, and atmospheric atomic elements. There are software tools that provide information on the environment of specific orbits around the Earth and beyond in the solar system. In particular, the ESA space environment information system (SPENVIS) is one such software package that offers standardized access to models of the hazardous space environment. This software is particularly useful for radiation effects and electrostatic charging tests for hardness assurance. SPENVIS utilizes an ESA-developed orbit generator to simulate orbit conditions necessary for different types of problems, including radiation patterns, and their effects, such as nonionizing energy loss, NIEL [42-45].

1.11 References

[1] N. Unger, T.C. Bond, J.S. Wang, D.M. Koch, S. Menon, D.T. Shindell, S. Bauer, Attribution of climate forcing to economic sectors, Proceedings of the National Academy of Sciences, 107 (2010) 3382-3387.

- [2] "Sources Of Greenhouse Gas Emissions | US EPA". 2021. US EPA.
<https://www.epa.gov/ghgemissions/sources-greenhouse-gas-emissions>.
<https://climate.nasa.gov/causes/>.
- [3] "EIA - Greenhouse Gas Emissions Overview". 2021. Eia.Gov.
https://www.eia.gov/environment/emissions/ghg_report/ghg_overview.php.
- [4] N.S. Lewis, G. Crabtree, A.J. Nozik, M.R. Wasielewski, P. Alivisatos, H. Kung, J. Tsao, E. Chandler, W. Walukiewicz, M. Spittler, Basic research needs for solar energy utilization. report of the basic energy sciences workshop on solar energy utilization, April 18-21, 2005, in, DOESC (USDOE Office of Science (SC)), 2005.
- [5] M. Green, Solar cells. Kensington, N.S.W.: University of New South Wales, 1998.
- [6] J.A. Nelson, The physics of solar cells, World Scientific Publishing Company, 2003.
- [7] <https://www.pveducation.org/pvcdrom/appendices/standard-solar-spectra>.
- [8] K.W. Crane, E. Linck, B. Lal, R.Y. Wei, Measuring the space economy: Estimating the value of economic activities in and for space, in, INSTITUTE FOR DEFENSE ANALYSES ALEXANDRIA VA, 2020.
- [9] Y. Liu, Y. Zhao, C. Tan, H. Liu, Y. Liu, Economic value analysis of on-orbit servicing for geosynchronous communication satellites, Acta Astronautica, 180 (2021) 176-188.
- [10] J. Li, A. Aierken, Y. Liu, Y. Zhuang, X. Yang, J. Mo, R. Fan, Q. Chen, S. Zhang, Y. Huang, A brief review of high efficiency III-V solar cells for space application, Frontiers in Physics, 8 (2021) 631925.
- [11] T. Torchynska, G. Polupan, High efficiency solar cells for space applications, Superficies y vacío, 17 (2004) 21-25.

- [12] Y. Miyazawa, M. Ikegami, H.-W. Chen, T. Ohshima, M. Imaizumi, K. Hirose, T. Miyasaka, Tolerance of Perovskite Solar Cell to High-Energy Particle Irradiations in Space Environment, *iScience*, 2 (2018) 148-155. <https://doi.org/10.1016/j.isci.2018.03.020>
- [13] H. Afshari, B.K. Durant, C.R. Brown, K. Hossain, D. Poplavskyy, B. Rout, I.R. Sellers, The role of metastability and concentration on the performance of CIGS solar cells under Low-Intensity-Low-Temperature conditions, *Sol. Energy Mater. Sol. Cells*, 212 (2020) 110571. <https://doi.org/10.1016/j.solmat.2020.110571>
- [14] B.K. Durant, H. Afshari, S. Singh, B. Rout, G.E. Eperon, I.R. Sellers, Tolerance of Perovskite Solar Cells to Targeted Proton Irradiation and Electronic Ionization Induced Healing, *ACS Energy Lett.*, 6 (2021) 2362-2368. <https://doi.org/10.1021/acsenergylett.1c00756>
- [15] A.R. Kirmani, B.K. Durant, J. Grandidier, N.M. Haegel, M.D. Kelzenberg, Y.M. Lao, M.D. McGehee, L. McMillon-Brown, D.P. Ostrowski, T.J. Peshek, Countdown to perovskite space launch: Guidelines to performing relevant radiation-hardness experiments, *Joule*, (2022).
- [16] A.R. Kirmani, D.P. Ostrowski, K.T. VanSant, T.A. Byers, R.C. Bramante, K.N. Heinselman, J. Tong, B. Stevens, W. Nemeth, K. Zhu, I.R. Sellers, B. Rout, J.M. Luther, Metal oxide barrier layers for terrestrial and space perovskite photovoltaics, *Nature Energy*, (2023). 10.1038/s41560-022-01189-1
- [17] J. Chang, Implementation guidelines for ANSI/AIAA S-081: space systems composite overwrapped pressure vessels, in, *AEROSPACE CORP EL SEGUNDO CA VEHICLE SYSTEMS DIV*, 2003.
- [18] A. Keys, J. Adams, J. Cressler, M. Johnson, M. Patrick, A review of NASA's radiation-hardened electronics for space environments project, in: *AIAA SPACE 2008 Conference & Exposition*, 2008, pp. 7673.

- [19] A. Bermudez-Garcia, P. Voarino, O. Raccurt, Environments, needs and opportunities for future space photovoltaic power generation: A review, *Applied Energy*, 290 (2021) 116757.
- [20] O. Mourra, T. Blancquaert, C. Signorini, F. Tonicello, European Cooperation for Space Standardization-The New Standard for Electric and Electronic ECSS-E-ST-20-C, in: 8th European Space Power Conference, 2008, pp. 112.
- [21] M. Cardona, Y.Y. Peter, *Fundamentals of semiconductors*, Springer, 2005.
- [22] M. Grundmann, *Physics of semiconductors*, Springer, 2010.
- [23] <https://www.w3schools.blog/n-and-p-type-semiconductors>.
- [24] J. McCaldin, Current approaches to pn junctions in wider band gap II–VI semiconductors, *Journal of Vacuum Science & Technology A: Vacuum, Surfaces, and Films*, 8 (1990) 1188-1193.
- [25] https://www.electronics-tutorials.ws/diode/diode_2.html.
- [26] A. Khatibi, F. Razi Astarai, M.H. Ahmadi, Generation and combination of the solar cells: A current model review, *Energy Science & Engineering*, 7 (2019) 305-322.
- [27] M.A. Green, Third generation photovoltaics: solar cells for 2020 and beyond, *Physica E: Low-dimensional Systems and Nanostructures*, 14 (2002) 65-70.
- [28] S. Sharma, K.K. Jain, A. Sharma, Solar cells: in research and applications—a review, *Materials Sciences and Applications*, 6 (2015) 1145.
- [29] W.A. Badawy, A review on solar cells from Si-single crystals to porous materials and quantum dots, *Journal of advanced research*, 6 (2015) 123-132.
- [30] O. Vigil-Galán, M. Courel, J. Andrade-Arvizu, Y. Sánchez, M. Espíndola-Rodríguez, E. Saucedo, D. Seuret-Jiménez, M. Titsworth, Route towards low cost-high efficiency second generation solar cells: current status and perspectives, *Journal of Materials Science: Materials in Electronics*, 26 (2015) 5562-5573.

- [31] M.M.A. Moon, M.F. Rahman, J. Hossain, A.B.M. Ismail, Comparative study of the second generation a-Si: H, CdTe, and CIGS thin-film solar cells, *Advanced Materials Research*, 1154 (2019) 102-111.
- [32] N. Mufti, T. Amrillah, A. Taufiq, M. Diantoro, H. Nur, Review of CIGS-based solar cells manufacturing by structural engineering, *Solar energy*, 207 (2020) 1146-1157.
- [33] B. Salhi, The Photovoltaic Cell Based on CIGS: Principles and Technologies, *Materials*, 15 (2022) 1908.
- [34] R. Wang, M. Mujahid, Y. Duan, Z.K. Wang, J. Xue, Y. Yang, A review of perovskites solar cell stability, *Advanced Functional Materials*, 29 (2019) 1808843.
- [35] S.W. Lee, S. Bae, D. Kim, H.S. Lee, Historical analysis of high-efficiency, large-area solar cells: toward upscaling of perovskite solar cells, *Advanced Materials*, 32 (2020) 2002202.
- [36] S. Ito, Research Update: Overview of progress about efficiency and stability on perovskite solar cells, *APL Materials*, 4 (2016) 091504.
- [37] <http://photonicswiki.org/index.php?title=File:Pvpowergraph.jpg>.
- [38] K. Hannewald, S. Glutsch, F. Bechstedt, Theory of photoluminescence in semiconductors, *Physical Review B*, 62 (2000) 4519.
- [39] S. Degraeve, M. Burgelman, P. Nollet, Modelling of polycrystalline thin film solar cells: new features in SCAPS version 2.3, in: 3rd World Conference on Photovoltaic Energy Conversion, 2003. Proceedings of, IEEE, 2003, pp. 487-490.
- [40] J.F. Ziegler, M. Ziegler, J. Biersack, SRIM-The stopping and range of ions in matter (2010), *Nuclear Instruments and Methods in Physics Research. Section B, Beam Interactions with Materials and Atoms*, 268 (2010) 1818-1823.

- [41] S.R. Messenger, E.A. Burke, R.J. Walters, J.H. Warner, G.P. Summers, Using SRIM to calculate the relative damage coefficients for solar cells, *Progress in Photovoltaics: Research and Applications*, 13 (2005) 115-123.
- [42] S. Calders, N. Messios, E. Botek, E. De Donder, M. Kruglanski, H. Evans, D. Rodgers, Modeling the space environment and its effects on spacecraft and astronauts using SPENVIS, in: *2018 SpaceOps Conference*, 2018, pp. 2598.
- [43] D. Heynderickx, B. Quaghebeur, J. Wera, E. Daly, H. Evans, New radiation environment and effects models in the European Space Agency's Space Environment Information System (SPENVIS), *Space Weather*, 2 (2004).
- [44] R. Walters, G.P. Summers, S. Messenger, J.R. Lorentzen, T. Morton, S.J. Taylor, H. Evans, D. Heynderickx, F. Lei, SPENVIS Implementation of end-of-life solar cell calculations using the displacement damage dose methodology, in: *Proceedings of the 19th Space Photovoltaic Research and Technology Conference*, 2007.
- [45] S. Calders, N. Messios, E. De Donder, L. Hetey, M. Kuglanski, D. Heynderickx, P. Beltrami, B. Bode, N. Ho, N. Ortiz, The SPENVIS next generation, in, 2014.

Chapter 2

Thin Film CIGS Solar Cells for Space Applications

CIGS solar cell technology has been studied for decades and now offer the highest efficiency among commercially available thin film solar cells with a recent record of 23.4% [1]. The CIGS material has a direct band gap which has led to the production of thin film and flexible solar panels, which are attractive for space applications for the following points: (1) reduced specific power (power generated per mass) (2) the implementation of thin film cells will inevitably receive less radiation induced damage as a result of a smaller interaction length with incident irradiation, and (3) thin films require a significantly lower diffusion length of charge carriers for extraction, hence degradation due to irradiation is less detrimental to the solar cell performance. However, this system also has several potential issues including the quaternary composition of CIGS, which results in the low formation energy of varied defect types such as vacancies, interstitial, anti-site and other defect complexes [2, 3]. Amongst all these defects, Cu vacancies (V_{Cu}) which form shallow acceptor levels within the band gap have the lowest formation energy, hence they are the most prevalent defects in this material and define the p-type nature of this semiconductor absorber [2, 3]. Controlled stoichiometry of the elements in this system is used to tune the density of desirable defects and hence the optoelectronic properties of the system. These “engineered” defect states in CIGS are mainly shallow and relatively benign to performance of the cell at terrestrial temperatures but may have serious effects on performance of the cell when working in deep space environments with temperatures that fall below 200 K. Multiple studies have targeted the behavior of these defect states and reported a low temperature metastability in CIGS [4, 5]. The planets Jupiter and Saturn have an average orbital temperature of 100 and 135

K, respectively, which lie within the temperature range where CIGS metastability is concerning. As such, it is of paramount importance to meticulously investigate the behavior of the CIGS system in extreme LILT environments before considering them suitable for deep space applications.

2.1 Relaxed and Metastable States of the CIGS

With the goal of examining the electro-optical properties of CIGS solar cells for space applications, this work is centered on the behavior of defect energy levels when the cell is subject to the harsh LILT conditions at the outer planetary conditions of Saturn, Jupiter and Mars. CIGS solar cells have been shown to have two distinct states of operation due to a known metastability experienced by these systems when exposed to varied conditions of operation such as heating, bias, and/or illumination [6]. These relaxed and metastable states affect the photovoltaic parameters of the cell in different ways. The relaxed state is normally seen when the solar cell is left in the “dark” and at temperatures around room temperature (300K - 330K). Holding the cells in this condition for ~ 1 hour typically transitions the cell into this relaxed state condition. We can see that in practice, when CIGS solar panels are installed, they experience the relaxed state at night with no illumination. The metastable state is seen when the solar cell is in working condition i.e., by constantly illuminating the cell (day time, in the field), typically an hour of illumination with 1 Sun power (AM0 or AM1.5) at room temperature transitions the cell into the metastable mode [7, 8]. The signatures of the relaxed state in the electrical functioning of the cells include a “roll over” in the current density-voltage (J-V) measurements, which is further noticeable by a saturation in current at voltages greater than the V_{OC} , and a crossover of the dark and light in J-V responses an example of which is seen in Figure 1 [9]. In practice this can result

in lower fill factor (FF) and therefore lower power conversion efficiency (PCE) of the solar panels.

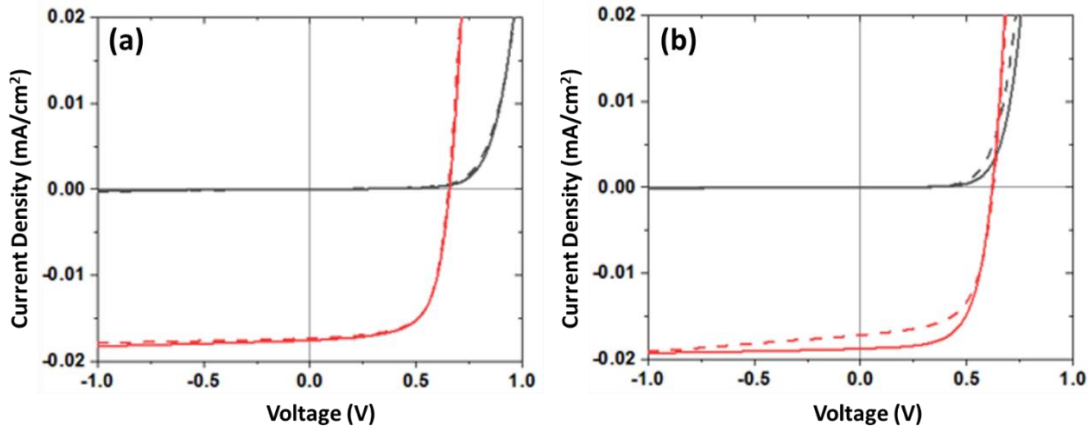


Figure 1. (a) Example of the crossover of dark and light J-V graphs (b) dark and light J-V graphs of a solar cell without the crossover effect [10].

Fortunately, these features are less problematic when the solar cells are under illumination and functioning [11]. Lany and Zunger (L-Z model) suggested a theoretical framework to describe the causes for the metastability in CIGS, and the underlying mechanisms responsible for the transition from one mode to another. The L-Z model is supported by experimental data to a good extent [7, 12]. Although this model is still debated, it explains many of the experimental outcomes observed here in this thesis, as well as the wider literature on these systems. In this model, Cu-Se divacancy complexes ($V_{Se}-V_{Cu}$), which are originally shallow donor states, convert to acceptor (shallow) configurations after constant illumination and capture of photogenerated carriers [13]. In other words, carrier generation, via illumination (i.e. light soaking), or external current injection is the primary cause for the transition between the metastable and relaxed configurations. The L-Z approach also suggests deep acceptor levels forming at the buffer/absorber interface, which also agrees with the experimental observations presented here, although in the literature some of such results are ascribed to losses at the back contact [14].

2.2 CIGS Metastability in Space Conditions

Spacecrafts that explore outer planets encounter rapid temperature fluctuations and cyclic situations of illumination and darkness. Such cycling will inevitably therefore cause transitions between the relaxed and metastable modes in the CIGS solar panels. In order to understand the effect of the transition between these modes (and their impact on photovoltaic performance), the samples were first set in the relaxed state (kept at 330 K, in the dark for 1 hour) then cooled down to 77 K, while still in the dark. In the relaxed state, deep parasitic energy levels at the CdS/CIGS interface produce features in the optoelectronic behavior of the sample (including roll-over of the light J-V curve), which allows a tracking of the dynamics of the energy levels in the samples. The samples are kept at temperature for 70 seconds, then dark and light J-V scans are performed and the PV parameters including open circuit voltage (V_{OC}) and fill Factor (FF) are extracted (Figure 2). The temperature of the cell is then raised in 10 K steps (in the dark) followed by dark and light J-V scans (black triangles Figure 2), after a dwell time of 70 s at each temperature. After reaching 310 K the experiment was repeated in the reverse direction lowering temperature in the same increments to 77 K (red squares Figure 2). The same experimental approach was repeated for the light intensity and temperature conditions of all the planetary conditions studied.

The difference in the PV parameters between the forward and reverse directions in Figure 2 is ascribed to the switching from the relaxed state (black triangles) to a metastable state (red squares) as a result of multiple light exposure cycles, and the carrier generation thereafter. For both modes of relaxed and metastable operation, the PV parameters improved significantly as the temperature decreased. At higher temperatures, activation of the defect states in the band gap manifests in an enhancement of the dark saturation current translating in lower V_{OC} . Lowering

the temperature also results in an increase of both the series and shunt resistances. Although, the relative change in shunt is more than that of the series resistance, resulting in a positive impact on device performance. The relaxed state consistently shows a higher series resistance, which is reflected in the non-monotonic behavior of the V_{OC} and FF in at low temperatures (Figure 2). Moreover, the metastable state has a higher V_{OC} at lower temperatures, when compared to the relaxed state in the reverse J-V scans (high to low temperatures). This pattern is the same for all the irradiation levels for all planetary conditions studied.

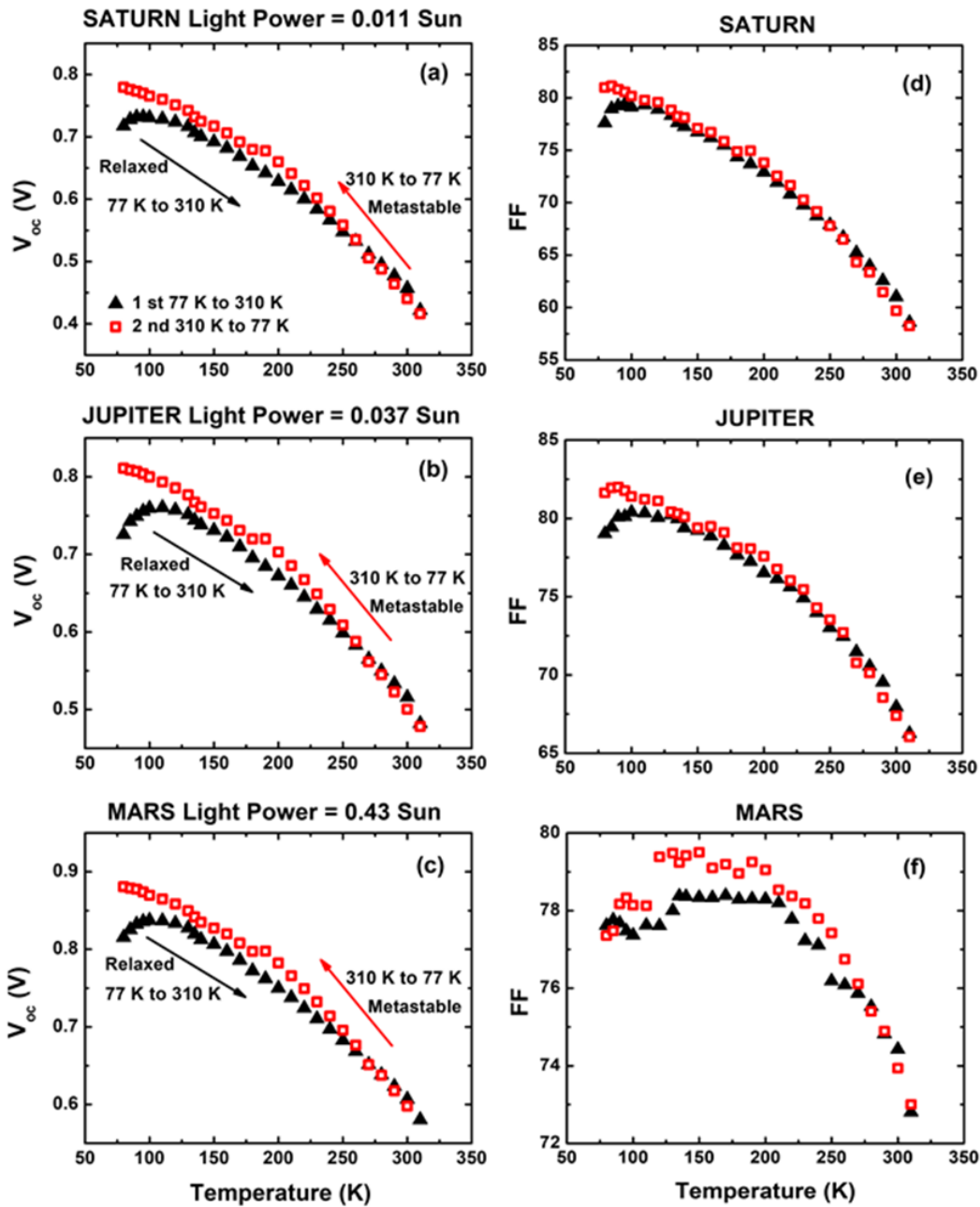


Figure 2. V_{oc} and FF values extracted from J-V experiments at the light intensities of (a, d) Saturn, (b, e) Jupiter and (c, f) Mars. The solar cells are placed in the relaxed state at 77 K and scanned to 310 K (solid black triangles), the experiment is then repeated down to 77 K (open red squares) [15].

The FF follows the same pattern (except for the case of Mars), having a higher FF for the metastable state at lower temperatures.

The emerged patterns are in qualitatively agreement with the L-Z model, in which high densities of $(V_{Se}-V_{Cu})^{2-}$ di-vacancies (traps), that act as deep acceptors are present at the CdS/CIGS interface in the relaxed state. Such defects at the CdS/CIGS interface inevitably open new channels for tunneling and recombination currents, and a simultaneous reduction of in both V_{OC} and FF, as seen in Figure 2. When extrapolating the V_{OC} -T graphs to 0 K, as shown in the Figure(s) 2(a-c), result in activation energies that are less than expected from the band gap energy. This suggests interface recombination for all excitation intensities [16, 17]. In the metastable state, the scenario is different as photogenerated carriers act to quench defects. In this mode deep trap states are occupied (through the photogenerated carriers produced via multiple light J-V scans) and consequently reconfigure and convert the defects into shallow acceptor states changing the doping profile and the properties of the interface. Particularly, saturation of the interface states and their combined effects lead to reduced shunting and higher V_{OC} and FF.

2.3 LILT Conditions of the Outer Planets

Table 1 presents the LILT conditions of the studied planetary conditions and compares the magnitude of the V_{OC} and FF in the metastable and relaxed states at those conditions. Both the values of V_{OC} and FF are lower for the relaxed state (as compared to metastable state) for Saturn and Jupiter ($T < 200$ K), while are similar for the case of Mars ($T > 200$ K). This means that at elevated temperatures the difference between the relaxed and metastable state is less significant. This effect can stem from thermally induced lattice relaxation, which creates a condition that is balanced between that of the two states [11, 13].

Table I. Intensity, temperature, relaxed and metastable V_{OC} and FF values for the CIGS solar cell in the LILT conditions of each planet.

Planet	I (AM0 Suns)	T _{eq} (K)	Relaxed		Metastable	
			V _{oc} (V)	FF	V _{oc} (V)	FF
Saturn	0.011	100	0.73	79.1	0.76	80.2
Jupiter	0.037	135	0.74	80	0.77	80.3
Mars	0.430	263	0.67	76.1	0.68	76.7

Moreover, there is also a transition in the response of the J-V curve at around 200 K in the reverse direction metastable data, which is consistent across several cells and data sets (see Figures 3(b) and (c), for example). The temperature of 200 K appears to be an important temperature regarding the dynamics of carriers in the CIGS structure. In the metastable state, at low temperatures the energy required to reconfigure the acceptor levels back into donors (according to the L-Z model) seems to be too small, or insufficient. As such the metastable state is “frozen” and a transition to the relaxed state is inhibited, resulting in improvement in performance of the solar cell. Figure 3 shows a comparison of the light and dark J-V graphs for the solar cells in the metastable and relaxed states. The lower illumination intensities for Jupiter and Saturn leads to smaller J_{SC} values as expected, while the lower temperature of these conditions leads to larger V_{OC} consistent with the expected increase in bandgap of the CIGS at low temperature. As seen, the metastable state has a bigger V_{OC} value for Jupiter and Saturn as compared to the relaxed state, while there is almost no difference between them for the conditions at Mars. A crossover in the light and dark J-V curves is also evident. Charging and discharging of the interface states leads to a non-monotonic change in the operating voltage of light and dark scans [18]. The insets in Figure 3 present the full-scale J-V response of the cells in forward bias. According to these figures the metastable state encounters a lower effective series

resistance compared to the relaxed state, which is explained by defect saturation in both the bulk absorber and at the CIGS/CdS interface. These results confirm the role of the dynamic defect states in PV performance (which are less pronounced at higher temperatures). The accumulation of deep states causes metastability in response of the CIGS solar cell. Nevertheless, relatively high efficiencies under extreme LILT conditions for Mars (14.6%), Jupiter (17.7%), and Saturn (16.2%) were observed for the relaxed state, with a slight increase to 15.2%, 19.2%, and 18.2%, respectively, for the metastable state. The room temperature efficiency of these cells was ~ 14 % at AM0 reflecting a considerable increase in performance of the CIGS under LILT conditions. This higher efficiency under LILT stems from not only the improved V_{OC} at lower temperatures, but an enhanced FF under these conditions. The efficiency results here clearly show that despite unintentional formation of deep defect energy levels at the CIGS/CdS interface, this interface is not prohibitive to the photovoltaic performance under LILT conditions [6].

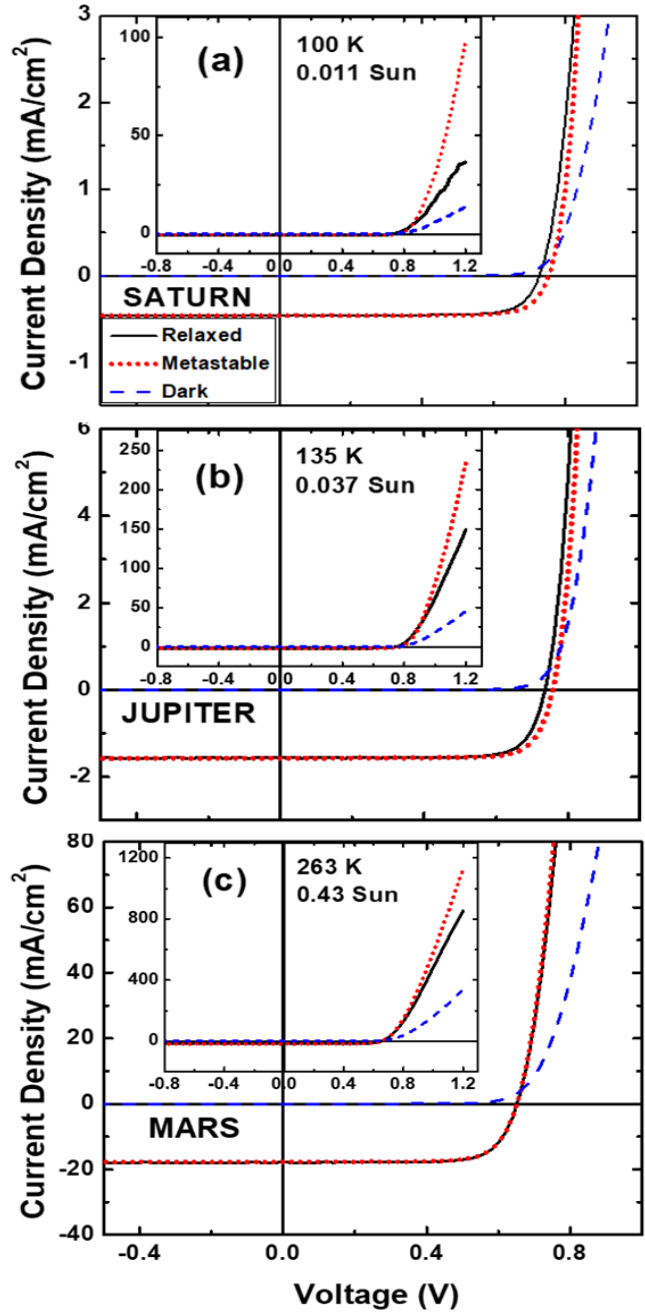


Figure 3. Comparison of the dark (blue dashed lines) and light J-V of CIGS solar cells in the relaxed (solid black lines) and metastable (red dots) configurations for conditions consistent with (a) Saturn, (b) Jupiter, and (c) Mars, respectively. Insets show the expanded graphs at the forward bias [15].

2.4 Electroluminescence of the CIGS Solar Cells

Figure 4 shows the injection dependent electroluminescence (EL) of the cells in the low and high temperature regimes. In all cases of temperature, increasing the injection creates more emission, but as seen in this figure for low temperatures (80 K and 100 K), increasing the current injection level results in a blue shift of emission as well, which does not occur at higher temperatures. It appears that defect states that are available at lower temperatures fill under injection resulting in a blue shift of the emission at $T < 200\text{K}$. According to the Moss-Burstein effect, increasing the injection levels (or increasing the excitation power in the case of photoluminescence) causes the lower energy levels in the band gap to be occupied and saturated, resulting in state filling and an evolution of the effective bandgap to higher energy. The temperature dependent EL provided further evidence for the presence and impact of defect states in CIGS on the low temperature dynamics and behavior of these systems.

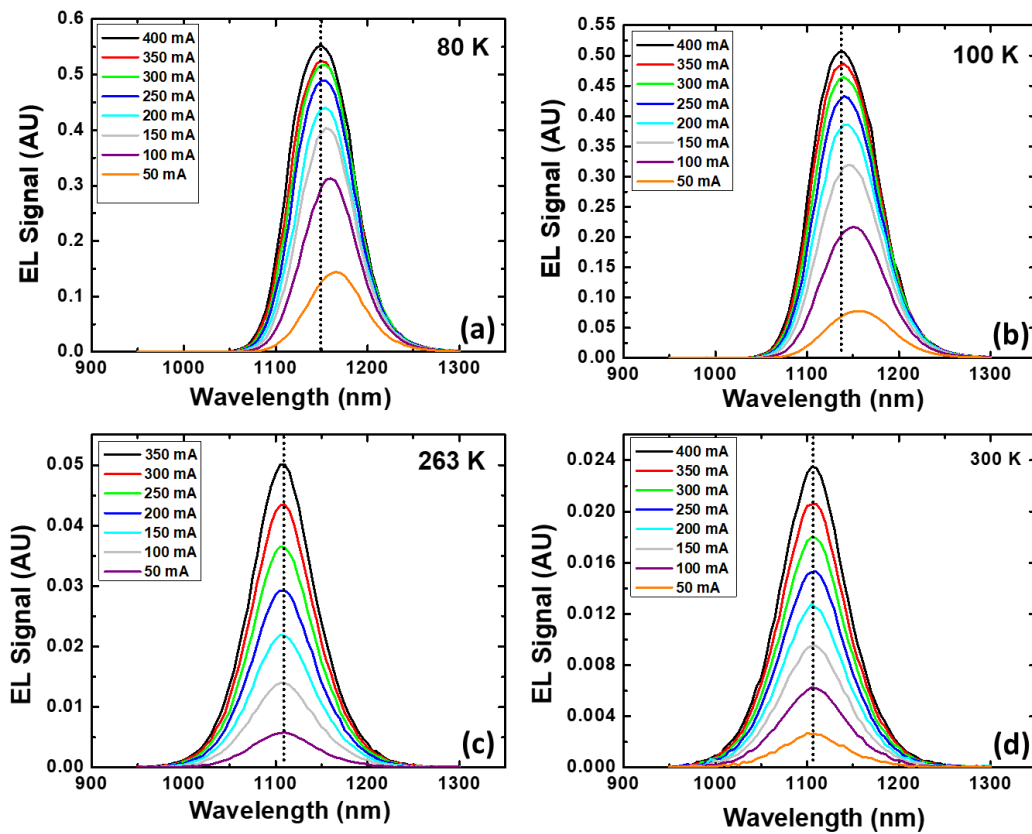


Figure 4. Current injection dependent electroluminescence at temperatures (a) 80 K, (b) 100 K, (c) 263 K and (d) 300 K.

Figure 5. shows the temperature dependent EL of the CIGS solar cell from 80 K up to 300 K. Once again, this figure displays the temperature dependent blueshift of the peak EL energy. At around 200 K this shift stops, and the peak position is stable and retains fixed energy. At low temperatures defect energy levels are accessible to carriers injected in the EL measurement, while at higher temperatures these carriers have enough thermal energy to occupy, redistribute between, and in some respect deactivate these energy levels. Once again, the EL presented here shows that at low temperatures defect energy levels actively participate in the dynamics of carrier generation, trapping and transport, and the recombination processes of the CIGS solar

cells assessed supporting the existence of competing relaxed and metastable states at such temperatures.

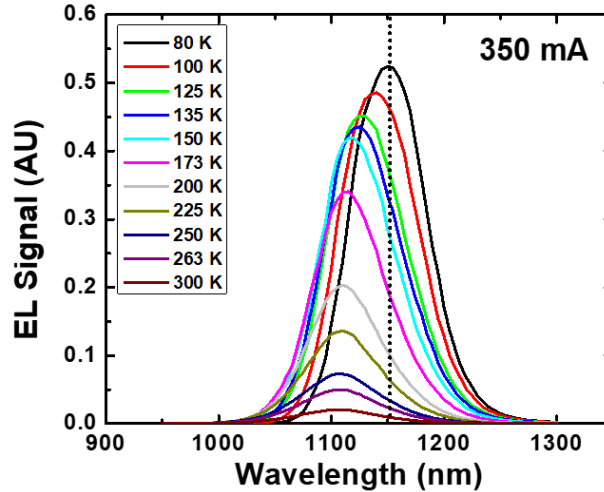


Figure 5. Temperature dependent electroluminescence between 80 K and 300 K at an injection level of 350 mA.

2.5 Concentrated Photovoltaic Measurements

In order to further study the impact of the light intensity on the metastability of CIGS systems, concentrator photovoltaic (CPV) experiments were performed at illumination levels covering Saturn (0.011 Sun) and Jupiter (0.037 Sun), through 1-Sun AM0 up to 10 Sun (AM0). Logically, having more photogenerated carriers due to concentrated illumination will increase V_{OC} and J_{sc} and serve to saturate defect centers, enhancing the performance. Although CIGS is not commonly considered for CPV, multiple studies on CIGS concentrator solar cells have reported improvements in efficiency under such conditions [19-21]. Regarding space applications, multiple research groups have been working on ultra-light Fresnel lens solar concentrators to focus more sunlight onto the solar panels [22, 23]. The SCARLET concentrator project, which used a Fresnel lensing system, was successfully deployed on the DS1 spacecraft on 1998

reducing the required solar cell area by almost a factor of 7 [24]. The thin film structure and lightweight nature of the CIGS solar cells allows the potential for utilization of concentrating systems to compensate the low solar irradiation at distant planets. Additionally, a lensing system fabricated from irradiation shielding material could also serve as both a concentrator and irradiation protection for missions to planets with a harsh radiation environment like Jupiter. Figure 6 shows results of the concentrated J-V scans for both relaxed and metastable states. The experiment is done starting with light intensity at illuminations consistent with Saturn (0.011 Sun) increasing up to 10 Sun AM0. Room temperature conditions (at Earth, 300 K) are also studied for comparison. At temperatures below 200 K - in the relaxed state - signature of a barrier to carrier extraction is evident and reflected in the slope of the forward bias current (see Figure 6-a and b). Such an inflection is not present in the metastable state, supporting the hypothesis that light soaking saturates defect states near the interface, consequently reducing the barrier to carrier collection and lowering the associated resistance. It is not a surprise that at high temperatures (more than 200 K) the difference between the performance of the sample in the metastable and relaxed state is quantitatively zero, since the thermal energy of the carriers, and therefore the effective barriers to collect, are lower.

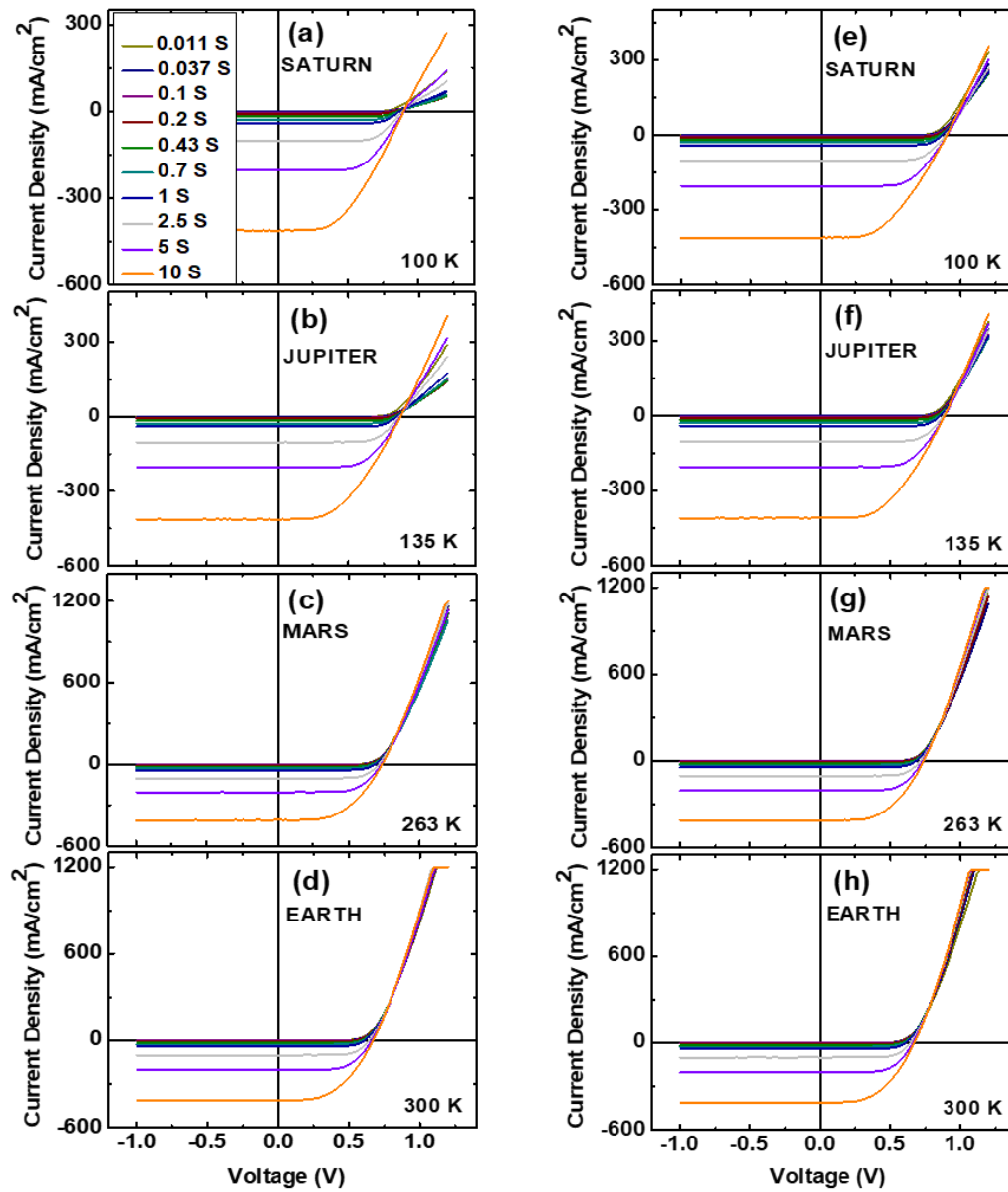
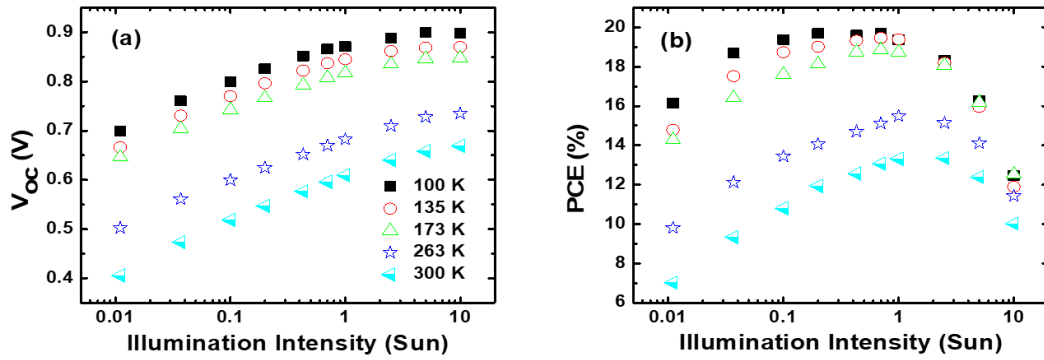


Figure 6. Concentration dependent J-V measurements of CIGS solar cells in the relaxed state, left column (a)-(d), and metastable state, right column (e)-(h) ranging from 0.011 Sun (Saturn) to 10 Sun. The measurements were repeated for the temperature of the planets Saturn, Jupiter (0.037 Sun), Mars (0.43 Sun) and Earth (1-Sun AM0) [15].

Figure 7 presents the PCE and V_{oc} values extracted from the CPV scans. These graphs convey valuable information regarding the energy positions of band edges and the role and presence of

defects. In this Figure, a rise of the V_{OC} is seen for higher intensities followed by saturation for both the relaxed (Figure 7(a)) and metastable (Figure 7(c)) states. The V_{OC} increases at intensities between 0.011 and 2 Sun, for all temperatures. As the light intensity increases, the magnitude of V_{OC} also climbs, approaching the band gap of the CIGS at the highest intensities. This is seen in the plateau of V_{OC} above 2-Sun concentration. In addition, V_{OC} also increases with light intensity as a result of occupation and saturation of trap states, both in the bulk absorber, and more importantly, at the CIGS/CdS interface. This light induced defect passivation reduces the recombination losses and improves the V_{OC} [25]. Comparing Figures 7 (b) and (d), the peak power conversion efficiency achieved in the metastable state is marginally more than that of the relaxed state. The efficiency of the cell increases because of improved V_{OC} up to 1 Sun. Although above 1 Sun, a significant drop in the performance of the cell is also apparent.

Relaxed



Metastable

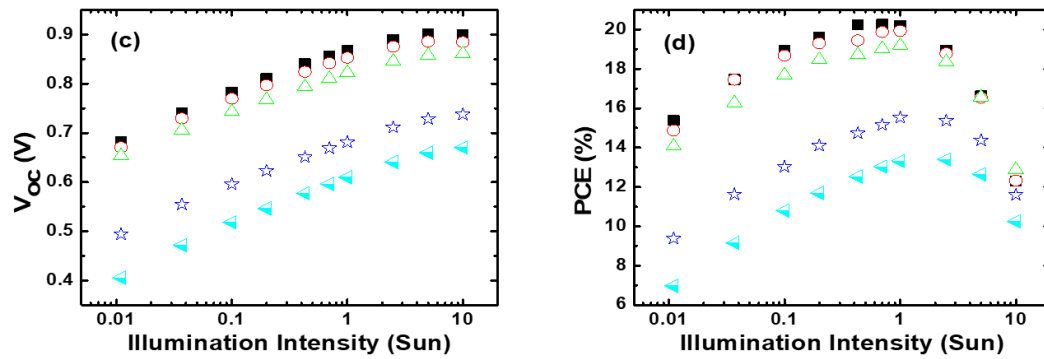


Figure 7. V_{oc} and PCE values extracted from CPV measurements in Figure 3. Figures (a) and (b) in the top row show the results of the relaxed state and the bottom row (c) and (d) shows the results of the metastable state, respectively [15].

Such reductions in PV parameters and performance at high carrier generation rates is mainly related to heating and thermal losses in the solar cell. Here, considerable losses are observed at relatively low carrier generation rates, with no significant reduction of V_{oc} . It is expected that the band gap energy decreases in response to the thermal expansion of the lattice, translating in a decrease in V_{oc} if the temperature of the solar cell is increasing. Therefore, the loss in photovoltaic performance above 1 Sun is unlikely to be related to heating of the cell, but rather the effect of a parasitic barrier at the CIGS/CdS interface, which is more pronounced at lower temperatures (Saturn -100 K; Jupiter -135 K) where the thermal energy of the carriers is lower.

This barrier limits carrier transport, as the light intensity and hence carrier generation rate increases. The carrier transport rate is related to the height of the barrier, temperature, and the thermionic emission rate. At lower light intensities, such as at Saturn and Jupiter, the rate of thermionic emission exceeds that of the carrier photogeneration. While at higher generation rates, extraction of carriers is limited by the comparatively low thermionic emission rate. This causes an increase in the series resistance, and hence lowers the fill factor, which in practice translates in reduced the PCE and performance of the solar cell. At low temperatures this phenomenon emerges at intensities of $\sim 1-2$ Sun, suggesting that at LILT, the barriers associated to the interfaces in current CIGS solar cell structure do not considerably impact the performance of the cell, although optimized architectures would be needed for space CPV applications.

2.6 Time Dependent Light Soaking Measurements

Figure 8 shows the effect of light soaking on the photovoltaic performance of the solar cells. The time dependent light soaking shows approximately the average time scale it takes for the defect states to be populated or saturated. At 77 K where the defect states have a big impact on carrier generation and extraction it is seen that with light soaking the resistance experienced by the majority carriers (due to voltages above V_{OC}) is reduced. This effect at the same time improves the fill factor. At 120 K there is an anomaly in the behavior of the J-V curve, which has been reported by other groups in the literature [26, 27]. Here, with increased light soaking time the series resistance and fill factor are almost unchanged, but the photocurrent improves considerably (reflected in higher J_{SC} values). This is again in good agreement with occupation deactivation of the defect states, which cannot capture carriers translating to an improved photocurrent. At 200 K light soaking has the minimum effect on the performance of the solar cell, and there is minor reduction in the series resistance experienced by majority carriers. Again,

this is due to the defect states being occupied as a result of the higher intrinsic carrier density at elevated temperatures.

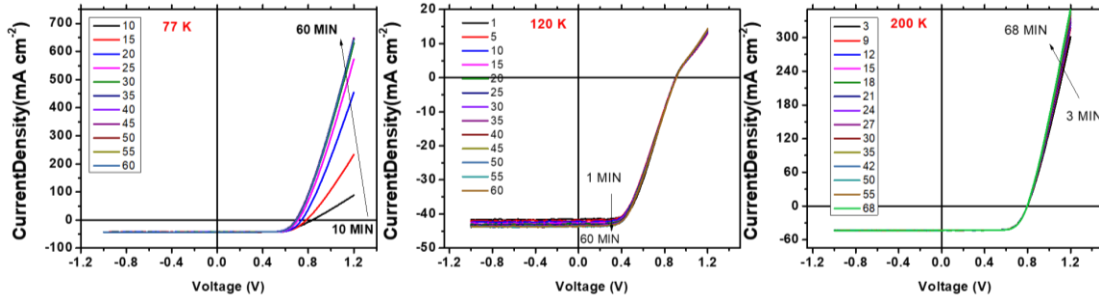


Figure 8. Time dependent light soaking effect on the J-V measurements at three temperatures 77 K, 120 K, and 200 K respectively from left to right.

2.7 Effect of Proton Irradiation

Previous work on CIGS cells with a soda lime substrate predicted high radiation tolerance for these systems and therefore potential for space power applications [28, 29]. To investigate the performance of the thin film flexible CIGS with stainless steel substrates in the extreme radiation environments of outer planets, particularly Jupiter, the effect of high energy proton irradiation has been studied to evaluate whether the previous predictions of higher radiation hardness in CIGS [28, 29] is transferred to LILT environments in the flexible systems. Here, unencapsulated cells were irradiated with energetic (1.5 MeV) protons at the Amethyst (Research Inc) with varying fluences to assess the solar cell regions most vulnerable to irradiation damage. Figure 8 presents a comparison of the light J-V scans for the reference and irradiated CIGS cells under the LILT condition for the planets of interest. The solar cells were bombarded with 1.5 MeV protons at fluences of 1×10^{11} , 5×10^{11} , 1×10^{12} , and 1×10^{13} (H^+/cm^2) for cells C, D, E and F, respectively. Such proton irradiation will induce sub gap defect states and consequent band tailing, which results in reduced photovoltaic performance. As the fluence of irradiation rises the

rectification quality of the J-V is reduced in all cases. Although the irradiation damage reduces the J_{SC} , in a systematic manner the effect on V_{OC} is more significant. Moreover, the relative damage in performance is more pronounced at the conditions of Jupiter and Saturn as shown in Figure(s) 9(a) and (b), respectively. For both planets - even at the lowest fluence of 1×10^{11} p/cm² (green) – perturbation due to shunt and series resistance are significant. At the highest fluence of 1×10^{13} protons/cm² (cyan) the rectifying behavior of the solar cell is completely removed, and the CIGS cells are almost permanently damaged. The CIGS material has a polycrystalline structure that is granular in nature, making these materials particularly vulnerable to defect generation at the grain boundaries and shunting through these defects [30, 31]. The higher fluence of irradiation therefore is expected to induce more shunting channels at these grain boundaries causing significant leakage paths in the system. Noticeably, at higher temperatures and illumination levels such as those at Martian conditions (Figure 9(c)) and Earth (Figure 9(d)) the effects of irradiation are less pronounced, yet still dominated by losses in V_{OC} . This is due to the increase in defects states in the absorber layer that cause non-radiative recombination (SRH) losses. This is reflected in a higher dark current (not shown) and a consequential large loss of V_{OC} . This deleterious effect on V_{OC} is more pronounced at the lower temperature-lower intensity conditions of the outer planetary or Saturn and Jupiter due to the smaller thermal energy and generation rate of carriers in these systems as compared to Mars and/or near-Earth orbit.

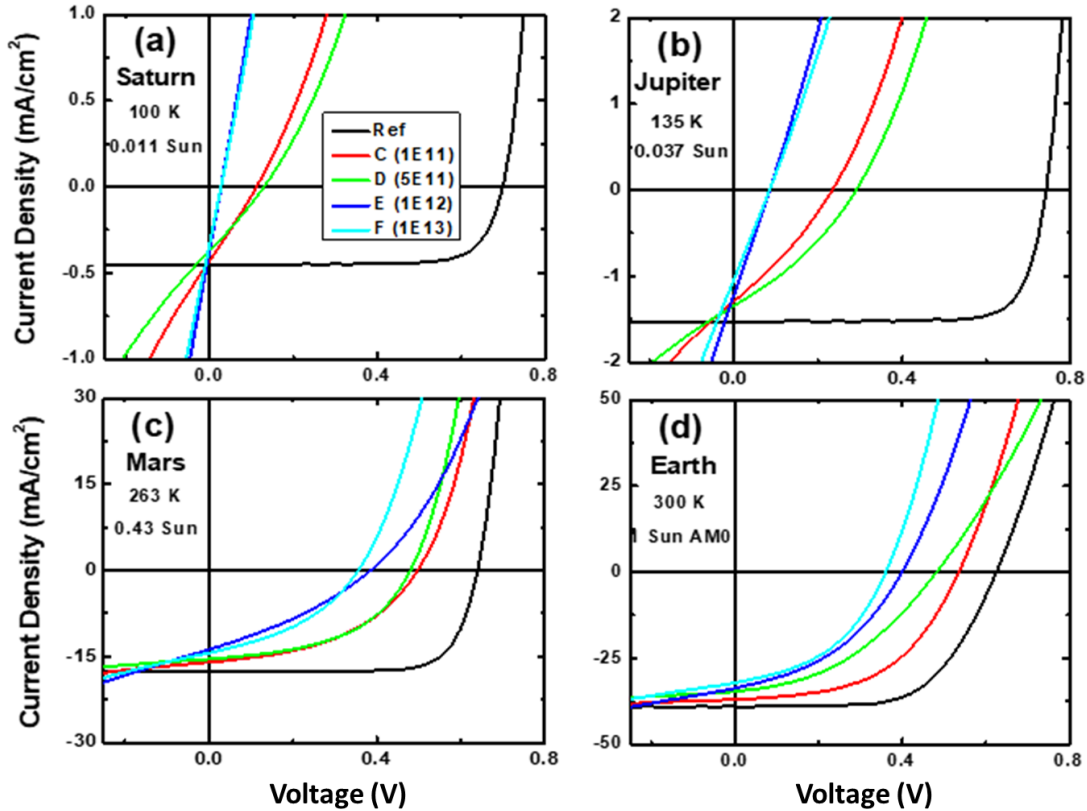


Figure 9. Light J-V of the Reference and irradiated samples under LILT conditions of the planets. Samples C, D, E and F are irradiated with 1.5 MeV protons and fluences of 1×10^{11} , 5×10^{11} , 1×10^{12} , and 1×10^{13} (H⁺/cm²), respectively [15].

To obtain further information regarding the loss mechanisms experienced by the CIGS solar cells after irradiation, external quantum efficiency (EQE) measurements were performed as shown in Figure 10 (a), which provides a comparison of the reference and irradiated samples. Also indicated in the figures are color-coded zones reflecting the various loss processes in the solar cell including: (I) the upper window layer (ZnO) absorption (red); (II) the buffer layer (CdS) absorption (blue); (III) wideband reflection from the surface of the solar cell (gray); (IV) recombination losses in the absorber layer (green); and (V) the transmission of photons with energies less than the bandgap of CIGS (brown).

With increasing fluence, the losses in EQE systematically increase in agreement with the reduction pattern of J_{SC} upon irradiation, another indication of substantial reductions in the performance of the cells after high energy proton irradiation. While all regions of the EQE spectra are affected, damage inflicted close to p-n junction (CIGS/CdS interface) has a smaller impact on carrier collection, as this is the region in which the space charge field is strongest, facilitating carrier extraction. The most pronounced region loss occurs in the CIGS absorber layer as illustrated in Figure 10 (b), which compares the change in EQE of irradiated cells with respect to the reference sample (ΔEQE). This further verifies an increase in SRH recombination losses due to defect formation. This in turn substantially reduces the diffusion length of minority carriers and carrier collection efficiency consistent with the observed reductions of J_{SC} with increasing proton fluences, as seen in Figure(s) 9. The substantial rise in density of defect states in the absorber layer also reduces V_{OC} as photo-excited carriers are trapped by defects, especially at lower temperature and illumination levels. Indeed, an increased density of recombination centers has been shown to be detrimental to device performance by spectroscopic examinations of high efficiency CIGS cells [32]. This showcases the significant decrease in diffusion length of minority carriers with reduced extraction efficiency when generated deeper in the cell farther from the junction, and indicates that significant damage may have been inflicted at the back contact upon irradiation, further degrading the diode characteristics of the device.

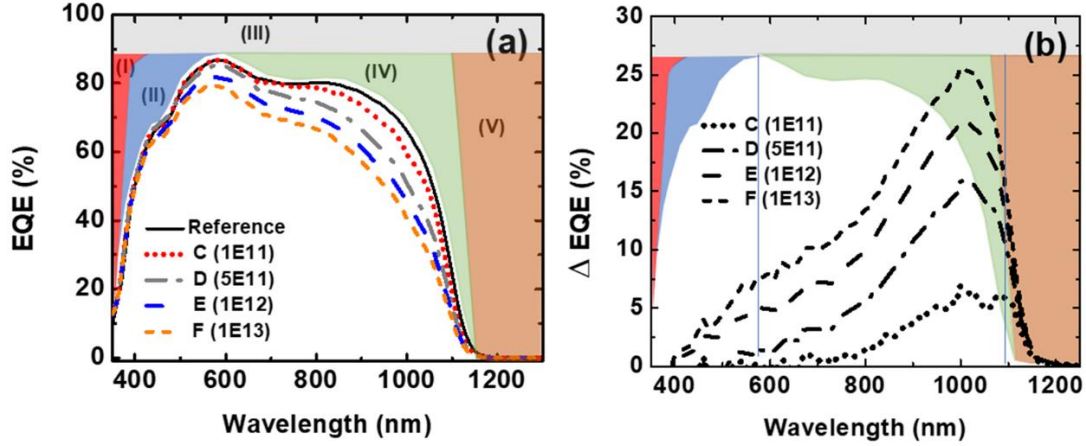


Figure 10: (a) Comparison of EQE at room temperature of the non-irradiated sample (reference) with 1.5 MeV proton irradiated samples with varying fluences (ion/cm²). (b) Difference between the EQE of reference and irradiated samples (Δ EQE) [15].

In all cases (increasing with fluence) leads to substantial losses near the back contact of the solar cell, which is reflected by the largest reduction in extraction in the EQE. This response follows the path of protons in the cell [33] and their projection depth, simulations of which are presented in Figure 11 (a). These simulations were carried out to track the trajectories of the incident 1.5 MeV protons in the cell and to assess the damage these particles produced in the constituent layers. These effects were simulated through a well-known particle interaction code: The stopping and range of ions in matter (SRIM-2013) simulation [34]. The SRIM program has been coded based on the binary collision approximation using Monte-Carlo random number generator simulations. In order to create the implant profile and approximate the total damage (vacancies and displaced atoms), “full cascade” calculations were carried out for 100,000 ions. The longitudinal straggling and projected range (R_p) of the 1.5 MeV protons were calculated to be 0.91 μ m and 3.72 μ m, respectively. Hence, almost all of the protons pass the absorber layer of CIGS and cumulate at the stainless-steel substrate. This suggests ionizing energy loss (IEL) processes are the major contributor of damage in these experiments and conditions. The total

density of damage in the constituent layers of the cell as simulated for 1×10^{13} protons/cm² is shown in Figure 10 (b).

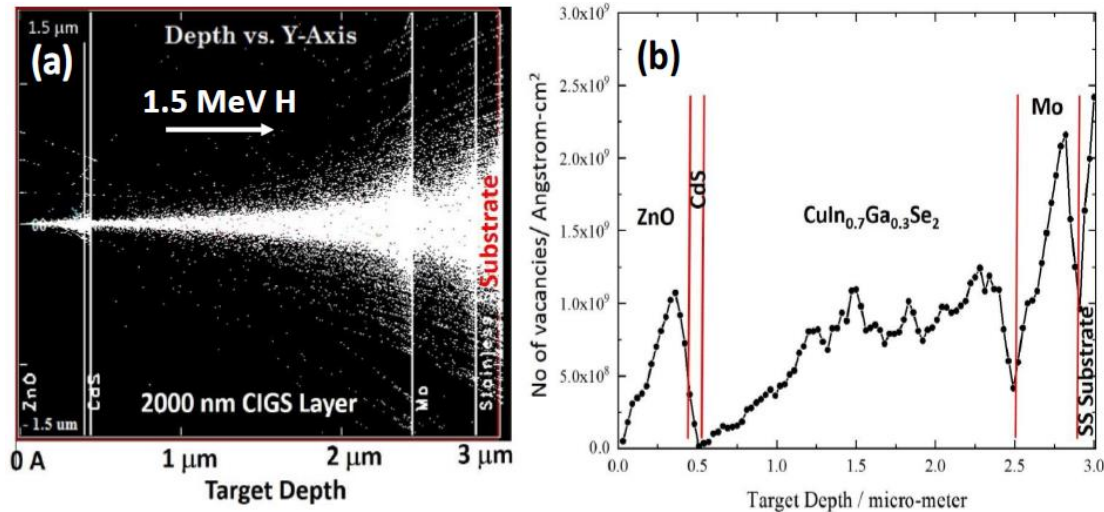


Figure 11: (a) Stopping and Range of Ions in Matter (SRIM) simulated trajectories of 1.5 MeV protons in the CIGS solar cell. The target structure consisted of ZnO(400 nm)/ CdS(40 nm)/ $\text{CuIn}_{0.7}\text{Ga}_{0.3}\text{Se}_2$ (2000 nm)/ Mo (400 nm)/ stainless steel substrate. (b) SRIM simulated damage in the structure due to the irradiation of 1.5 MeV protons with a fluence of 1×10^{13} ions/cm² [15].

Figure 11 (b) shows substantial damage in the upper ZnO layer, that is reduced at the CdS/ZnO interface as reflected in a reduction in the magnitude of the EQE around 600 nm (see Figure 10). With increasing depth, the damage inflicted in the CIGS absorber layer increases, reflected in decreased carrier extraction at longer wavelengths in Figure 10(a) and (b). The protons that accumulate at the back side of the CIGS devices in the Mo-contact and steel substrate may also contribute to the substantial shunting that is observed upon irradiation at all fluences and conditions as observed in Figure 9.

2.8 SCAPS Simulation

The structure of the solar cells investigated is shown in Figure 12 (a), and Figure 12(b) shows the layer structure implemented using the solar cell capacitance simulator, SCAPS. The name of each layer and the order is shown in the right Figure 12 (c). For the top and bottom contact a flat band contact is considered. Many studies on CIGS have predicted presence of a p+ layer (a secondary layer) near the CIGS/CdS interface. In this study using SCAPS assuming a p+ layer at this interface also helps improve the behavior of the solar cell. All the thicknesses provided in the structure of the cell are used for simulation except for absorber, in which a 2 μm CIGS divided in two layers of 1.8 + 0.2 μm layers is implemented to control/or simulate the properties of the interface better.

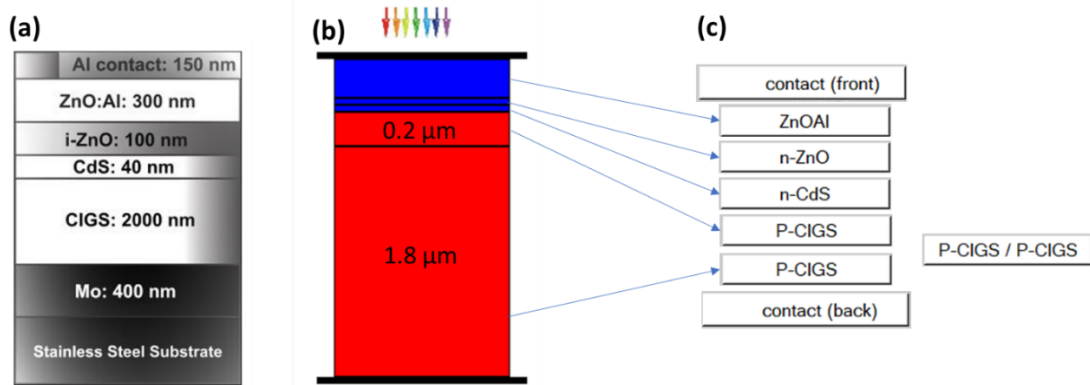


Figure 12: (a) Structure of the CIGS solar cell (b) SCAPS simulation of the structure of the solar cell and direction of illumination (c) Respective layers for the solar cell structure in the simulation.

The band gap of the main absorber layer is graded through changing the composition factor of Ga shown in Figure 13 (a). This grading is also used here in the SCAPS simulation of the solar cell. Being a compound of elements with atom sizes close to each other, many defect types show low formation energy in CIGS. Some common defect types are shown in Figure 13 (b), and typical densities used in simulations of this system for some of defects are also provided.

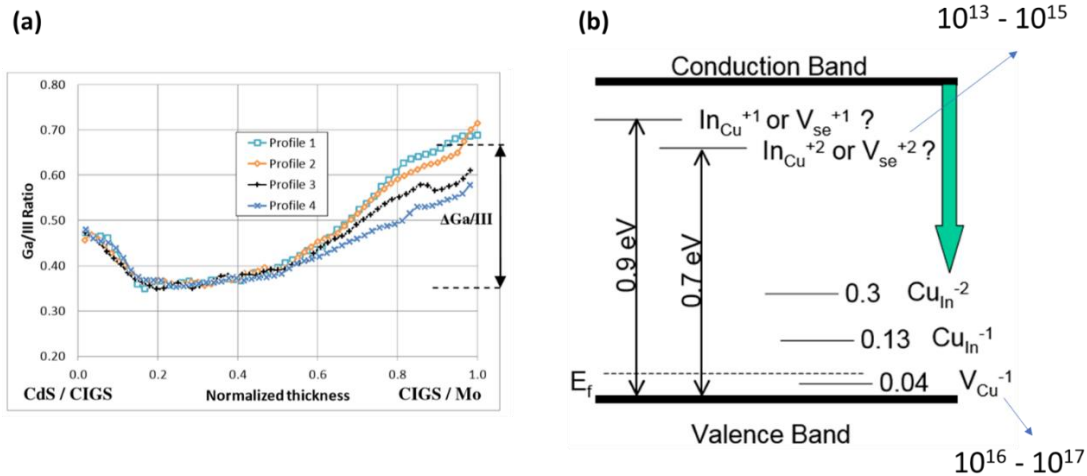


Figure 13. (a) Grading profile of the band gap via tuning Ga and In composition factors (b) Defect states in the band gap of the CIGS material with their respective energy levels from the valance band. Figure in the right reproduced from Cu(In,Ga)(S,Se)₂ Crystal Growth, Structure, and Properties, by Angus Rocket [35].

By increasing the defect density in the main absorber layer and also their contribution at a specific depth of 0.2 micrometer inside the absorber layer, we can reproduce the results of our J-V and EQE measurements from the irradiated samples to a good extent as shown in Figures 14 (a)-(d). Along with adding the defects states, we also reduced the shunt resistance and increased the series resistance. How these values are changed can be seen in table II.

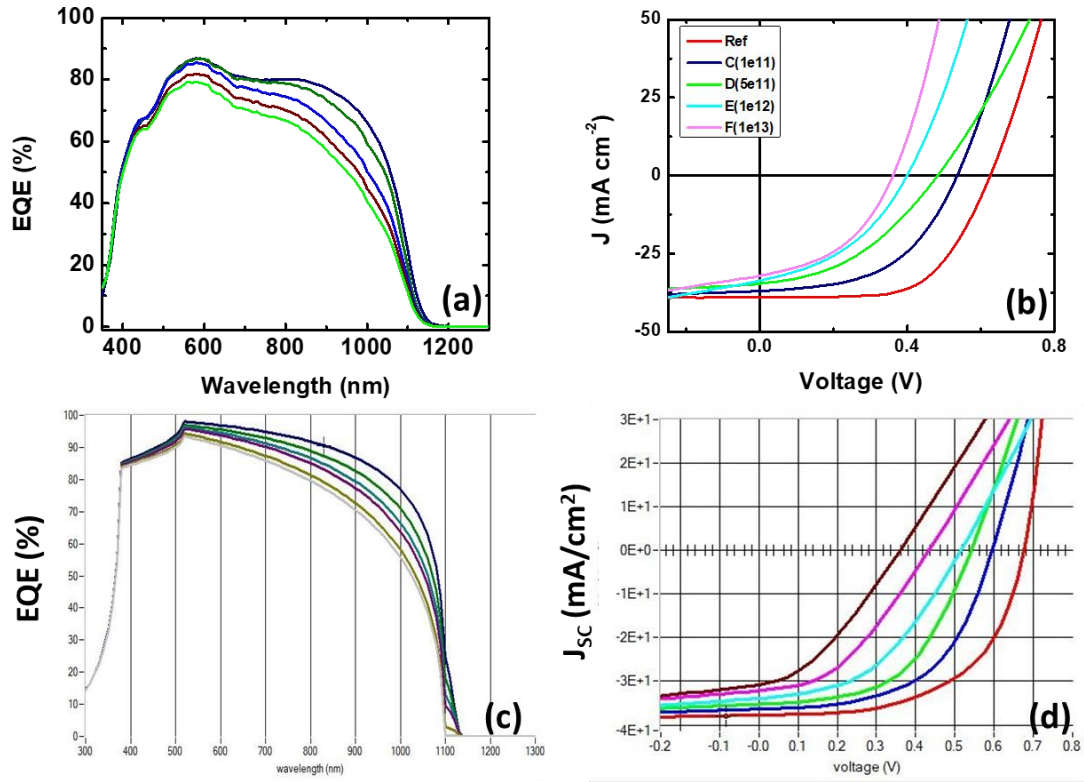


Figure 14. (a) EQE of the reference solar cell and the irradiated cells (b) J-V graph of the reference sample and the irradiated cells (c) SCAPS simulation of the EQE of the reference cell and the irradiated cells (d) SCAPS simulation of the J-V graphs for reference cell and the irradiated ones.

Defects added to these layers result in mid-gap energy defects similar to selenium vacancies or indium-copper anti-sites that are prevalent in CIGS, the energy level of which is known to be ~ 0.6 eV above the valence band. The density of secondary CIGS layer is kept almost unchanged while for the main absorber the density of these defects increases as the irradiation fluence increases (from left to right in Table II). The series resistance is also observed to increase with increasing the irradiation fluence, while the shunt resistance decreases. The defects implanted at the depth of 0.2 micrometer are also observed to rise with fluence considerably.

Table II. Intensity, temperature, relaxed and metastable V_{OC} and FF values for the CIGS solar cell in the LILT conditions of each planet.

Sample	Ref	C	D	E	F
Density of defects In CIGS Secondary layer (1/cm ³)	2×10^{14}	9×10^{14}	9×10^{14}	9×10^{14}	9×10^{14}
Density of defects At the Interface between two CIGS layers (1/cm ²)	$2 * E5$	1×10^{10}	5×10^{10}	2×10^{11}	1.4×10^{12}
Density of defects in CIGS Main absorber layer (1/cm ³)	7.5×10^{14}	1.7×10^{15}	4×10^{15}	7×10^{15}	6×10^{16}
Series Resistance (Ω)	0.2	2	3	5	6
Shunt Resistance (Ω)	1×10^7	1000	500	200	150

2.9 Conclusions

Under the outer planetary conditions of deep space, the main elements that decide the final efficiency of the solar cells are the light intensity, temperature, and the irradiation level (LILT) of the target planet, or mission. In this work, various PV characterizing techniques were applied on commercially available flexible CIGS solar cells, tracing the effects of metastability and defect formation on the performance of the system under LILT conditions. At low temperatures, higher V_{OC} and fill factor values translate to improved photovoltaic performance as compared to terrestrial AM0 conditions. Evidence of inhibited carrier extraction is observed at low temperatures and is ascribed to the presence of interfacial defects and the doping contrast between the bulk CIGS and CdS window layer in these structures. The effect of this interface is a barrier to carrier collection that declines under light soaking, as the system undergoes a transition from the so-called relaxed to metastable state. At elevated temperatures (> 200 K), the effect of this barrier to minority carrier collection is reduced, due to the higher thermal energy of the

carriers at these temperatures and an enhanced thermionic emission rate under such conditions. Despite the effects of metastability in the CIGS system, and the parasitic barrier at the CdS/CIGS interface, the low temperatures of the planets studied here resulted in a substantially higher power conversion efficiency than. Moreover, using a lensing system and concentration up to ~ 1 Sun AM0 was observed to further increase the efficiency, for the temperatures of Jupiter (135 K) and Saturn (100 K) with no significant reduction in fill factor, reflecting effective carrier extraction at these conditions. Proton irradiation of the CIGS solar cells induced defect states predominantly in the absorber layer (and with increasing depth), decreasing the diffusion length of minority carriers, and at the same time lowering the shunt resistance, which translates in the reduced PV parameters most substantially; V_{oc} . The results of this study suggest while the CIGS solar cell performs well in LILT conditions, but proper or mission specific encapsulation would be needed for applications in the extreme radiation environments of space.

2.10 References

- [1] Solar Frontier Achieves World Record Thin-Film Solar Cell Efficiency of 23.35%, 2019. http://www.solar-frontier.com/eng/news/2019/0117_press.html.
- [2] L.L. Baranowski, P. Zawadzki, S. Lany, E.S. Toberer, A. Zakutayev, A review of defects and disorder in multinary tetrahedrally bonded semiconductors, *Semiconductor Science and Technology*, 31 (2016) 123004. 10.1088/0268-1242/31/12/123004
- [3] D. Shin, B. Saparov, D.B. Mitzi, Defect Engineering in Multinary Earth-Abundant Chalcogenide Photovoltaic Materials, (2017). 10.1002/aenm.201602366
- [4] M. Maciaszek, P. Zabierowski, Influence of relaxation processes on the evaluation of the metastable defect density in Cu(In,Ga)Se₂, *Journal of Applied Physics*, 119 (2016) 215103. 10.1063/1.4953145

- [5] M. Igalson, M. Cwil, M. Edoff, Metastabilities in the electrical characteristics of CIGS devices: Experimental results vs theoretical predictions, *Thin Solid Films*, 515 (2007) 6142-6146. 10.1016/j.tsf.2006.12.038
- [6] C.R. Brown, V.R. Whiteside, D. Poplavskyy, K. Hossain, M.S. Dhoubhadel, I.R. Sellers, Flexible Cu(In,Ga)Se₂ Solar Cells for Outer Planetary Missions: Investigation Under Low-Intensity Low-Temperature Conditions, *IEEE Journal of Photovoltaics*, 9 (2019) 552-558. 10.1109/JPHOTOV.2018.2889179
- [7] D. Przado, M. Igalson, R. Bacewicz, M. Edoff, The Influence of Metastabilities on the Luminescence in the Cu(In,Ga)Se₂ Solar Cells, 2007. 10.12693/APhysPolA.112.183
- [8] M. Igalson, P. Zabierowski, Electron traps in Cu (In, Ga) Se₂ absorbers of thin film solar cells studied by junction capacitance techniques, 2003.
- [9] F. Pianezzi, P. Reinhard, A. Chirila, B. Bissig, S. Nishiwaki, S. Buecheler, A.N. Tiwari, Unveiling the effects of post-deposition treatment with different alkaline elements on the electronic properties of CIGS thin film solar cells, *Physical chemistry chemical physics : PCCP*, 16 (2014) 8843-8851. 10.1039/c4cp00614c
- [10]
https://www.researchgate.net/post/Whats_the_reason_for_the_crossover_of_illuminated_and_dark_J-V_curve_in_CIGS_solar_cells.
- [11] J. Bailey, G. Zapalac, D. Poplavskyy, Metastable defect measurement from capacitance-voltage and admittance measurements in Cu(In, Ga)Se₂ Solar Cells, in: 2016 IEEE 43rd Photovoltaic Specialists Conference (PVSC), 2016, pp. 2135-2140. 10.1109/pvsc.2016.7750011

- [12] Q. Cao, O. Gunawan, M. Copel, K.B. Reuter, S.J. Chey, V.R. Deline, D.B. Mitzi, Defects in Cu(In,Ga)Se₂ Chalcopyrite Semiconductors: A Comparative Study of Material Properties, Defect States, and Photovoltaic Performance, *Advanced Energy Materials*, 1 (2011) 845-853. 10.1002/aenm.201100344
- [13] S. Lany, A. Zunger, Light- and bias-induced metastabilities in Cu(In,Ga)Se₂ based solar cells caused by the (VSe-VCu) vacancy complex, *Journal of Applied Physics*, 100 (2006) 113725. 10.1063/1.2388256
- [14] T. Eisenbarth, T. Unold, R. Caballero, C.A. Kaufmann, H.-W. Schock, Interpretation of admittance, capacitance-voltage, and current-voltage signatures in Cu(In,Ga)Se₂ thin film solar cells, *Journal of Applied Physics*, 107 (2010) 034509. 10.1063/1.3277043
- [15] H. Afshari, B.K. Durant, C.R. Brown, K. Hossain, D. Poplavskyy, B. Rout, I.R. Sellers, The role of metastability and concentration on the performance of CIGS solar cells under Low-Intensity-Low-Temperature conditions, *Sol. Energy Mater. Sol. Cells*, 212 (2020) 110571. <https://doi.org/10.1016/j.solmat.2020.110571>
- [16] S. Song, D.B. Khadka, S. Kim, J. Kim, J. Gwak, J.H. Yun, K. Yoon, Study of Inx (O, OH, S) y buffer layer effect on CIGSe thin film solar cells, *Current Applied Physics*, 14 (2014) S17-S22.
- [17] V. Nadenau, U. Rau, A. Jasenek, H.W. Schock, Electronic properties of CuGaSe₂-based heterojunction solar cells. Part I. Transport analysis, *Journal of Applied Physics*, 87 (2000) 584-593. 10.1063/1.371903
- [18] M. Gloeckler, C.R. Jenkins, J.R. Sites, Explanation of Light/Dark Superposition Failure in CIGS Solar Cells, *MRS Proceedings*, 763 (2011) B5.20. 10.1557/PROC-763-B5.20
- [19] K.R. J. Ward, F. Hasoon, T. Coutts, J. Keane, T. Moriarty, and R. Noufi Cu(In,Ga)Se₂ Thin-Film Concentrator Solar Cells, in: NCPV Program Review Meeting, Colorado, 2001.

- [20] Y. Hirai, H. Nagashima, Y. Kurokawa, A. Yamada, Experimental and Theoretical Evaluation of Cu(In,Ga)Se₂ Concentrator Solar Cells, Japanese Journal of Applied Physics, 51 (2011) 014101. <https://doi.org/10.1143/jjap.51.014101>
- [21] J.S. Ward, B. Egaas, R. Noufi, M. Contreras, K. Ramanathan, C. Osterwald, K. Emery, Cu(In,Ga)Se₂ solar cells measured under low flux optical concentration, in: 2014 IEEE 40th Photovoltaic Specialist Conference (PVSC), 2014, pp. 2934-2937. 10.1109/PVSC.2014.6925546
- [22] G.R. Whitfield, R.W. Bentley, C.K. Weatherby, A.C. Hunt, H.D. Mohring, F.H. Klotz, P. Keuber, J. Miñano, E. Alarte-Garvi, The Development and Testing of Small Concentrating PV Systems, 1999. 10.1016/S0038-092X(00)00045-1
- [23] M. O'Neill, M. F. Piszczor, M. I. Eskenazi, A. J. McDanal, P. George, M. M. Botke, H. W. Brandhorst, D. Edwards, D. Hoppe, Ultralight stretched Fresnel lens solar concentrator for space power applications, 2003. 10.1117/12.505801
- [24] D.M. Murphy, The Scarlet Solar Array: Technology Validation and Flight Results Deep Space 1 Technology Validation Report
- [25] S.B. Zhang, S.-H. Wei, A. Zunger, H. Katayama-Yoshida, Defect physics of the CuInSe₂ chalcopyrite semiconductor, Physical Review B, 57 (1998) 9642-9656. 10.1103/PhysRevB.57.9642
- [26] P. Zabierowski, U. Rau, M. Igalson, Classification of metastabilities in the electrical characteristics of ZnO/CdS/Cu(In,Ga)Se₂ solar cells, Thin Solid Films, 387 (2001) 147-150. [https://doi.org/10.1016/S0040-6090\(00\)01850-2](https://doi.org/10.1016/S0040-6090(00)01850-2)
- [27] M. Igalson, Metastable defect distributions in CIGS solar cells and their impact on device efficiency, MRS Online Proceedings Library (OPL), 1012 (2007) 1012-Y1004-1001.

- [28] A. Jasenek, U. Rau, K. Weinert, I.M. Kotschau, G. Hanna, G. Voorwinden, M. Powalla, H.W. Schock, J.H. Werner, Radiation resistance of Cu(In,Ga)Se₂ solar cells under 1-MeV electron irradiation, *Thin Solid Films*, 387 (2001) 228-230. 10.1016/S0040-6090(00)01847-2
- [29] A. Jasenek, U. Rau, K. Weinert, H.W. Schock, J.H. Werner, Radiation response of Cu(In,Ga)Se₂ solar cells, in: 3rd World Conference on Photovoltaic Energy Conversion, 2003. Proceedings of, 2003, pp. 593-598 Vol.591.
- [30] S.P. Harvey, H. Guthrey, C.P. Muzzillo, G. Teeter, L. Mansfield, P. Hacke, S. Johnston, M. Al-Jassim, Investigating PID shunting in polycrystalline CIGS devices via multi-scale, multi-technique characterization, *IEEE Journal of Photovoltaics*, 9 (2019) 559-564.
- [31] M. Theelen, V. Hans, N. Barreau, H. Steijvers, Z. Vroon, M. Zeman, The impact of alkali elements on the degradation of CIGS solar cells, *Progress in Photovoltaics: Research and Applications*, 23 (2015) 537-545.
- [32] S. Jensen, A. Kanevce, L. Mansfield, S. Glynn, S. Lany, D. Kuciauskas, Optically induced metastability in Cu (In, Ga) Se₂, *Scientific reports*, 7 (2017) 1-7.
- [33] B. Anspaugh, *GaAs Solar Cell Radiation Handbook*, JPL Publication, Jet Propulsion Laboratory, California Institute of Technology, Pasadena, California, 5 (1996) 1.
- [34] J.F. Ziegler, M. Ziegler, J. Biersack, *SRIM-The stopping and range of ions in matter* (2010), *Nuclear Instruments and Methods in Physics Research. Section B, Beam Interactions with Materials and Atoms*, 268 (2010) 1818-1823.
- [35] D. Poplavskyy, J. Bailey, R. Farshchi, D. Spaulding, Impact of Ga/III Profile on Voltage-dependent Collection Losses in CIGS Solar Cells, in: 2017 IEEE 44th Photovoltaic Specialist Conference (PVSC), IEEE, 2017, pp. 1686-1690.

Chapter 3

Electron Radiation Tolerance of GaAs_{1-x}Sb_x Solar Cells

High efficiency and radiation hardness are two key factors needed for solar cells functioning in space. although multi-junction solar cells are being used extensively in space [1-4], their tolerance to radiation environments, specifically in deep space adds complexity to the design of their structure since there is variability in the sub-cell radiation hardness [5-7]. Numerous studies have focused on improving radiation tolerance of the tandem solar cells [8-11] however, relatively thick cover glass is still required to implement these systems, which leads to increase in weight of the panels and reduces the specific system power (W/kg). Although GaAs has high power conversion efficiency, its performance in severe radiation environments such as under the LILT conditions or Jupiter and its moons (for example) is concerning. While these systems are already being used in space missions, they do require relatively thick cover glass for radiation protection, which removes the capacity for compact stowage and deployment [8]. More Recently, ultrathin versions of GaAs are suggested to offer potentially more radiation-hardness for space [12], if additional optical management is used to enhance the absorption. The capacity of GaAs_{1-x}Sb_x as a candidate absorber material for outer planetary CubeSAT and SmallSAT [13] missions is particularly interesting. The small satellites have limited area available to be used for surface mounted solar panels limiting the absolute power. This is specifically problematic under the *low-intensity-low-temperature* (LILT) conditions in deep space. Recently, *thin film* solar cell technologies such as CIGS and perovskites, as well as tandem perovskite/CIGS based solar cells are all being investigated for such applications in space [14-17]. In this study, optically *thick* GaAs_{0.86}Sb_{0.14} absorber material is investigated in high levels of electron irradiation. The

experimental results suggest remarkable radiation-resistance of the solar cells without encapsulation, indicating this material has potential for hostile space missions such as those exploring Jupiter [18] or in satellite applications in highly eccentric orbits (HEO) that are being considered to facilitate better internet coverage and enhanced navigation accuracy, but which require more robust solar panels than are currently available due to the high radiation levels in these orbits around the earth.

3.1 Strain Management

The structure of the solar cell is presented in Figure 1 (a) showing different layers including multiple consecutive $\text{GaAs}_{1-x}\text{Sb}_x$ layers with varying composition factors engineered to manage the strain in the system. These p-i-n based $\text{GaAs}_{1-x}\text{Sb}_x$ solar cells are grown using solid source molecular beam epitaxy on n+-GaAs (100) substrates. Upon the substrate, a strain-balanced $\text{GaAs}_{1-x}\text{Sb}_x$ (n-type, $2 \times 10^{17} \text{ 1/cm}^3$) layer is grown at 510 °C followed by a thin n-AlGaAsSb (30 nm) back-surface-field (BSF) layer, which is doped with silicon at $2 \times 10^{18} \text{ 1/cm}^3$. This strain balanced buffer layer is followed by a base region of $\text{GaAs}_{0.86}\text{Sb}_{0.14}$ (n-type, 1000 nm) and 500 nm of undoped $\text{GaAs}_{0.86}\text{Sb}_{0.14}$. The initial n-type $\text{GaAs}_{1-x}\text{Sb}_x$ layer is grown in four 100 nm graded steps/layers ranging from $x = 0.08$ to 0.14, to 0.19, and then decreased once more to 0.14 to allow for strain compensation to reduce the mismatch in lattice constant between the GaAs substrate and $\text{GaAs}_{1-x}\text{Sb}_x$ epilayer producing high quality material in the active region of $\text{GaAs}_{0.86}\text{Sb}_{0.14}$ absorber. The absence of such strain management would result in significant defect formation that is prohibitive for high PV performance [19, 20]. The high optical quality of absorber layers fabricated using this strain management approach is illustrated in Figure 1(b). This figure shows a high-resolution transmission electron microscope (HR-TEM) that demonstrates the absence of defects and disorder - other than at the lower interfaces of the

structure, by design - which is well away from the active region of the solar cell. The design of the p-i-n structure is completed with a Be-doped p-type GaAs_{0.86}Sb_{0.14} emitter (50 nm, 1×10^{18} 1/cm³), p-type AlGaAsSb window layer (30 nm 1×10^{18} 1/cm³), and finally a 20 nm p+-GaAsSb_{0.14} cap layer. Solar cell devices were fabricated using conventional wet-etching and optical lithography resulting in diodes of an average area of ~ 0.25 cm². The contacts were deposited through physical vapor deposition (PVD) with Zn–Au and a Ni-Ge-Au films for the upper p-type and lower n-type electrodes, respectively. The devices were rapid thermal annealed (RTA) at 400 °C for 60 s to facilitate the formation of high quality ohmic contacts [19-21].

For testing the effect of electron irradiation on the performance of the devices, each solar cell was irradiated with 1- MeV electrons at a fluence of 1×10^{15} electrons/cm². These energetic electrons completely penetrate the active region of the structure and rest in the substrate of the device. Irradiation was conducted at the NEO Beam facility in Ohio, and a Faraday cup and CTA film was used to control the flux of irradiation. Cross section imaging was performed using a Titan 80–300 transmission electron microscope (TEM) operated at 300 kV at Arizona State University.

(a)	20nm p ⁺ -GaAsSb
	30nm p-AlGaAsSb Window
	p-50nm GaAsSb
	p-100nm GaAsSb
	500nm i-GaAsSb _{0.14} Base
	1000nm n-GaAsSb _{0.14} Base
	30nm n-AlGaAsSb BSF
	100nm n-GaAsSb _{0.14} Buffer
	100nm n-GaAsSb _{0.19} Buffer
	100nm n-GaAsSb _{0.14} Buffer
	100nm n-GaAsSb _{0.08} Buffer
	100nm n-GaAs Buffer
	n ⁺ GaAs (100) Substrate

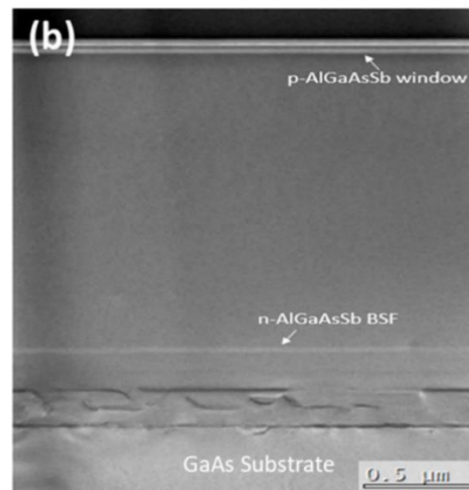


Figure 1: (a) Schematic illustration of the structure of the GaAsSb based solar cell, (b) TEM cross section of the layers of the cell.

The physical structure of the solar cell is seen in the TEM image of the cross section of the device in Figure 1(b). High contrast light-colored strips of the high band gap AlGaAsSb window layers stand out at the top of the structure in this TEM image. Signatures of the strain relaxation in form of defect generation are also evident in the lower sections of the device (between the substrate and the BSF), but such defects are not visible in the upper layers. Figure 2(a) presents the energy band diagram simulated for this device using NRL Bands© and reflects preferential band alignments for carrier extraction in the system. The room temperature photoluminescence (PL) and external quantum efficiency (EQE) of the solar cell are shown Figure 2(b). The PL peak reflects the bandgap of the material, which is well matched to the absorption edge of the EQE spectrum at ~ 1100 nm (1.12 eV). The observed peak in the EQE at ~ 700 nm is due to the absorption in the AlGaAsSb window layer. The longer wavelength tail of the PL indicates the presence of low energy defects or impurity states, which are ascribed to unintended alloy fluctuations and the background impurity concentration in this structure.

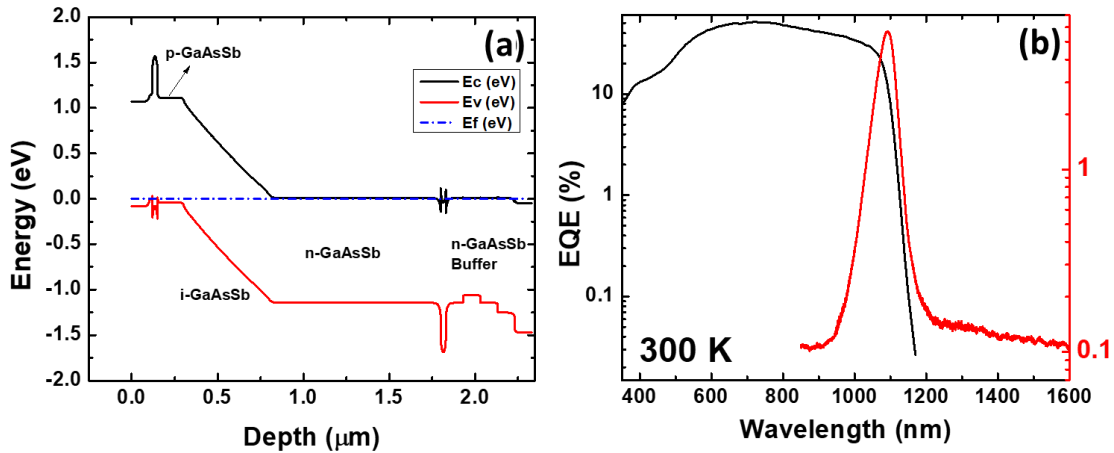


Figure 2: (a) Simulated energy band alignments for the structure calculated using NRL Bands© illustrating the relative positions of the conduction (E_c) and valence band (E_v), in addition to the Fermi-level (E_f) at equilibrium. (b) EQE and PL response of the solar cell at 300 K. Right axis in red shows the PL response and left axis in black shows the EQE response [22].

3.2 Impact of Electron Irradiation on the Solar Cells

In order to test the effect of electron irradiation on performance of the cells, each cell is bombarded with 1- MeV electrons at a fluence of 1×10^{15} electrons/cm². These energetic electrons penetrate the active region of the structure and deep into the device. Irradiation was conducted at the NEO Beam facility in Ohio, and a Faraday cup and CTA film was used to control the flux of irradiation. Cross section imaging was done using a Titan 80–300 transmission electron microscope (TEM) operated at 300 kV.

Figure 3(a) shows the temperature-dependent PL of the cell from 4.2 K to 300 K before electron irradiation. At low temperature ($T < 80$ K), the spectrum has a low energy shoulder (1075 nm), which persists until ~ 200 K. With increasing temperature, the main peak evolves, and a second higher energy transition appears at ~ 1010 nm, which dominates at $T > 80$ K. This higher energy peak, which shifts to longer wavelength with temperature in a Varshni-type dependence, is ascribed to the fundamental band gap of the GaAs_{0.86}Sb_{0.14}, [23]. The existence of lower energy transitions and their temperature dependent behavior including thermally induced redistribution of carriers into the higher energy levels is well known in III-V ternaries/quaternaries such as GaInNAs [24, 25], AlInAs [26], and InAlAsSb [27], and is typically ascribed to charge carriers trapped in shallow coulomb potentials and/or alloy fluctuations. Similar behaviors were recently reported in GaAs_{1-x}Sb_x system [28] equivalent to that observed here, where the low energy transition was explained through presence of localized states as a result of Sb-segregation. At

higher temperatures, the thermal energy of carriers trapped in the alloy fluctuations increases, freeing carriers and redistributing them into the available energy bands which screens the defect band(s) and reflects the true band gap PL at higher temperatures. Further verification of this phenomenological interpretation is illustrated in Figure 3(c), which presents the change in the emission peak energy versus temperature for this system before (solid black squares) and after (solid red squares) electron irradiation.

This Figure reveals the classic s-shape pattern in the emission energy of materials affected by carrier localization and alloy inhomogeneity, especially at lower temperatures. At low temperature ($4.2 \text{ K} < T < 100 \text{ K}$) carriers trapped in defects relax to lower energy impurity states, causing the red shift of the peak PL emission energy. At $T > 90\text{--}100 \text{ K}$ carriers gain enough thermal energy to escape the traps, screening the localization energy. This causes the PL blueshift of the emission with respect to that of the energy of the defect band. After this point ($T > 100 \text{ K}$) the band gap follows the conventional temperature dependence of the most semiconductor materials according to the Varshni equation. Figure 3(b) presents the temperature dependent PL of the same (unencapsulated) solar cell after the cell is irradiated with 1 MeV electrons at a fluence of $\sim 1 \times 10^{15}$ electrons/cm². This fluence is equivalent to the irradiation dose of about 1 year at the severe radiation environments experienced by encapsulated (0.5 mm) solar panels in the vicinity of the Jovian moon, Io with its harsh volcanic atmosphere, and greater than those experienced at the icy moon, *Europa*; both objects are of great scientific interest to the space exploration community, but are prohibitive to current III-V technology without thick and weighty cover glass [18]. Here, the radiation resistance of GaAsSb solar cells to 1 MeV electrons without a cover glass, indicates that a significantly thinner protection layer would be enough to

prevent degradation of these solar cells from high energy electrons. As such, less encapsulation would be required and GaAsSb based systems can then offer higher specific powers.

While the behavior of the irradiated cell is qualitatively similar to the reference, there are small variations upon closer inspection. Firstly, the PL spectrum of the irradiated cell has a more distinct feature related to the lower energy peak ascribed to localized states. This suggests that irradiation has increased the density of defect states within the material. This is perhaps not surprising as irradiation will inevitably create disorder and defects in the lattice through displacement of constituent elements and electron ionization. Figure 3 (b) indicates that irradiation does not (*apparently*) create new types of defect states, but rather contributes to the existing ones. This suggests that electron irradiation (or lighter particles, in general) advocate the same type of the defects that are generated in the system through increasing the Sb component. At low temperatures, the prevalent defect band has a marginally higher energy which is the case for the PL, in general (see Figure 3(c)). In fact, while the thermally induced redistribution of carriers is once more clear with temperature in the irradiated cell, the bandgap here has increased by $\sim 8\text{--}10$ meV (see Figure 3(c)). This observation suggests that the irradiation of the solar cell has induced some strain relaxation in the structure, perhaps associated with electron ionization and the propagation of energetic electrons during irradiation, which mainly causes local heating rather than nuclear displacement [29]. This phenomenon has certainly impacted the cell, but it does not seem to noticeably increase (or reduce) the density of the sub-gap impurity-related emission, as is seen in Figure 3(c), where the dependence of the emission has mainly scaled to higher energy upon irradiation. Further verification of change in band gap due to irradiation is observed in Figure 4(b) and (d), which show a comparison of the EQE of the cells before and after irradiation at 80 K and 300 K, respectively.

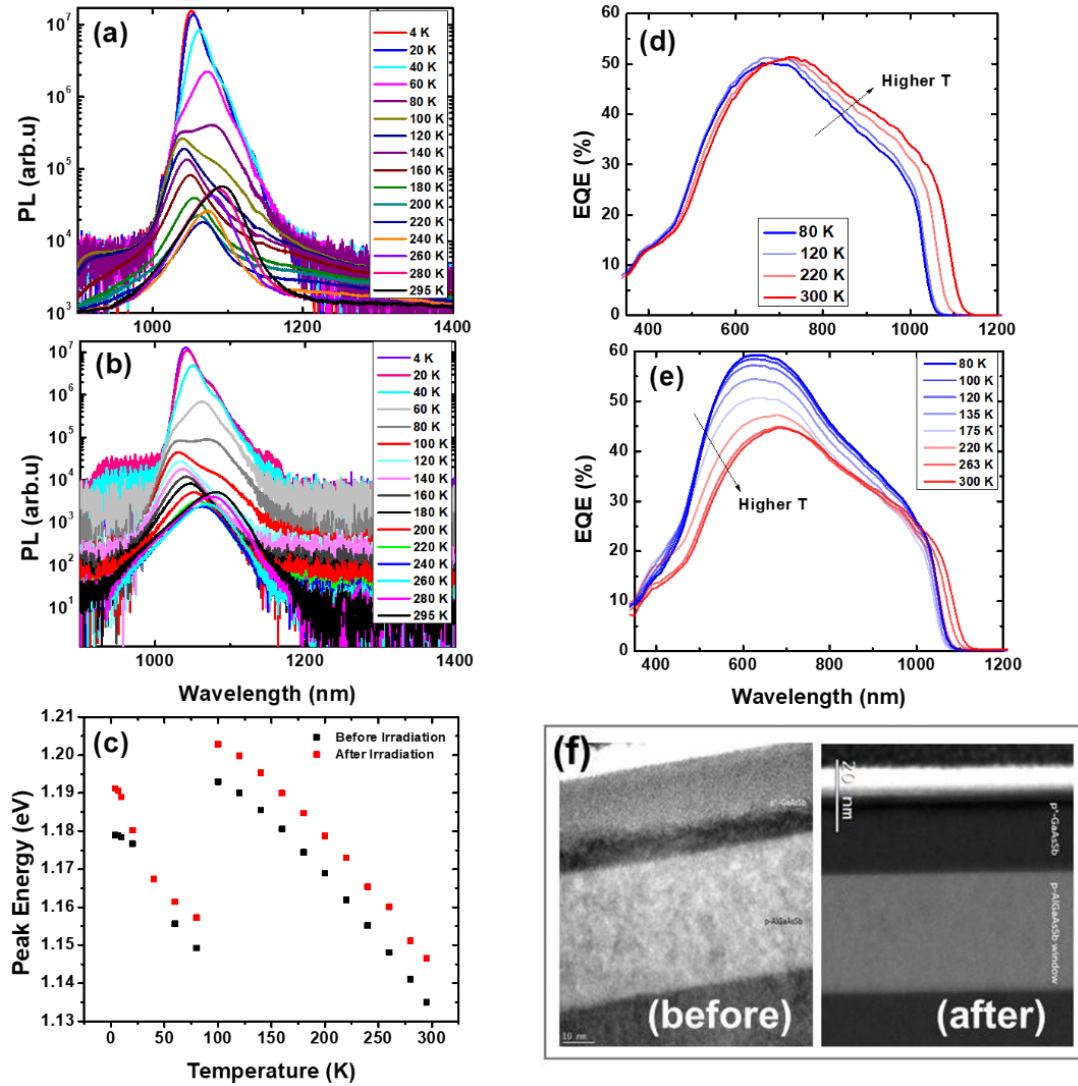


Figure 3. (a) Photoluminescence (PL) of the solar cell as a function of temperature: (a) prior to irradiation, and (b) after exposure to a 1 MeV electrons with a fluence of 1×10^{15} electron/cm². (c) Comparison of the peak PL position versus temperature for the pre- (solid black squares) and post- (solid red squares) electron irradiated solar cells as extracted from (a) and (b). EQE behavior of the GaAs_{1-x}Sb_x solar cells as a function of temperature before (d) and (e) after electron irradiation, respectively. (f) HR-TEM images of the upper p-AlGaAsSb/p+-GaAsSb interfaces before and after exposure to high-energy electron radiation [22].

To investigate the photovoltaic behavior of the solar cells in the energetic electron environments of space, temperature dependent EQE experiments are carried out pre and post exposure to electron irradiation. The acquired results are shown in Figure(s) 3(d) and (e), respectively. When comparing the response of the post and pre-irradiated cells it is clear that the low temperature (in particular) behavior of the cells is very different after irradiation. The as-grown solar cell (Figure 3(d)) manifests a rather typical redshift and increase in magnitude of the EQE with temperature; this is associated to the temperature dependence of the $\text{GaAs}_{0.86}\text{Sb}_{0.14}$ band gap and improved carrier extraction at high temperatures, as carriers gain thermal energy and escape the localizing states (as discussed in previous sections and verified in the PL spectrum – Figure 3(c)).

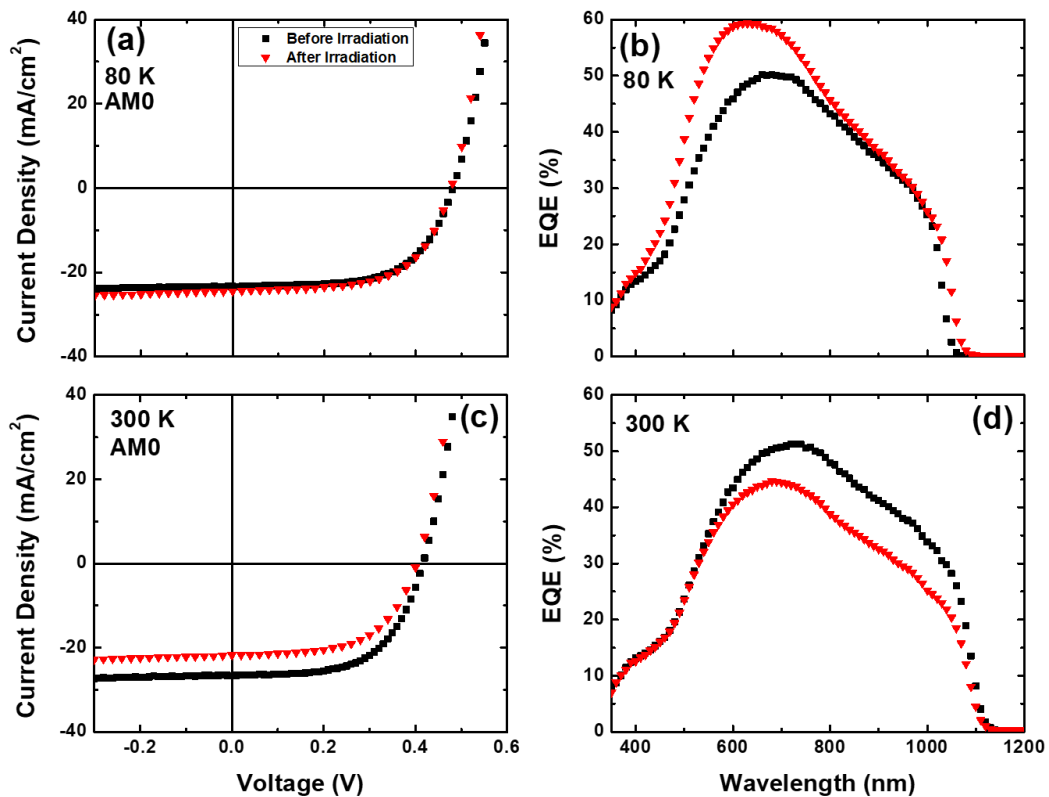


Figure 4. Current density – Voltage at AM0 of the $\text{GaAs}_{1-x}\text{Sb}_x$ solar cell before (solid black squares) and after (solid red triangles) electron irradiation at (a) 80 K and (c) 300 K. The associated EQE are shown in (b) at 80 K and (d) 300 K [22].

The irradiated cell, however, shows rather unusual features, as is illustrated in Figure 3(e). The low temperature EQE for this cell, which experienced exposure to an electron irradiation fluence of 1×10^{15} electrons/cm² has a *substantially higher* EQE at $T < 100$ K, particularly in the visible part of the spectrum. With increasing temperature, the EQE shifts, and quenches (more pronounced so at lower wavelength) reaching levels lower than those seen in the unirradiated (reference) solar cell at 300 K. This pattern can be more clearly seen in Figure 4, which presents direct comparisons of the J-V and EQE at 80 K and 300 K for the devices pre and post irradiation. Figure 4 (a) compares the light J-V data pre and post irradiation of the GaAs_{1-x}Sb_x solar cell under 1 Sun AM0 illumination at 80 K. The J_{SC} of the irradiated cell (24.5 mA/cm²) shown with solid red triangles is higher than that of the reference cell (23.3 mA/cm²) shown with solid black squares, while the difference in V_{OC} is negligible for the two cells at this temperature (80 K). The same behavior is also observed in Figure 4(b), which compares the EQE of the two cells, at 80 K. While the magnitude of J_{sc} extracted from the EQE are less than those given in the J-V analysis (Figure 4(a)) because of the lower illumination intensity used in the EQE experiments compared to the broadband irradiation of the solar simulator, the qualitative response seen in the EQE is the same, and the substantial increase in the EQE in the temperature regime upon irradiation is very clear in Figure 4(b). Interestingly, the change in the band gap seen in the PL *and* EQE after irradiation is not reflected in any substantial difference in V_{OC} for the irradiated cell, suggesting no appreciable increase in contribution of non-radiative recombination in the electron irradiated cell, *at low temperatures*. However, it should be noted that generally in this system there is an unusually large V_{OC} deficit. The V_{OC} at low (Figure 4(a)) and room temperature (Figure 4(c)), both pre and post irradiation, are considerably lower than what is expected for an absorber with a direct band gap of 1100 nm (1.12 eV), which would

ideally be around 0.7 eV. This V_{OC} deficit is the current limiting element of these cells, which needs attention before they can compete practically with state-of-the-art III-V solar cells. This loss of V_{OC} observed here is ascribed to the non-optimum architecture of the current cell structure, which was designed originally to investigate the potential to grow thick layers of strain compensated GaAsSb on GaAs. So, the current GaAsSb structures suffer substantial recombination losses across the thick intrinsic region due to alloy fluctuations, and the consequentially unintended high background impurity concentration in the absorber of the p-i-n structure.

The J-V and EQE data for the two cells at 300 K are compared in Figure 4(c) and (d), respectively. Unlike the results at 80 K, the relative performance of the before irradiation cell (solid black squares) out-performs that of the irradiated device (solid red triangles) at room temperature, as might be expected. The rather unusual behavior in the blue region of the spectrum at low temperatures observed in the TD EQE, and the transition to a behavior more consistent with the pre-irradiated cell at 300 K (see Figure(s) 3(e) and (d)) whilst requiring more investigation, seems to be associated with unavoidable local heating (or annealing) of the samples due to irradiation with energetic particles. Evidence of this hypothesis is seen in Figure 3(f) that shows HR-TEM image of the emitter and cap sections of the solar cell before (left) and after (right) electron irradiation. In the pre-exposed solar cells, the upper approximately two-thirds of the n^+ -GaAsSb cap is amorphous, probably due to the very large impurity density in this layer generated during MBE growth. While for the case of irradiated cell, the n^+ -GaAsSb is highly crystalline suggesting some form of annealing and enhancement of the layer after irradiation. This local heating of the sample is consistent with electron ionization mechanism when exposed to 1 MeV electrons, which is the dominant energy loss process when energetic

electrons pass through the cell, in this case stopping deep in the substrate of the structure. This enhanced crystallinity clearly boosts the extraction of charge carriers mainly at the top of the cell and at low temperature. The origin of the reduction in performance at high temperature is non-trivial and probably relates to the ionization of impurities at interfaces near the emitter region but, more work is required for a more rigid interpretation.

3.3 Change in the Pattern of the Temperature Dependent J-V

To further investigate this unusual response observed in the solar cells after electron irradiation temperature dependent J-V measurements are performed before and after irradiation, as shown in Figure 5. As seen, in this Figure the V_{OC} reduces with increasing temperature in both the as-grown and irradiated samples. This is partly due to the reduction of the effective band gap at higher temperatures reflected in the tail of the EQE seen in (Figure 3 (d) and (e)). For the J_{SC} , the behavior of the irradiated cell is the exact opposite of the as-grown cells. For the pristine cell, increasing the temperature results in increase in the J_{SC} , while for the irradiated cell J_{SC} reduces at higher temperatures. This is again, in agreement with the EQE data (Figure 3 (d) and (e)).

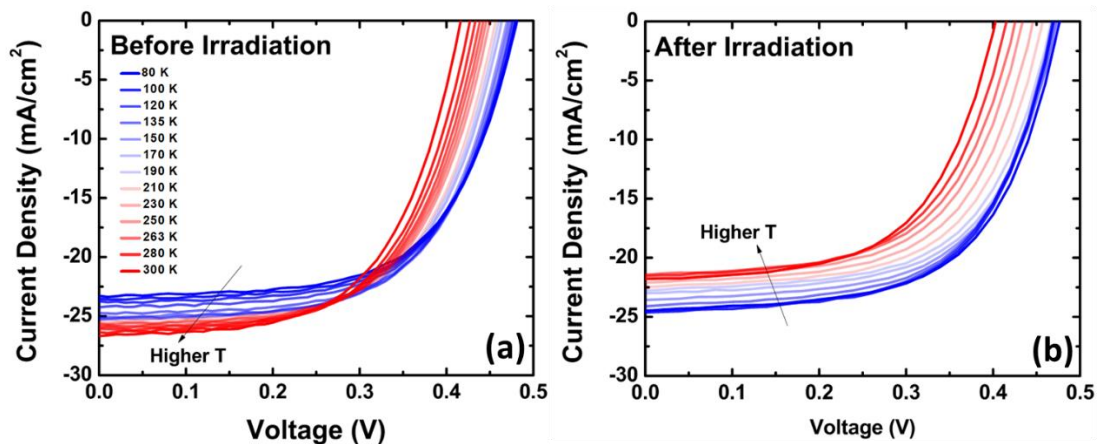


Figure 5. Temperature dependent J-V results from 80 K to 300 K before (a) and after irradiation (b). Blue color indicates the low temperatures and red color indicates the high temperatures [22].

The source of this behavior may be routed in that multiple way that electron interaction with lattice sites and the interfaces can affect a system. While more irradiation studies are needed to deliver a conclusion, it appears that irradiation improves some regions of the device, while damaging others. It is reasonable to assume that the high energy irradiation creates defect states that are activated at higher temperatures degrading the J_{SC} at such temperatures. But at the same time, enhanced J_{SC} at lower temperatures indicates improvement in some regions of the structure, which are believed to be related to local heating and/or micro annealing under irradiation.

3.4 Performance Under LILT Conditions of the Planets

To assess the capacity of the GaAsSb solar cells for outer planetary space missions, the fabricated cells were studied under the LILT conditions of the planets of Saturn, Jupiter, and Mars. The results for the three planets are presented in Figure 6. Regarding the J-V for the lower temperatures of Saturn (100 K) and Jupiter (135 K), as presented in Figures 6(a) and (b), only minor changes are evident in the pre- and post-irradiated solar cells. These minor changes are manifested in the irradiated cells as slightly higher J_{SC} at the conditions of Saturn, which is altered from 0.26 mA/cm² before, to 0.29 mA/cm² after irradiation, and at Jupiter from 0.93 mA/cm² to 0.99 mA/cm² after irradiation, while the V_{OC} experiences only a marginal reduction in these cases. In the case of Mars, (263 K) see Figure 6(c), the V_{OC} is not changing, while J_{SC} reduces from 13.8 mA/cm² to 11.3 mA/cm² after electron irradiation. The lower J_{SC} values at Saturn (0.011 Suns) as compared to Jupiter (0.037 Suns), and Mars (0.43 Suns), simply reflects the increasing solar irradiance received by the planets that are closer to the Sun. In practice, this means an adjusted AM0 spectrum for each of these systems; the corresponding contribution of which are shown, in Figure 6(a), (b), and (c).

In all cases studied (Saturn, Jupiter, and Mars), the reduction of the V_{OC} due to irradiation is negligible, and all the samples show a high level of radiation resistance under the LILT conditions assessed here. These data indicate the marginal influence on the dark J-V response due to irradiation, and infer small additional losses related to non-radiative recombination after irradiation. This rather unusual response is once again provisionally ascribed to the electron ionization and subsequent local heating of the crystal lattice due to exposure to the 1.0 MeV electron flux, which micro-anneals the solar cell decreasing some of the inhomogeneity and alloy fluctuations known to be present in most quaternaries, specifically the mixed group-V Sb alloys [27,28,30]. Such an annealing mechanism is supported by the improved crystallization of the n+-GaAsSb cap after irradiation, as seen in Figure 3(f). The EQE results of the irradiated samples in LILT conditions are presented in Figure(s) 6(d)–(f) for Saturn, Jupiter, and Mars, respectively. These EQE data support the J_{SC} values acquired in the light J-V scans shown in Figure(s) 6(a)–(c), as expected. In the case of Saturn and Jupiter, the magnitude of J_{SC} is higher after irradiation. Accordingly, an enhanced EQE is seen in the entire spectrum for the case of Saturn (d), and particularly at the lower wavelength region of the spectrum in the case of Jupiter (e). However, in the case of Mars at higher temperature there is a decrease in the EQE after irradiation agreeing with the J_{SC} , which is above the transition temperature seen in the temperature dependent EQE shown in Figure 3(e).

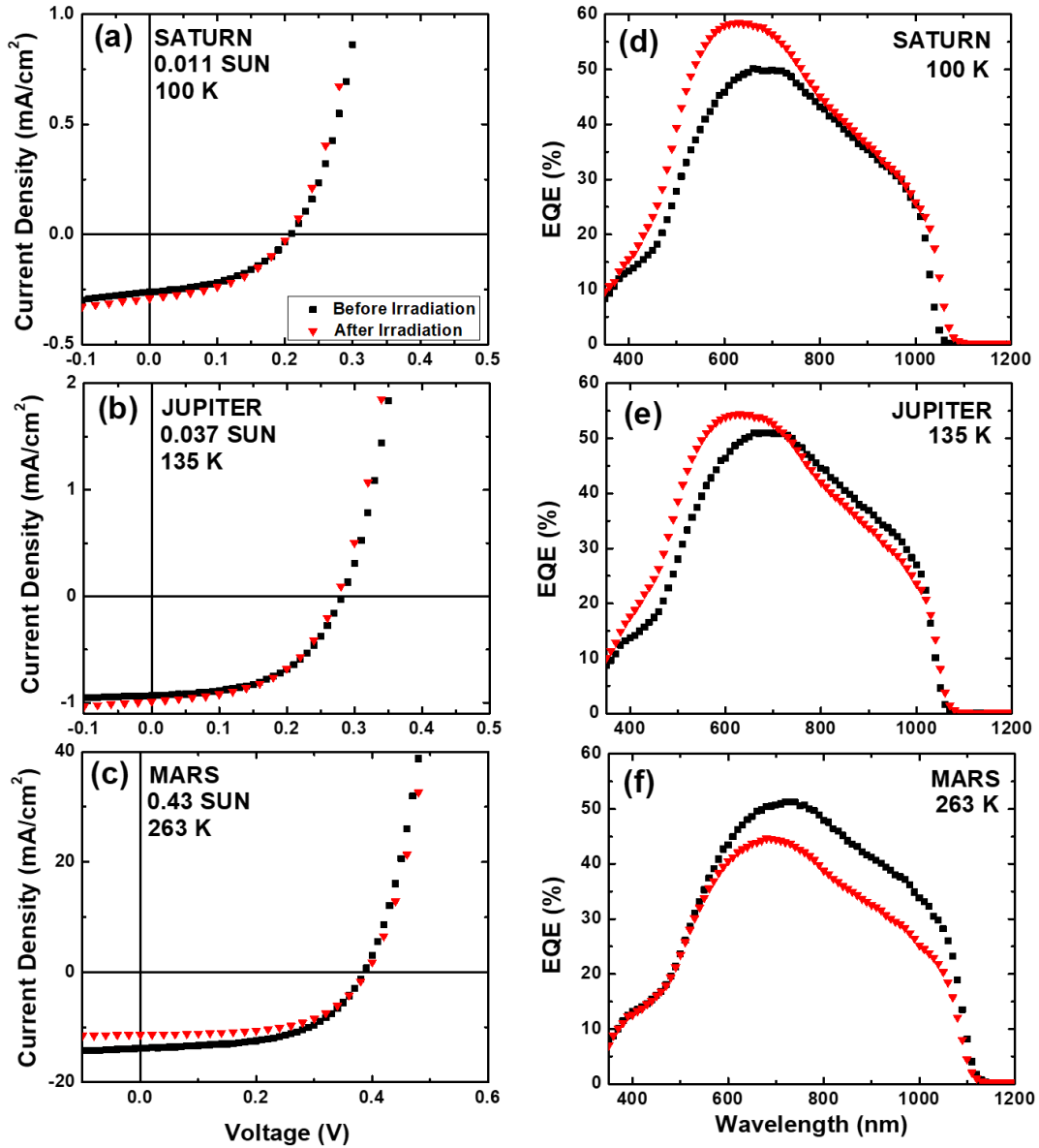


Figure 6. Current density-Voltage (J-V) measurements before and after irradiation for (a) Saturn, (b) Jupiter, and (c) Mars. The External Quantum Efficiency (EQE) results before and after irradiation are shown for Saturn, Jupiter, and Mars in (d), (e), and (f), respectively. The solid black squares show results before irradiation and the solid red triangles those data after irradiation [22].

This phenomenon of improved J_{SC} (and EQE) upon irradiation has been reported previously for III-V solar cells [12, 30], and recently in the perovskites cells [29]. These effects have been

ascribed to carrier removal and alteration of the doping profile of constituent layers due to irradiation, which can lead to expanded depletion region width translating in higher capacity for carrier extraction under specific circumstances [12, 29, 30]. Here, expansion of the depletion region width can be inferred from higher EQE for the lower wavelength part of the spectrum, which expands towards high wavelength at low temperatures in the irradiated solar cell. However, in order to have a better understanding of these effects, more irradiated GaAsSb cells with varied energy and fluence, are needed.

3.5 Conclusions

The radiation resistance of GaAs_{1-x}Sb_x solar cells is studied under the LILT conditions of Saturn, Jupiter, and Mars. High radiation tolerance is observed in PV parameters of the solar cells *after irradiation* particularly with respect to V_{OC} and FF. Moreover, an unusual temperature dependent behavior is seen for the J_{SC} of the cells including an enhancement (compared to pre-irradiation) at low temperatures and a degradation at higher temperatures, this is despite the fact that V_{OC} and FF are almost unchanged at all temperatures. The low temperature improvement in the J_{SC} of the irradiated cells resulted in an enhanced performance of the solar cells in the environments of Saturn and Jupiter. While some loss in performance of the irradiated cells is observed at the higher temperature and light intensity for Mars, these losses were for the most part in J_{SC} . These unusual behaviors, especially in the low temperature regime, are provisionally ascribed to local heating due to high energy irradiation, and defect passivation at lower temperatures, followed by ionization of impurities and decreased carrier collection at higher temperature.

3.6 References

- [1] T. Markvart, A. McEvoy, L. Castaner, Practical handbook of photovoltaics: fundamentals and applications, Elsevier, 2003.
- [2] S.A. Kalogirou, McEvoy's Handbook of Photovoltaics Fundamentals and Applications Third Edition, Academic Press, (2017).
- [3] M. Lumb, S. Mack, K. Schmieder, M. González, M. Bennett, D. Scheiman, M. Meitl, B. Fisher, S. Burroughs, K. Lee, J. Rogers, R. Walters, GaSb-Based Solar Cells for Full Solar Spectrum Energy Harvesting, *Advanced Energy Materials*, 7 (2017) 1700345.
- [4] M. Imaizumi, T. Nakamura, T. Takamoto, T. Ohshima, M. Tajima, Radiation degradation characteristics of component subcells in inverted metamorphic triple-junction solar cells irradiated with electrons and protons, *Progress in Photovoltaics: Research and Applications*, 25 (2017) 161-174.
- [5] J. Parravicini, F. Arcadi, A. Le Donne, R. Campesato, M. Casale, E. Greco, S. Binetti, Effect of the irradiation on optical and electrical properties of triple-junction flexible thin solar cells for space applications, *Frontiers in Physics*, 7 (2019) 169.
- [6] M. Yamaguchi, Radiation-resistant solar cells for space use, *Sol. Energy Mater. Sol. Cells*, 68 (2001) 31-53.
- [7] R.H.v. Leest, D. Fuhrmann, A. Frey, M. Meusel, G. Siefer, S.K. Reichmuth, Recent progress of multi-junction solar cell development for CPV applications at AZUR SPACE, *AIP Conference Proceedings*, 2149 (2019) 020007. 10.1063/1.5124177
- [8] A. Bett, D. Frank, W. Guter, R. Hoheisel, E. Oliva, S. Philipps, J. Schöne, G. Siefer, M. Steiner, A. Wekkeli, E. Welser, M. Meusel, W. Köstler, G. Strobl, Highest efficiency multi-

junction solar cell for terrestrial and space applications, 24th European Photovoltaic Solar Energy Conference and Exhibition, (2009).

[9] A. Khan, M. Yamaguchi, N. Dharmaras, T. Yamada, T. Tanabe, S. Takagishi, H. Itoh, T. Ohshima, M. Imaizumi, S. Matsuda, Radiation resistant low bandgap InGaAsP solar cell for multi-junction solar cells, Japanese Journal of Applied Physics, 40 (2001) L728.

[10] P. Colter, B. Hagar, S. Bedair, Tunnel junctions for III-V multijunction solar cells review, Crystals, 8 (2018) 445.

[11] I. Garcia, I. Rey-Stolle, C. Algora, Performance analysis of AlGaAs/GaAs tunnel junctions for ultra-high concentration photovoltaics, Journal of Physics D: Applied Physics, 45 (2012) 045101. 10.1088/0022-3727/45/4/045101

[12] L. Hirst, M. Yakes, J. Warner, M. Bennett, K. Schmieder, R. Walters, P. Jenkins, Intrinsic radiation tolerance of ultra-thin GaAs solar cells, Applied Physics Letters, 109 (2016) 033908.

[13] M. Sweeting, Modern small satellites-changing the economics of space, Proceedings of the IEEE, 106 (2018) 343-361.

[14] C.R. Brown, V.R. Whiteside, D. Poplavskyy, K. Hossain, M.S. Dhoubhadel, I.R. Sellers, Flexible Cu(In,Ga)Se₂ Solar Cells for Outer Planetary Missions: Investigation Under Low-Intensity Low-Temperature Conditions, IEEE Journal of Photovoltaics, 9 (2019) 552-558. 10.1109/JPHOTOV.2018.2889179

[15] H. Afshari, B.K. Durant, C.R. Brown, K. Hossain, D. Poplavskyy, B. Rout, I.R. Sellers, The role of metastability and concentration on the performance of CIGS solar cells under Low-Intensity-Low-Temperature conditions, Sol. Energy Mater. Sol. Cells, 212 (2020) 110571.

<https://doi.org/10.1016/j.solmat.2020.110571>

- [16] C. Brown, G. Eperon, V. Whiteside, I. Sellers, Potential of high-stability perovskite solar cells for low-intensity–low-temperature (LILT) outer planetary space missions, *ACS Appl. Energy Mater.*, 2 (2018) 814-821. <http://dx.doi.org/10.1021/acsaem.8b01882>
- [17] F. Lang, M. Jošt, K. Frohna, E. Köhnen, A. Al-Ashouri, A.R. Bowman, T. Bertram, A.B. Morales-Vilches, D. Koushik, E.M. Tennyson, Proton Radiation Hardness of Perovskite Tandem Photovoltaics, *Joule*, (2020).
- [18] G.A. Landis, J. Fincannon, Study of power options for Jupiter and outer planet missions, in: 2015 IEEE 42nd Photovoltaic Specialist Conference (PVSC), IEEE, 2015, pp. 1-5.
- [19] H. Liu, I. Sellers, M. Gutierrez, K. Groom, W. Soong, M. Hopkinson, J. David, R. Beanland, T. Badcock, D. Mowbray, Influences of the spacer layer growth temperature on multilayer InAs/GaAs quantum dot structures, *Journal of applied physics*, 96 (2004) 1988-1992.
- [20] I.R.S. H.Y. Liu, T.J. Badcock, D.J. Mowbray, M.S. Skolnick, K. M. Groom, M. Gutierrez, M. Hopkinson, J. S. Ng, J. P. R. David, and R. Beanland, Optimizing the growth of 1.3 μm multi-layer quantum dot lasers using a high-temperature-growth GaAs spacer layers, *Appl. Phys. Lett.*, 85 (2004) 704-706.
- [21] F. Tutu, I. Sellers, M. Peinado, C. Pastore, S. Willis, A. Watt, T. Wang, H. Liu, Improved performance of multilayer InAs/GaAs quantum-dot solar cells using a high-growth-temperature GaAs spacer layer, in, American Institute of Physics, 2012.
- [22] H. Afshari, B.K. Durant, T. Thrasher, L. Abshire, V.R. Whiteside, S. Chan, D. Kim, S. Hatch, M. Tang, J.S. McNatt, Radiation tolerance of GaAs_{1-x}Sb_x solar cells, *Sol. Energy Mater. Sol. Cells*, 233 (2021) 111352.
- [23] Y.P. Varshni, Temperature dependence of the energy gap in semiconductors, *Physica*, 34 (1967) 149-154.

- [24] C.R. Brown, N.J. Estes, V.R. Whiteside, B. Wang, K. Hossain, T.D. Golding, M. Leroux, M. Al Khalfioui, J.G. Tischler, C.T. Ellis, E.R. Glaser, I.R. Sellers, The effect and nature of N–H complexes in the control of the dominant photoluminescence transitions in UV-hydrogenated GaInNAs, *RSC Advances*, 7 (2017) 25353-25361. [10.1039/C7RA02900D](https://doi.org/10.1039/C7RA02900D)
- [25] T. Nuytten, M. Hayne, B. Bansal, H.Y. Liu, M. Hopkinson, V.V. Moshchalkov, Charge separation and temperature-induced carrier migration in Ga_{1-x}In_xNyAs_{1-y} multiple quantum wells, *Physical Review B*, 84 (2011) 045302. [10.1103/PhysRevB.84.045302](https://doi.org/10.1103/PhysRevB.84.045302)
- [26] H. Esmailpour, V.R. Whiteside, L. Hirst, J. Tischler, R. Walters, I. Sellers, The effect of an InP cap layer on the photoluminescence of an In_xGa_{1-x}As_QyPy/InzAlQ_zAs quantum well heterostructure, *Journal of Applied Physics*, 121 (2017) 235301.
- [27] S. Tomasulo, M. Gonzalez, M.P. Lumb, C.R. Brown, A.H. Dicarolo, I.R. Sellers, I. Vurgaftman, J.R. Meyer, R.J. Walters, M.K. Yakes, Effect of molecular beam epitaxy growth conditions on phase separation in wide-bandgap InAlAsSb lattice-matched to InP, *Journal of Crystal Growth*, 548 (2020) 125826. <https://doi.org/10.1016/j.jcrysgro.2020.125826>
- [28] X. Gao, Z. Wei, F. Zhao, Y. Yang, R. Chen, X. Fang, J. Tang, D. Fang, D. Wang, R. Li, Investigation of localized states in GaAsSb epilayers grown by molecular beam epitaxy, *Scientific reports*, 6 (2016) 29112.
- [29] B.K. Durant, H. Afshari, S. Singh, B. Rout, G.E. Eperon, I.R. Sellers, Tolerance of Perovskite Solar Cells to Targeted Proton Irradiation and Electronic Ionization Induced Healing, *ACS Energy Lett.*, 6 (2021) 2362-2368. <https://doi.org/10.1021/acsenergylett.1c00756>
- [30] R.J. Walters, S. Messenger, J.H. Warner, C.D. Cress, M. Gonzalez, S. Maximenko, Modeling of radiation induced defects in space solar cells, in: *Physics and Simulation of Optoelectronic Devices XIX*, International Society for Optics and Photonics, 2011, pp. 79330P.

Chapter 4

Excitons and Carrier Extraction in Perovskite Solar Cells

The optoelectronic properties of perovskites are influenced by the formation and mobilization of excitons, especially at low temperatures [1, 2]. Indeed, the large absorption coefficients and strong radiative emission in these systems are a result of the excitonic properties of this family of materials [1]. Given that free charge carriers and excitons have different transport properties, it is crucial to comprehend and consider their dynamics in the transport properties of perovskites. Additionally, excitons impact the band-edge states in perovskites, which ultimately affects the performance of perovskite solar cells and their transport properties. Therefore, determining the implications of such dynamics in perovskite systems is necessary for their commercialization [1, 3].

Excitonic effects in semiconductor devices are typically observed at lower temperatures because the binding energy of these complexes is less than 25 meV in most cases [1, 4]. While the perovskite systems have exciton binding energies ranging from a few to hundreds of meV [1, 3], in all cases the effects of excitons are screened less by disorder and phonons at lower temperature enabling better understanding of the physics in these regimes [5-7]. Therefore, investigations of excitonic effects in perovskites are ideally conducted at low temperatures. However, there have been relatively few studies of perovskite solar cells under these conditions, and little is known about the relationship between recombination dynamics and carrier transport in this regime. This is largely due to the fact that the implementation of solar panels that primarily drives this research normally operate at approximately 300 K, so most of the research on perovskite solar cells focuses on achieving stability at ambient conditions. Nonetheless, low-

temperature measurements can yield valuable insights into the fundamental physics underlying solar cell performance [8-10], as well as the role of parasitic processes in determining performance, stability, and longevity.

When it comes to extraterrestrial applications, such as a power generation system for satellites, extra factors are necessary to support operation in these environments. In outer space, there are certain environmental factors such as decreased pressure, extreme temperatures, and high levels of radiation that solar panels designed to function in space must endure. Perovskite solar cells have garnered significant recent attention for space applications due to their high radiation tolerance in space conditions, [11-13] which is rooted in the soft nature and flexible crystal structure of the material that reduce defect formation and stabilization and facilitate self-healing [14, 15]. However, because these systems would also experience wide temperature swings in space (ranging from - 100 °C to 100 °C in LEO), it is crucial to study their low-temperature performance for such applications [12, 16].

In this study, the behavior of $\text{Cs}_{0.05}\text{FA}_{0.79}\text{MA}_{0.16}\text{Pb}(\text{I}_{0.83}\text{Br}_{0.17})_3$ perovskite solar cells are investigated as they undergo thermal cycles from low to high temperatures in order to monitor the evolution of their properties. Figure 1 presents the schematic details of the studied solar cells studied here. The SnO_2 electron transport layer (ETL) and a SPIRO hole transport layer (HTL) encapsulate the perovskite absorber layer. A layer of MoO_3 is added on top of the SPIRO to enhance interfacial properties, prevent diffusion, and improve carrier extraction. The solar cell structure, including the thickness of each layer, is illustrated in Figure 1(a). The thicknesses have been carefully optimized to achieve maximum performance of the devices derived from these materials. The band alignment of the system is depicted in Figure 1(b). The heterostructure architecture of the $\text{Cs}_{0.05}\text{FA}_{0.79}\text{MA}_{0.16}\text{Pb}(\text{I}_{0.83}\text{Br}_{0.17})_3$ based solar cell, which has an energy band

gap of ~ 1.62 eV, facilitates the transport of electrons and holes to the electrical contacts of the device.

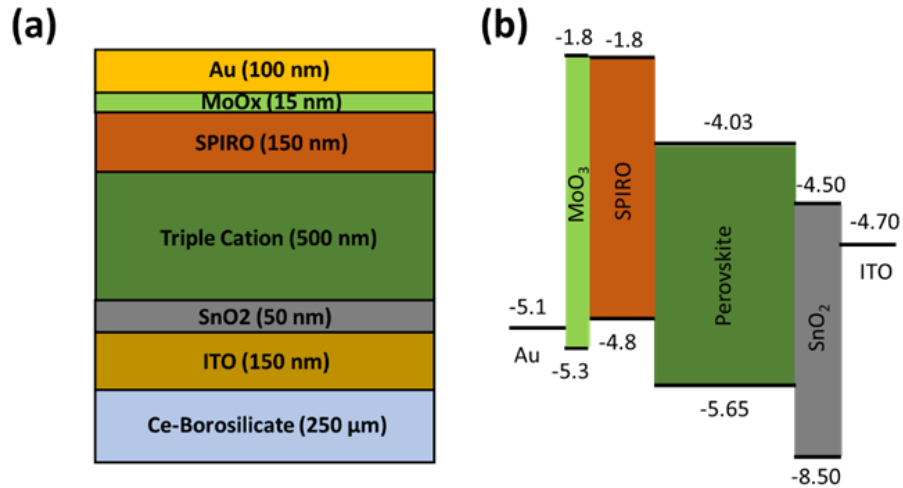


Figure 1. (a) Structure of the Perovskite solar cell. (b) Energy band alignment of the solar cell.

Figure 2(a) shows the temperature-dependent current density-voltage (J-V) characteristics of the solar cell under AM 1.5G illumination measured between 85 K to 290 K. At 85 K, the photogenerated current at short circuit (J_{sc}) is minimal. However, as the temperature increases, the photocurrent gradually improves until it reaches a saturation point. The fill factor (FF) of the solar cell also shows a similar trend. At lower temperatures, the photocurrent exhibits a strong voltage dependence with a low FF, indicating the presence of an extraction barrier and/or pinning of the Fermi level. Figure 2(b-d) illustrates the suggested barrier, and the role of excitons at different temperatures. Noticeably, extraction of both majority and minority carriers is inhibited at low temperatures, leading to a small current above the V_{oc} point as well. This suggests the presence of additional series resistance in the system, arising from a failure to conduct in one or more layers and/or an interface barrier hindering carrier transport. The reduced J_{sc} and other PV parameters at very low temperatures may also be simply rooted in changes in electronic properties and morphology of the charge transport layers. Hence, for perovskite solar

cells to function well at low temperatures such as in space, consideration must be given to both the perovskite absorber and the constituent transport and interfacial layers.

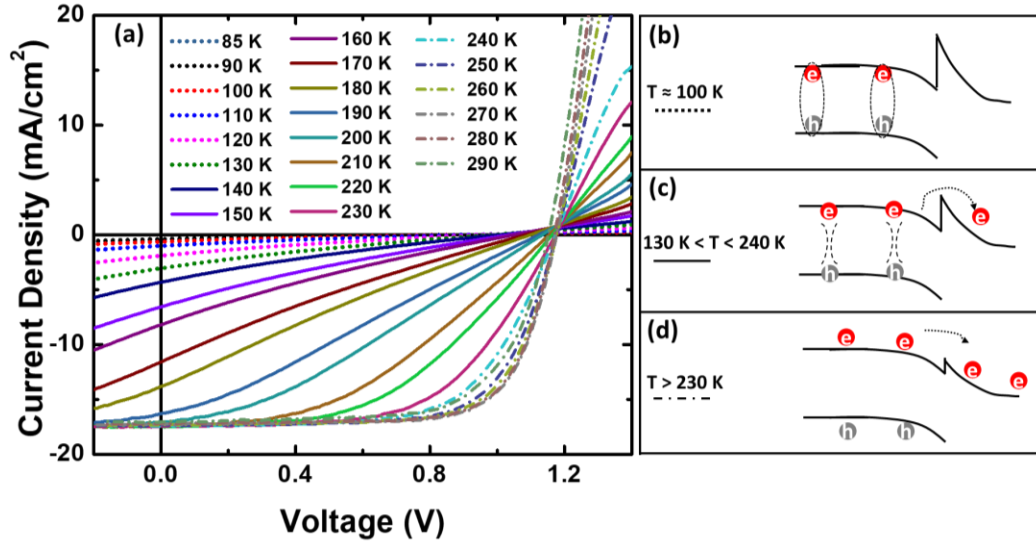


Figure 2. (a) J-V response as a function of temperature. (b-d) Diagrammatic representations of the extraction of charge carriers and excitons under different temperature conditions where the extraction of carriers is influenced by excitonic recombination, thermionic emission, and/or their thermal energy. These conditions occur at temperatures of 100K, 140 K to 250 K, and at 300 K, respectively.

Figure 2(a) illustrates three temperature regimes that effect the carrier transport and extraction in the solar cell. The low-temperature regime ($T \leq 100$ K) is represented by dotted lines, which are also schematically illustrated in Figure 2(b). In this regime, both the excitonic nature of the system and a parasitic barrier to photogenerated carrier extraction cause perturbations in carrier transport and collection. The intermediate regime, shown as solid lines in Figure 2(a) —occurring between $T \sim 140$ K and $T \sim 250$ K— exhibits an increase in the ionization and thermal energy of the carriers, which enhances their ability to be collected in the electrodes of the solar cell. This is schematically illustrated in Figure 1(c). Figure 2(d) represents the optimum regime for carrier extraction and efficient PV operation for this perovskite system, which occurs at $T > 250$ K and

is indicated by dash-dot lines in the Figure. In this regime, the barrier to photogenerated carriers is reduced due to their higher thermal energy ($k_B T$) resulting in lower resistance to carrier transport, as well as large currents and voltages under illumination and improved FF.

4.1 Discrepancy Between External Quantum Efficiency and Light J-V Measurements

Figure 3(a) illustrates the temperature dependent EQE data ranging from 90 K to 300 K. Despite retaining their shape, the EQE spectra displays a reduced magnitude at lower temperatures, which increases as the temperature rises. This indicates inhibited carrier extraction at lower temperatures, which is consistent aligns with the J_{sc} response observed. The uniform loss of EQE with temperature implies a barrier to *all* minority carriers absorbed in the structure (i.e., the loss is not related to a specific region of the devices), which is typical of a parasitic barrier at the absorber transport layer interface that perturbs the diffusion and extraction of *all* photogenerated carriers. Although the qualitative EQE and J_{sc} trends concur, there is a notable quantitative discrepancy between these data. While the low-temperature EQE results reveal greater extraction efficiency at lower temperatures (Figure 3(a)), the J_{sc} extracted from the 1 Sun J–V measurements exhibit negligible charge extraction (lower current - see Figure 2(a) and 3(b)). Specifically, at $T = 90$ K, the light J–V measurement yield a J_{sc} of 0.45 mA/cm^2 ; however, the J_{sc} value extracted from the EQE measurement at the same temperature ($T = 90$ K) is $\sim 14 \text{ mA/cm}^2$.

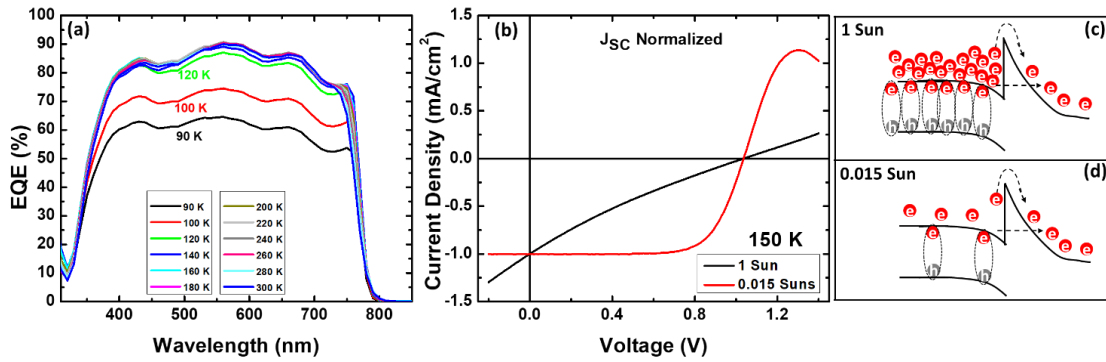


Figure 3. (a) EQE measured between 90 K and 300 K. (b) Normalized J_{SC} at for two different illumination intensities (1 Sun AM 1.5G (black) and 0.015 Sun (red)) at 150 K. The diagram in (c) and (d) demonstrate the proposed increase in excess carrier concentration at low temperatures for 1-Sun AM0 due to limited thermionic emission and inhibited carrier extraction, and the improved balance between carrier generation and thermionic extraction at lower fluences for 0.015 Sun at the same temperature, leading to higher relative carrier extraction for low carrier densities.

It should be noted that there are differences in the measurements that may explain the inconsistencies observed in the extracted photocurrent density when comparing J-V and EQE. Specifically, the light sources used for the EQE, and J-V measurements differ in several ways. In EQE measurements, a monochromatic light is used, which scans a wide range of wavelengths from 300 nm to 1100 nm in a step like fashion. Conversely, the J-V measurements are performed under AM 1.5G broadband illumination that include naturally all wavelengths of the solar spectrum. Additionally, the optical excitation intensity in the EQE measurements is substantially lower than that of AM 1.5G from the solar simulator. These differences can impact the role of defects and non-idealities in the system causing perturbations in carrier extraction.

To evaluate how illumination intensity affects solar cell performance, the solar simulator light intensity was reduced to a level similar to that of the EQE system (0.015 Sun). J-V

measurements were then re-taken at a temperature of 150 K, where the J_{sc} and V_{oc} values had yet to reach their stable point (as seen in Figures 2(a) and 3(b)). Figure 3(b) presents a comparison of the normalized (J_{sc}) light J-V measurements taken at 1 Sun AM 1.5G and 0.015 Sun at 150 K. While the cells J-V response under AM 1.5G exhibited little rectifying behavior, and resembled that of a resistor, at 0.015 Sun concentration, the photovoltaic parameters were restored. Interestingly, despite the difference in intensity, V_{oc} remained unchanged with variations in fluence. This suggests that the main effect of inhibited carrier extraction is to limit carrier collection, rather than enhance parasitic recombination losses as demonstrated by the unnormalized data presented (and discussed) in Figure 4.

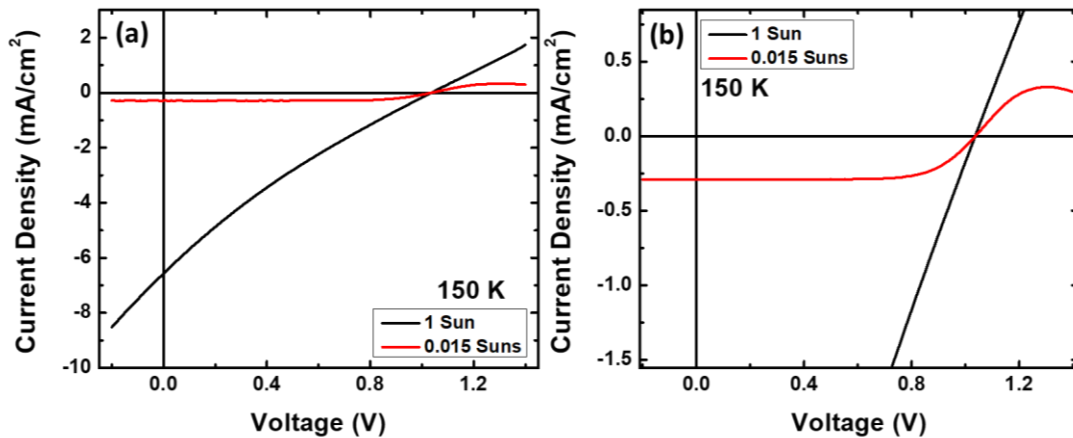


Figure 4. (a) Light J-V of the $\text{CS}_{0.05}\text{FA}_{0.79}\text{MA}_{0.16}\text{Pb}(\text{I}_{0.83}\text{Br}_{0.17})_3$ based perovskite solar cell at 150 K under low and high illumination intensities. The red curve shows results of illumination with 0.015 Suns and the black curve shows the results for 1 Sun AM1.5G (b) Light J-V results zoomed in on the 0.015 Suns results to show the PV parameters are restored for this *lower* illumination intensity.

The hypothesis of the presence of a parasitic barrier at an interface that inhibits carrier transport is supported by the intensity dependence of the J-V measurements and the monotonic reduction in the EQE spectrum with increasing temperature. In such a scenario, carrier extraction is

influenced by two competing factors: photogeneration and thermionic emission extraction of the carriers. At low temperatures and high incident illumination, the photogeneration rate surpasses thermionic emission across the parasitic barrier. As a result, only a portion of the photogenerated carriers can cross the interface, increasing resistance and leading to a low fill factor (FF) and subsequently, reducing the power conversion efficiency. This situation is depicted in Figure 3(c). However, when the light intensity (and thus the photogeneration rate) is decreased, the thermionic emission dominates and carrier extraction increases. This results in an enhanced FF and efficiency of the solar cell, as demonstrated in Figure 3(d). These findings align with earlier studies on perovskite solar cells under low-intensity, low-temperature (LILT) conditions, which displayed similar behavior [6].

4.2 Ionization of Excitons: Temperature Dependent Photoluminescence

Figure 5(a) depicts the temperature-dependent photoluminescence (PL) from 4.2 K to 295 K, where the dotted line serves as a guide-to-the-eye. As the temperature increases, the PL intensity decreases, the peak energy undergoes a blue shift, and the spectra broaden. Figure 5(b) further demonstrates these changes by displaying the integrated PL intensity as a function of temperature, as obtained from the data (represented by solid black squares) in Figure 5(a).

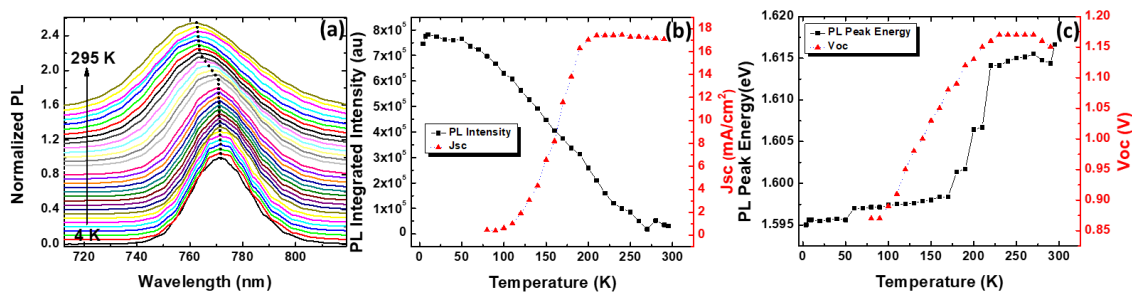


Figure 5. (a) The photoluminescence of the solar cell exhibits temperature dependence over a range of 4 K to 295 K. The dotted line is a guide-to-the-eye. (b) The integrated intensity data extracted from (a) and

the J_{sc} data obtained from Figure 1(a) both vary as a function of temperature. (c) The peak energy data extracted from Figure 3(a) and the V_{oc} data from Figure 1(a) both exhibit temperature dependence.

The blue shift in the PL peak energy is attributed to the increase in the band gap of the perovskite material with temperature, which is a unique characteristic of metal halide perovskites [17, 18], which is opposite to that of the traditional III-V semiconductors, or silicon. The broadening of the PL can be explained by the increased Fröhlich interaction at temperatures exceeding 30 K. [19] According to these data the decrease in the radiative efficiency of the perovskite is not *primarily* due to the activation of non-radiative losses, but rather it results from improved carrier extraction and device performance at elevated temperatures. This is evident when comparing the temperature dependence of the J_{sc} (represented by solid red triangles) in Figure 5(b), which is negligible between 85 K and 100 K ($\sim 0.3 \text{ mA/cm}^2$), and then rapidly rises after 100 K, reaching approximate saturation at $> 200 \text{ K}$.

Figures 5(b) and (c) Show the variations in J_{sc} and V_{oc} as extracted from Figure 2(a). These results demonstrate that both J_{sc} and V_{oc} exhibit low values at lower temperatures but increase as the temperature increases. Between 200 K and 220 K, both parameters reach a stable maximum. The decrease in V_{oc} suggests a voltage drop at one of the interfaces, which may be due to the temperature-dependent nature of the constituent layers resulting in barriers at various interfaces at low temperature. However, these barriers are eliminated at $T > 200 \text{ K}$, which is much lower than the standard operating temperature for such solar cells. In perovskite solar cells, FF loss at low temperatures has been attributed to a combination of restricted carrier transport in the perovskite absorber, non-ideal heterojunction offsets [18], and low conductivity of the transport layers at low temperatures, [18, 20] as discussed previously.

It should be stressed that when examining the quenching of photoluminescence (PL) intensity and the extraction of photocurrent, a (negative) correlation is observed between PL intensity and carrier extraction (J_{sc}), which further implies, that the loss of PL is not due to increased non-radiative processes such as due to defects or non-idealities. Indeed, the reduction in PL intensity is rather a result of the rapid extraction of photogenerated carriers between 100 K and 200 K. Additionally, the constant and relatively low PL observed at $T > 250$ K when the solar cell is performing at its best (refer to Figure 2) indicates that the solar cell remains mainly within the radiative limit and any uncollected carriers recombine radiatively. This is supported by the significant temperature dependence of the V_{OC} (~ 1.15 V) above 200 K, as displayed in Figure 5(c). At $T \sim 85$ K, V_{OC} is ~ 0.85 V and increases to 1.15 V at 200 K, where it approximately saturates up to room temperature.

Increased non-radiative processes are often evidenced by an increase in the dark current and subsequent loss of V_{OC} . However, unlike the temperature-dependent reduction in PL, which does not result in simultaneous loss of V_{OC} , the poor performance of the device at lower temperatures can be attributed to the role of parasitic barriers, low thermal energy of carriers, as well as non-ideal current extraction —due to lower thermionic emission— at high excitation. Furthermore, since the band gap of perovskites increases at higher temperatures the increased voltage likely reflects the increasing band gap of the absorber and more optimal band offsets at temperatures above 200 K. This hypothesis is supported by the temperature-dependent dark J-V data presented in Figure 6, which demonstrate the very high resistance against carrier extraction at low temperatures, indicating the presence of a barrier to carrier extraction at such temperatures. Carrier transport is improved at higher temperatures.

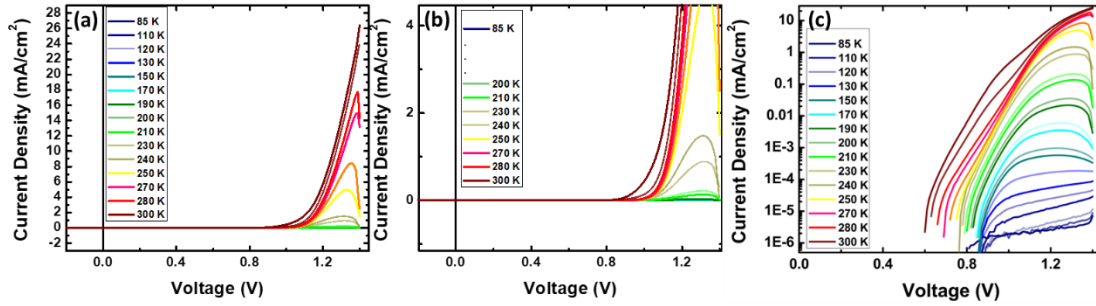


Figure 6. (a) Temperature dependent dark J-V of the solar cell from 85 K up to 300 K (b) Magnified dark J-V results at low temperatures to illustrate the effect of high series resistance in this regime, which is reflected in almost flat horizontal J-V curves with minimal rectification, at very low temperatures. (c) Temperature dependent dark J-V plotted in a log scale to show details of low and high temperature behavior of the cell. There is a high series resistance at very low temperatures reducing the majority carrier extraction, which is reflected in almost flat J-V curves at low temperatures.

While the solar cell shows different modes of performance at various temperatures, signatures of the excitons also manifest in various experiments. One of these is a sudden increase in the photoluminescence (PL) peak position at ~ 170 K, increasing from approximately 1.597 eV to 1.615 eV, as reflected in the significant shift of the PL spectra at higher temperatures in Figure 5(a). This shift in energy can be explained via the ionization of excitons as temperature increases. Although perovskite materials are known to experience structural phase transitions with increasing temperature, this phenomenon typically leads to a sudden *decrease* in the band gap. In contrast, Figure 5(a) shows an *increase* in the peak PL energy, suggesting an alternative effect. Additionally, the heat map in Figure 8 shows a monotonic increase in the PL energy with temperature, indicating the absence of any significant phase transition in this system within the temperature range studied (4.2 K to 295 K).

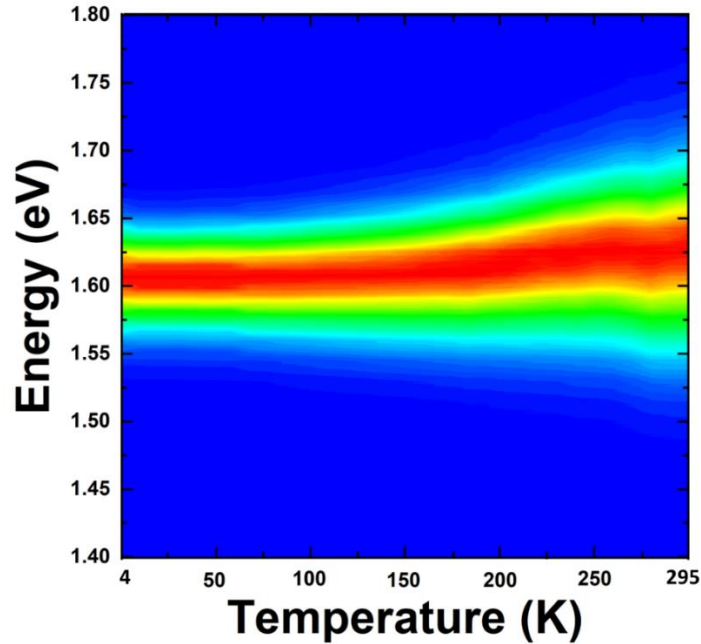


Figure 7. Heat map of the temperature dependent photoluminescence from the (FACs)Pb(BrCl)₃ absorber from 4.2 K to 295 K. The lack of a sudden reduction in energy in this temperature window excludes the occurrence of a structural phase transition for the system under study in this temperature range.

A clear correlation exists between the ionization of excitons and the behavior of V_{OC} and J_{sc} with temperature as shown in Figure 5(b) and (c). As the temperature increases, the thermal energy increases gradually ionizing the excitons, resulting in an increase in both V_{OC} and J_{sc} . In addition, or simultaneously, the absorption edge also blueshifts above $T \sim 170$ K, eventually reaching a plateau at ~ 210 K when the system's thermal energy ($k_B T$) exceeds that of the exciton binding energy, indicating a complete transition to the free excitonic regime.

4.3 Ionization of Excitons in Temperature Dependent EQE

The observed increase in peak energy at $T \sim 170$ K in the PL spectra is attributed to the ionization of excitons and the subsequent transition of the absorption edge to that of the continuum after the annihilation of the excitonic species. This hypothesis is reinforced by the EQE shown in Figure 8(a), where the normalized low (77 K) and high (300 K) temperature EQE exhibits clear evidence of exciton absorption and its subsequent quenching at higher temperature. While the excitonic complex, E_x , is evident at low temperatures, it merges into the continuum, E_c , at higher temperatures. Figure 8(b) illustrates the changes in exciton ionization by focusing on the temperature dependent EQE between 160 K and 300 K. At 160 K, the EQE of the solar cell exhibits a peak on the lower energy tail of the EQE indicative of strong excitonic absorption. As the temperature increases, the excitonic transition weakens and broadens into the continuum and loses dominance at temperatures exceeding 200 K. The impact of excitons at low temperatures can also be observed by comparing the emission (PL) and absorption (EQE) at various temperatures throughout the transition from excitons to the free carrier regime.

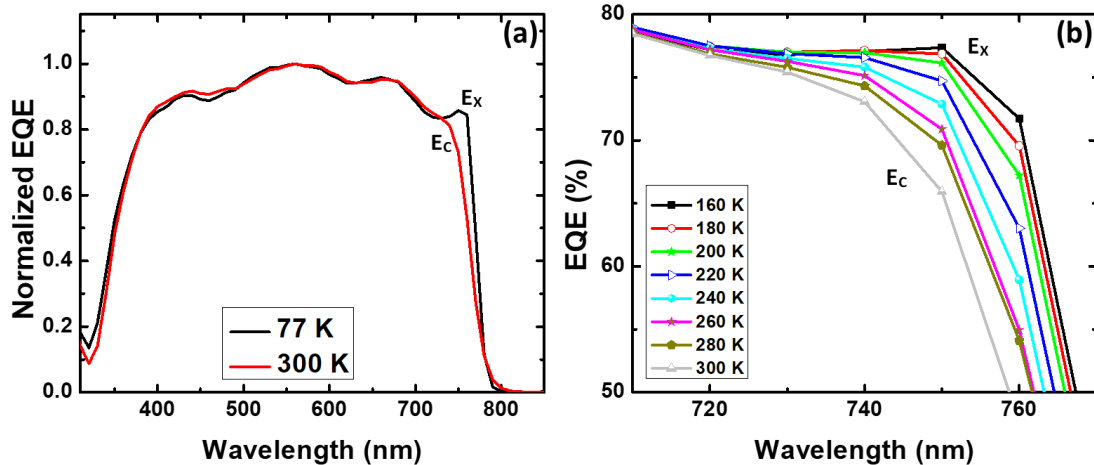


Figure 8. (a) The EQE of the solar cell, normalized to room temperature at both 77 K and 300 K. (b) A detailed view of the temperature dependent EQE, focusing on the exciton region.

4.4 Comparing Ionization of Excitons Observed in PL and EQE

Figure 9(a-c) illustrates a comparison between the PL and EQE at different temperatures (90 K, 180 K, and 280 K) focusing on the low energy region (absorption edge) of the EQE spectra. The goal is to allow for easier assessment of the shift and broadening of the PL and dynamics of low energy tail of the EQE. At 90 K, the EQE is dominated by the excitonic nature of the systems, as seen by the strong exciton absorption at the band edge and the narrow and intense PL. As temperature increases to approximately 180 K, the continuum begins to dominate the EQE, and the PL broadens through a combination of enhanced carrier-phonon interactions, reduced radiative efficiency, and more efficient free carrier extraction (Figure 10(b)). This is reflected in the increase in both J_{sc} and total EQE at higher temperatures, as shown in Figure 3. At 280 K, the EQE is dominated by band-to-band continuum related absorption and the associated PL is significantly broadened due to the strong Fröhlich coupling [21] inherent in the strongly polar metal halide perovskite.

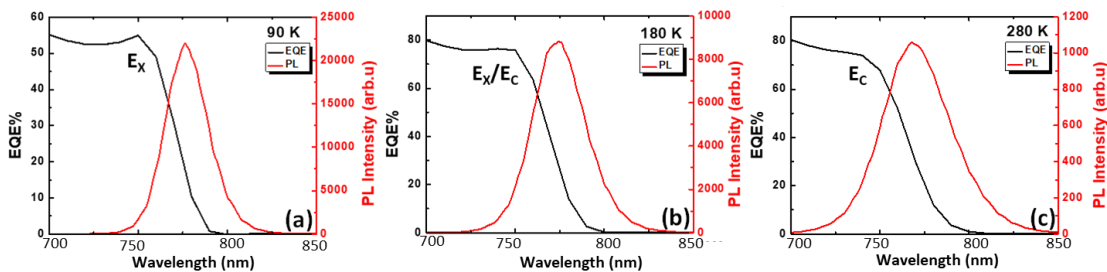


Figure 9. Comparison of the EQE (Black) at the absorption edge and PL (Red) at: (a) 90 K; (b) 180 K; and; (c) 280 K.

4.5 Temperature Dependence of the Exciton Binding Energy

Comprehending the impact of carrier localization (due to band offsets at heterointerfaces, and the effect of exciton binding energy) can be achieved by analyzing the temperature-dependent PL intensity and the J_{sc} through complementary Arrhenius analysis.

$$I(T) = \frac{I_0}{1 + a \cdot \exp\left(\frac{-E_x}{k_B T}\right) + b \cdot \exp\left(\frac{-E_b}{k_B T}\right)}. \quad (1)$$

Here, the coefficients and energies associated with various activation processes are represented by a , b , E_x , and E_b , while T and k_B represent temperature and Boltzmann constant, respectively.

At 4.2 K, the initial integrated PL intensity is denoted by I_0 .

Figure 10(a) summarizes the correlation between the integrated PL intensity and temperature. To determine the activation energies, an Arrhenius fit is used. The data suggests two activation energies, approximately 26 meV and 143 meV, respectively, which are attributed to the exciton binding energy, E_x , and a parasitic barrier, E_b , respectively. The inset in Figure 10(a) illustrates the respective roles of these processes. The exciton binding energy value is consistent with previous studies of this system [1, 6, 22]. However, the specific interface responsible for E_b remains a subject of debate.

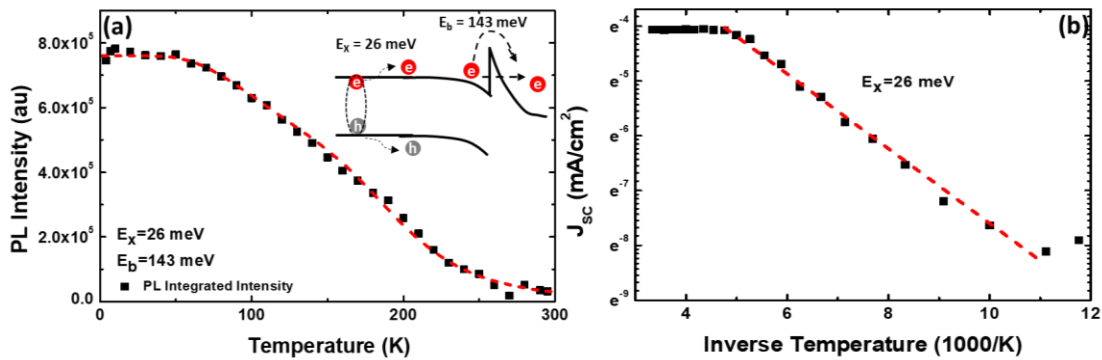


Figure 10. (a) The temperature dependence of the PL-integrated intensity is represented in an Arrhenius plot that fits two activation energies. The inset provides a visual representation of the impact and proportional contribution of carrier extraction, as well as the rate of radiative recombination caused by the potential barrier and exciton binding energies in these systems. (b) To determine the activation energy value of excitonic states, an Arrhenius plot of J_{sc} versus the inverse temperature ($1000/T$) is used.

Figure 10(b) provides further evidence of the correlation between carrier extraction and the role of exciton. Here, a plot of $\ln J_{sc}$ versus $1000/T$ for the perovskite solar cell shows that in the linear regime Follows an Arrhenius relationship given by:

$$\ln J_{sc} = \ln J_0 - \left(\frac{E_x}{k_B} * 1000 \right) \left(\frac{1000}{T} \right). \quad (2)$$

Here, the activation energy of the charge carriers that participate in conduction (E_x) can be calculated by equating the slope of the plot (shown in Figure 11(b)) with $(E_x/(k_B \times 1000))$, where k_B is the Boltzmann's constant, T is the temperature, and J_0 is the intrinsic current density of the device. This method yields an activation energy of $E_x \sim 26$ meV, which is consistent with the exciton binding energy extracted from the Arrhenius plot of the integrated intensity of the PL (shown in Figure 10(a)) further demonstrating the intimate relationship between the carrier extraction and PL spectrum. Indeed, this correlation between the quenching of the PL intensity and the increased J_{sc} confirms that the change in PL energy observed at ~ 170 K originates from the transition from excitonic to band-to-band like recombination. Moreover, despite the inhibited electronic performance at low temperatures, the perovskite solar cells assessed here are shown to operate predominantly in the radiative limit at all temperatures despite parasitic recombination in these structures in these regimes.

4.6 Conclusions

This chapter focused on the optoelectronic properties of triple cation perovskite $[\text{Cs}_{0.05}\text{FA}_{0.79}\text{MA}_{0.16}\text{Pb}(\text{I}_{0.83}\text{Br}_{0.17})_3]$ solar cells and analyzed their performance at low and high temperatures. The investigation revealed that at low temperatures ($T < 200$ K), a parasitic barrier to carrier extraction results in a loss of photovoltaic performance. Intensity-dependent measurements showed that the combination of the exciton binding energy and inefficient thermionic emission limit charge carrier extraction across a parasitic interface within the structure with the PV parameters recovering at low intensity levels. A correlation was observed between the loss of solar cell performance and an increase in PL intensity, indicating inhibited carrier extraction leads to strong radiative recombination. The study also revealed carrier extraction is inhibited by excitonic effects particularly at low temperatures, as evidenced by a strong anti-correlation in (high intensity and narrow) PL and (low) carrier extraction at lower temperatures. The study showed the presence of excitonic absorption in low-temperature EQE and the thermal quenching of this complex, indicating excitonic binding energies of ~ 26 meV.

4.7 References

- [1] M. Baranowski, P. Plochocka, Excitons in metal-halide perovskites, *Adv. Energy Mater.*, 10 (2020) 1903659. <https://doi.org/10.1002/aenm.201903659>
- [2] F. Ruf, A. Magin, M. Schultes, E. Ahlswede, H. Kalt, M. Hetterich, Excitonic nature of optical transitions in electroabsorption spectra of perovskite solar cells, *Applied Physics Letters*, 112 (2018) 083902.

- [3] J. Even, L. Pedesseau, C. Katan, Analysis of multivalley and multibandgap absorption and enhancement of free carriers related to exciton screening in hybrid perovskites, *J. Phys. Chem. C*, 118 (2014) 11566-11572. <https://doi.org/10.1021/jp503337a>
- [4] F. Panzer, C. Li, T. Meier, A. Köhler, S. Huettner, Impact of structural dynamics on the optical properties of methylammonium lead iodide perovskites, *Adv. Energy Mater.*, 7 (2017) 1700286. <https://doi.org/10.1002/aenm.201700286>
- [5] M. Wang, W.L. Yim, P. Liao, Y. Shen, Temperature dependent characteristics of perovskite solar cells, *ChemistrySelect*, 2 (2017) 4469-4477.
- [6] C. Brown, G. Eperon, V. Whiteside, I. Sellers, Potential of high-stability perovskite solar cells for low-intensity–low-temperature (LILT) outer planetary space missions, *ACS Appl. Energy Mater.*, 2 (2018) 814-821. <http://dx.doi.org/10.1021/acsaem.8b01882>
- [7] H. Zhang, X. Qiao, Y. Shen, T. Moehl, S.M. Zakeeruddin, M. Grätzel, M. Wang, Photovoltaic behaviour of lead methylammonium triiodide perovskite solar cells down to 80 K, *Journal of Materials Chemistry A*, 3 (2015) 11762-11767.
- [8] R.T. Ginting, E.-S. Jung, M.-K. Jeon, W.-Y. Jin, M. Song, J.-W. Kang, Low-temperature operation of perovskite solar cells: With efficiency improvement and hysteresis-less, *Nano Energy*, 27 (2016) 569-576.
- [9] Y. Chen, S. Tan, N. Li, B. Huang, X. Niu, L. Li, M. Sun, Y. Zhang, X. Zhang, C. Zhu, Self-elimination of intrinsic defects improves the low-temperature performance of perovskite photovoltaics, *Joule*, 4 (2020) 1961-1976.

- [10] I. Mesquita, L. Andrade, A. Mendes, Temperature impact on perovskite solar cells under operation, *ChemSusChem*, 12 (2019) 2186-2194.
- [11] S. Kanaya, G.M. Kim, M. Ikegami, T. Miyasaka, K. Suzuki, Y. Miyazawa, H. Toyota, K. Osonoe, T. Yamamoto, K. Hirose, Proton irradiation tolerance of high-efficiency perovskite absorbers for space applications, *J. Phys. Chem. Lett.*, 10 (2019) 6990-6995. <https://doi.org/10.1021/acs.jpcllett.9b02665>
- [12] Y. Miyazawa, M. Ikegami, H.-W. Chen, T. Ohshima, M. Imaizumi, K. Hirose, T. Miyasaka, Tolerance of Perovskite Solar Cell to High-Energy Particle Irradiations in Space Environment, *iScience*, 2 (2018) 148-155. <https://doi.org/10.1016/j.isci.2018.03.020>
- [13] A.R. Kirmani, B.K. Durant, J. Grandidier, N.M. Haegel, M.D. Kelzenberg, Y.M. Lao, M.D. McGehee, L. McMillon-Brown, D.P. Ostrowski, T.J. Peshek, Countdown to perovskite space launch: Guidelines to performing relevant radiation-hardness experiments, *Joule*, (2022).
- [14] F. Lang, N.H. Nickel, J. Bundesmann, S. Seidel, A. Denker, S. Albrecht, V.V. Brus, J. Rappich, B. Rech, G. Landi, Radiation Hardness and Self-Healing of Perovskite Solar Cells, *Adv. Mater.*, 28 (2016) 8726-8731. <https://doi.org/10.1002/adma.201603326>
- [15] N.H. Nickel, F. Lang, V. Brus, J. Bundesmann, S. Seidel, A. Denker, S. Albrecht, G. Landi, H. Neitzert, Radiation hardness and self-healing of perovskite solar cells under proton irradiation (Conference Presentation), in: *Physics, Simulation, and Photonic Engineering of Photovoltaic Devices VII*, SPIE, 2018, pp. 1052703.
- [16] Y. Tu, J. Wu, G. Xu, X. Yang, R. Cai, Q. Gong, R. Zhu, W. Huang, Perovskite Solar Cells for Space Applications: Progress and Challenges, *Advanced Materials*, 33 (2021) 2006545. <https://doi.org/10.1002/adma.202006545>

- [17] G. Mannino, I. Deretzis, E. Smecca, A. La Magna, A. Alberti, D. Ceratti, D. Cahen, Temperature-dependent optical band gap in CsPbBr₃, MAPbBr₃, and FAPbBr₃ single crystals, *The journal of physical chemistry letters*, 11 (2020) 2490-2496.
- [18] L. Lin, N. Ravindra, Temperature dependence of CIGS and perovskite solar cell performance: an overview, *SN Appl. Sci.*, 2 (2020) 1-12. <https://doi.org/10.1007/s42452-020-3169-2>
- [19] Y. Guo, O. Yaffe, T.D. Hull, J.S. Owen, D.R. Reichman, L.E. Brus, Dynamic emission Stokes shift and liquid-like dielectric solvation of band edge carriers in lead-halide perovskites, *Nat. Commun.*, 10 (2019) 1-8. <https://doi.org/10.1038/s41467-019-09057-5>
- [20] B.K. Durant, H. Afshari, S. Sourabh, V. Yeddu, M.T. Bamidele, S. Singh, B. Rout, G.E. Eperon, I.R. Sellers, Radiation stability of mixed tin–lead halide perovskites: Implications for space applications, *Sol. Energy Mater. Sol. Cells*, 230 (2021) 111232. <https://doi.org/10.1016/j.solmat.2021.111232>
- [21] S. Sourabh, V. Whiteside, I. Sellers, Y. Zhai, K. Wang, M.C. Beard, V. Yeddu, M. Bamidele, D. Kim, Hot carrier redistribution, electron-phonon interaction, and their role in carrier relaxation in thin film metal-halide perovskites, *Phys. Rev. Mater.*, 5 (2021) 095402. <https://doi.org/10.1103/PhysRevMaterials.5.095402>
- [22] H. Afshari, B.K. Durant, A.R. Kirmani, S.A. Chacon, J. Mahoney, V.R. Whiteside, R.A. Scheidt, M.C. Beard, J.M. Luther, I.R. Sellers, Temperature-Dependent Carrier Extraction and the Effects of Excitons on Emission and Photovoltaic Performance in Cs_{0.05}FA_{0.79}MA_{0.16}Pb_{0.83}Br_{0.17} 3 Solar Cells, *ACS Applied Materials & Interfaces*, 14 (2022) 44358-44366.

Chapter 5

High Temperature Stability of FACsPb(IBrCl)₃ Perovskite Solar Cells

Metal halide perovskites have gained significant attention as a cost-effective photovoltaic (PV) technology for terrestrial applications. In addition, perovskite PVs possess distinct properties that could make them a promising option for space PV technology due to their ability to withstand high levels of radiation [1, 2]. However, surviving in space requires more than radiation tolerance, as exposure to high temperatures is also a major risk factor. Satellites orbiting in low Earth orbits frequently encounter temperatures as high as 120 °C (393-413 K), making it crucial to evaluate the thermal stability of perovskite solar cells (PSCs) despite their radiation tolerance. Specific mechanisms related to perovskite materials, such as ion migration, phase segregation, and the outgassing of organic molecules, raise concerns about their thermal stability [3]. Therefore, it is necessary to investigate and enhance their thermal response at high temperatures (> 358 K or 85 °C) to facilitate practical space applications [3, 4]. Additionally, accelerated lifetime testing and stability assessment of perovskites is essential for their use in terrestrial applications.

Perovskite solar cells based on the triple halide and formamidinium cesium (FACs) configuration have exhibited exceptional stability, outperforming other perovskite systems [5-8]. Although single gap PV applications have been extensively studied, the triple halide systems have displayed great potential and suitability as the high energy junction in perovskite-perovskite [9, 10], silicon-perovskite [11, 12], and CIGS-perovskite [13, 14] tandem solar cells. Earlier investigations have also demonstrated that the metal halide perovskite systems exhibit high

radiation tolerance, which makes them attractive for space power applications [3, 15, 16]. This study presents high-temperature data that systematically and statistically establishes the high thermal stability of this system, even at temperatures exceeding 200 °C.

5.1 Solar Cell Design for High Temperature Tolerance

This study demonstrates the remarkable high temperature performance of triple halide perovskite solar cells based on FACs cation configurations. The excellent thermal stability of these cells is attributed to their unique design, which also includes a triple-halide architecture. Firstly, the use of double cation (FACs) composition enhances stability [17, 18] Secondly, the transparent conductive back contact prevents metal-induced degradation that may occur through metal migration or iodine-metal corrosion [19]. Finally, the conformal atomic layer deposition (ALD) of an alumina-based nanolaminate helps prevent thermal decomposition. The bifacial cell design utilized for applications in tandem structures allows independent assessment of transparent front and back surfaces *optically*. The PV performance of the solar cell is evaluated at temperatures ranging from – 23 °C to 217 °C (250 K to 490 K).

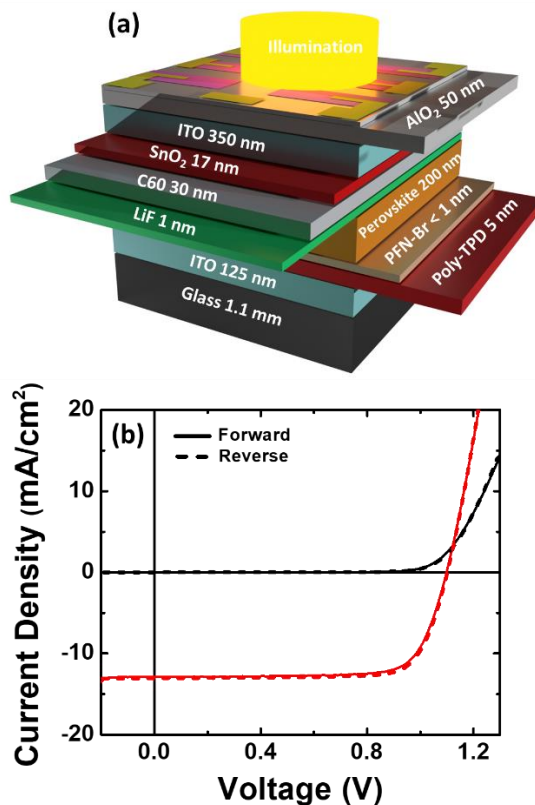


Figure 1(a). Schematic of perovskite solar cell investigated in this study. Here, the upper and lower transparent contacts encapsulate the absorber layer, which is thinner than typical structures to facilitate assessment of the thin film optically, as well as the device response (b) Representative dark (black) and light (red) J-V curves at 1-Sun AM1.5G in ambient conditions.

Figure 1(a) illustrates the structural design of the solar cell with triple halide perovskite material as the absorber layer. The perovskite layer, which has a band gap of approximately 1.7 eV and a thickness of 200 nm, is deposited using a spin-coating technique onto an indium tin oxide (ITO) front contact. A poly(N,N'-bis-4-butylphenyl-N,N'-bisphenyl)benzidine (Poly-TPD) layer is used as the hole transport layer, while a poly[(9,9-bis(3'-((N,N-dimethyl)-N-ethylammonium)-propyl)-2,7-fluorene)-alt-2,7-(9,9-dioctylfluorene)]dibromide (PFN-Br) interface layer is used to enhance the perovskite crystal formation. To evaluate absorption, the absorber layer thickness is kept lower than that of typical perovskite solar cells. The thermal stability of the perovskite layer

is also assessed in devices with a more conventional 400 nm perovskite layer to exclude device stack degradation which is discussed in the next sections.

Figure 1(b) displays the J-V responses of the devices, which were evaluated in both dark conditions and under 1-Sun AM1.5G illumination. The absence of hysteresis, as well as the high yield and reproducibility of approximately 100 solar cells, validate the quality of these devices. These solar cells belong to three generations of devices that were fabricated independently within an 18-month period, as illustrated in Figure 2.

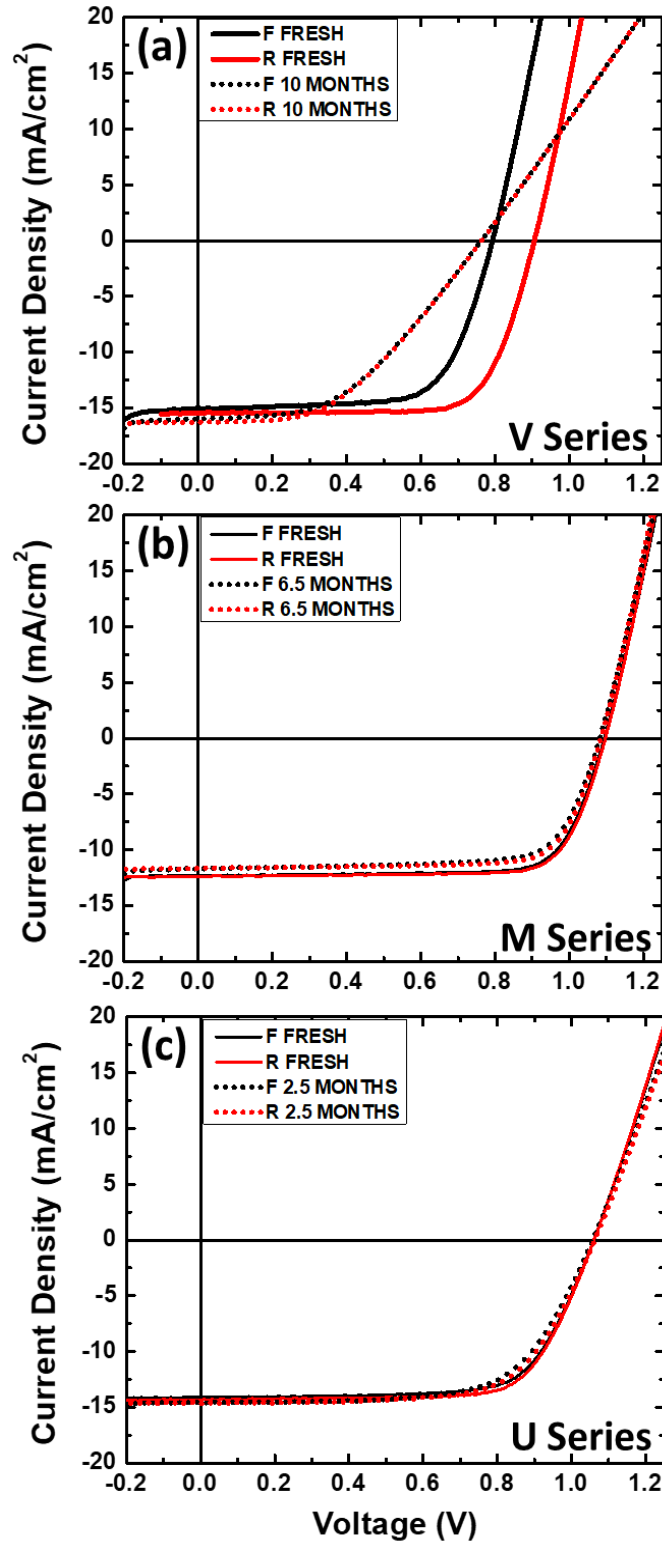


Figure 2. J-V data from three batches of the solar cells: (a) V series; (b) M series; and (c) U series studied for over 18 months. The data presents J-V scans in both forward and reverse direction (positive to

negative bias, negative to positive bias) and after long periods of time where the samples were exposed to different stresses such as high temperature exposure or high energy proton irradiation. *F* stands for forward and *R* stands for reverse. The dotted lines show the results after a prolonged time of 10 months for series V shown in (a), 6.5 months for series M shown in (b), and 2.5 months for series U shown in (c).

J-V characteristics of a range of devices at temperatures ranging from 250 K (-23 °C) to 490 K (217 °C) in increments of 10 K were assessed in the cryostat maintaining a vacuum of approximately 10^{-3} Torr. These measurements allow the space vacuum and cycling to be somewhat assessed in the laboratory. At each temperature point, both forward and reverse biased J-V measurements were taken for both 1-Sun AM1.5G and dark conditions, with the devices being held at each temperature for approximately 5 minutes between each scan once each at the temperature set.

Figure 3. shows the temperature dependent J-V measurements taken using both reverse (solid) and forward (dashed) voltage sweeps up to 490 K (217 °C). Evidence of hysteresis, indicating non-idealities such ion migration-halide and charging and discharging of interfaces and segregation are evident particularly at higher temperatures, as reflected as a loss of V_{OC} especially above 400 K (Figure 3). However, despite these high temperature effects, the devices do not experience prohibitive degradation. Upon returning to ambient temperatures, they retain and reproduce their original performance, and in some cases, there is even a slight improvement after this high temperature exposure.

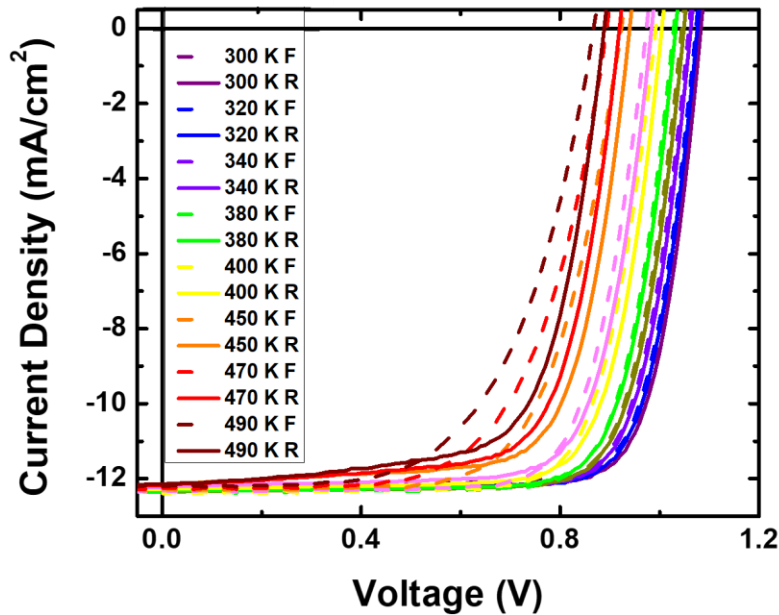


Figure 3. Temperature dependent J-V measurements for the FACsPb(IBrCl)₃ solar cell under study swept from forward (F – dashed) to reverse bias, and reverse (R - solid) to forward bias direction from 300 K up to 490 K.

5.2 High Temperature Effects Upon Photovoltaic Performance

In Figure 4, the temperature dependence of the key photovoltaic parameters are presented. These data were extracted from reverse to forward biased sept J-V measurements, which are shown in the inset to Figure 4. The J_{sc} is almost constant throughout the temperature range studied, which indicates the system is extremely efficient in extracting carriers even at temperatures as high as 490 K. The fill factor (FF), represented by gray symbols, demonstrates the tolerance of these perovskite solar cells to extremely high temperatures, with FF retention of approximately 90% of its initial value up 490 K (217 °C). It is worth noting that the FF of a perovskite solar cell is typically sensitive to external perturbations and reflects resistance to carrier extraction and degradation in the absorber, at interfaces, or in transporting regions. The stability shown in Figure 4 for the FF - in this case - suggests that extreme high temperatures do not significantly

affect the structural properties of the junction(s) and the device structure for the $\text{FACsPb}(\text{IBrCl})_3$ system studied. This indicates that the absorber material and interfaces are relatively stable even at high temperatures. On the other hand, the open-circuit voltage (V_{OC}), represented by red triangles in Figure 4, is the photovoltaic (PV) parameter most affected by increased temperature exposure above 200 °C. However, it still retains 80% of its initial value. This indicates some increase in defect formation likely halide segregation at elevated temperatures [20, 21] The combined effects of the PV parameters at high temperature result in a loss of power conversion efficiency (PCE), which retains 70% of its initial ambient value at 490 K (217 °C).

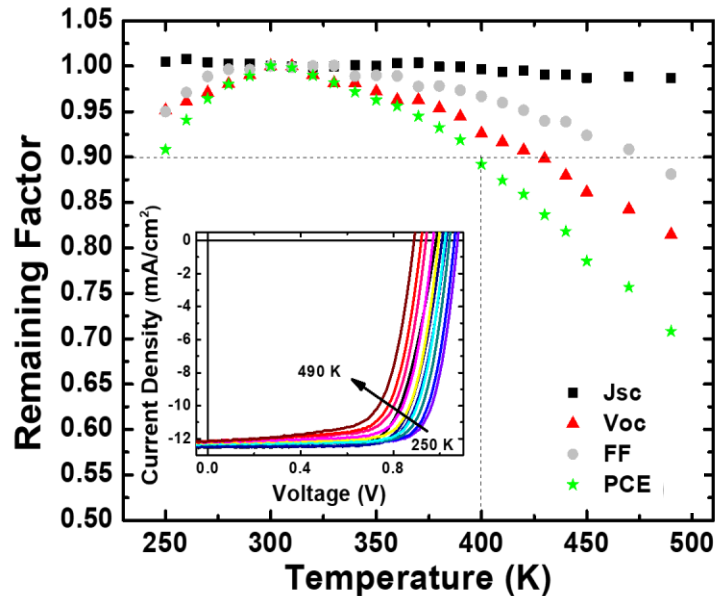


Figure 4. Temperature dependence of the remaining factors for PV parameters: J_{sc} , V_{oc} , FF, and PCE extracted from the J-V curves shown in the inset. The inset shows temperature dependent J-V results swept in the reverse direction from 300 K to 490 K.

The exposure to high temperatures for conventional solar cells typically leads to reduction in band gap translating in a decrease of V_{oc} due to increased intrinsic carrier density [22, 23]. However, perovskite systems exhibit an increase in band gap with rising temperatures, (as shown

in Figure 9). Consequently, the origin of V_{OC} loss in perovskite solar cells at higher temperatures is more nuanced than in traditional semiconductor solar cells such as silicon or the III-Vs. This is consistent with the constant J_{sc} (black squares) observed at elevated temperatures in Figure 4, which would be affected if the dark current increased over this temperature range – which would be expected if the change in V_{OC} were defect mediated as is often the case. Although further investigation is needed to fully understand the V_{OC} loss observed at higher temperatures in this study (Figure 4), it is likely caused by reversible halide segregation at elevated temperatures, and under illumination. This segregation results in iodine-rich regions in the absorber and a reduction in the band gap. [24, 25].

5.3 Effects of High Temperature on the Radiative Emission

In addition to the apparent stability of the FACsPb(I₂BrCl)₃ solar cells studied here to *extreme* temperatures ($T > 215$ °C) previous work has also demonstrated the absence of prohibitive degradation of the solar cells after exposure to *very* high excitation powers (> 0.5 W) in photoluminescence experiments [26]. These works together [26, 27] indicate that while the perovskite absorber is affected by these perturbations in the form of halide segregation and possibly a structural phase transition [27, 28], these characteristics are not deleterious to the performance of the solar cell systems studied and that they are reversible due to the soft nature of the perovskites, in general, and due to the dynamics of their constituent elements at high temperatures and/or under high energy photoactivation [27, 28]. Figure 5 shows the power dependent PL from the FACsPb(I₂BrCl)₃ absorber and provides further evidence of this lack of degradation in these systems. Under high photoexcitation (~ 500 mW, or 8.2 W/cm²), lattice and carrier distribution heating occur, which in combination with the energy introduction to the system by photoexcitation result in the onset of halide segregation, with a local lattice

temperature exceeding 450 K. However, the lattice returns to its original PL energy/linewidth at low power and after the measurements have been completed demonstrating the reversible nature of alloy decomposition in these materials.

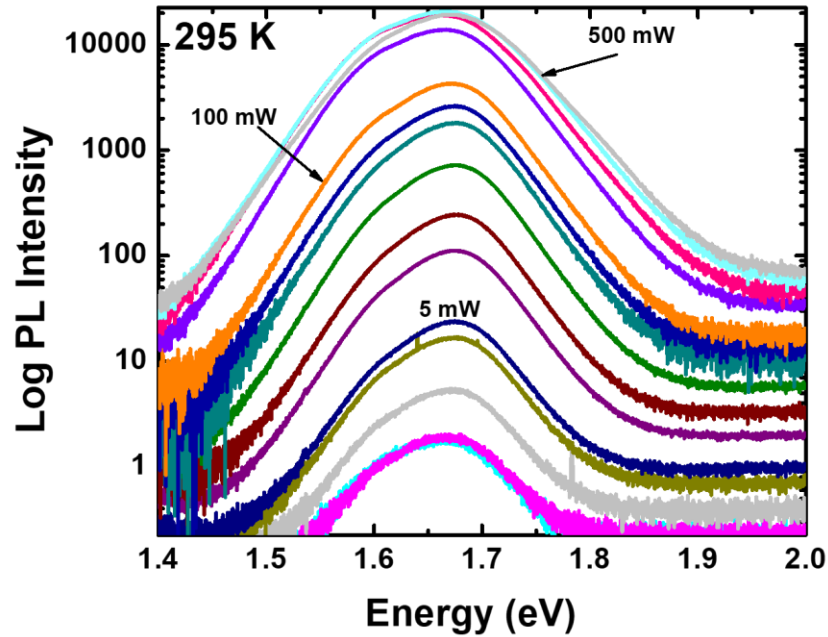


Figure 5. Power dependent photoluminescence (PL) at 295 K between 0.5 mW (8.2 mW/cm^2) to 500 mW (8.2 W/cm^2). These data are plotted on a logarithmic scale for clarity of the low power data.

Figure 5 presents the power dependent photoluminescence of the absorber region of the solar cell at excitation powers ranging from 0.5 mW (8.2 mW/cm^2) to 500 mW (8.2 W/cm^2). As seen in Figure 5, while the magnitude increases as expected, the shape of the emission spectrum is retained as power is increased. Furthermore, there is negligible shift in the main emission peak (at 1.67 eV), which indicates that the material is tolerant to the high laser powers used. Also, there is a low energy shoulder next to the main peak that can be due to the domains of the segregated elements which will get pronounced at very high powers.

5.4 Improved Performance at High Temperature: Effect of Local Heating

The apparent ability of the solar cells studied here to return to their original performance after thermal cycling demonstrates their robust and reversible nature. As shown in Figure 6 (a), the J-V measurements at 1-Sun AM1.5G at 300 K before and after exposure to high temperature stress reveal that the devices retain much of their performance. These data – coupled with the PL exposed to high powers - highlight the lack of prohibitive degradation and the reversible nature of the devices under high thermal stress. The primary section in Figure 6 illustrates the remaining factor of the key PV parameters obtained from the 1-Sun AM1.5G J-V measurements conducted at 300 K, following the exposure of solar cells to temperatures reaching up to 490 K. These outcomes represent data from various pixels on the device, with the error bars representing the distribution of results across all assessed pixels and devices, supporting the universal nature of the stability observed for these devices.

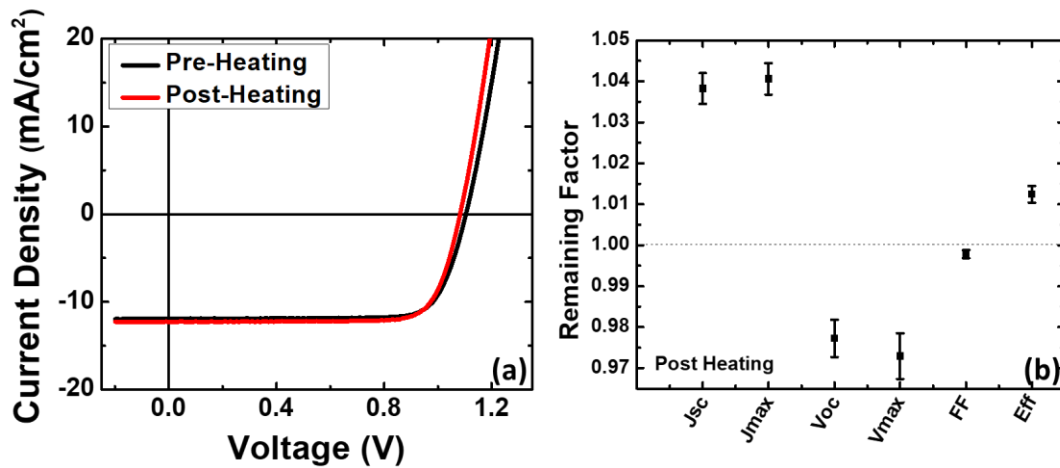


Figure 6. The inset shows the J-V curve for 300 K under 1-Sun AM1.5G measured before (black) and after (red) thermal cycle demonstrating retention of performance despite the extreme thermal load under which they were exposed. The main panel is a plot of the remaining factors for room temperature PV parameters post heating.

According to Figure 6, the thermal stress did not degrade J_{sc} or the maximum photocurrent, J_{max} ; rather, they actually improved by approximately 4% after exposure to high temperatures. This improvement is attributed to annealing, which likely enhances the quality of the interfaces, transporting layers, and/or absorbers in the solar cell structure. While V_{OC} and the maximum photovoltage, V_{max} did experience some degradation (as shown in Figure 6), this decrease was relatively small at $\sim 3\%$ absolute. This small change is attributed to slight changes in the perovskite lattice resulting from annealing, the low crystallization temperature of the systems, or other effects like material homogenization and strain relaxation induced by annealing of the system. The FF is almost not affected (-0.2%) after the high temperature exposure. The combined effect of change in the PV parameters due to thermal stress caused 1% *increase* in the power conversion efficiency (PCE).

These devices clearly exhibit considerable stability and resilience to external perturbations and are not subject to a meaningful degradation upon exposure to high temperatures. This is further demonstrated by analyzing the dark J-V of the solar cells before high temperature exposure at 490 K and after thermal cycling, as shown in Figure 7. This data indicates that not only does the dark J-V not increase after exposure to high temperatures, it (once again) experiences a decrease in the absolute current level after thermal stress. This supports the absence of increased non-radiative channels upon thermal stress *and* that the system is improved due to the annealing effects to which the structure is exposed during cycling.

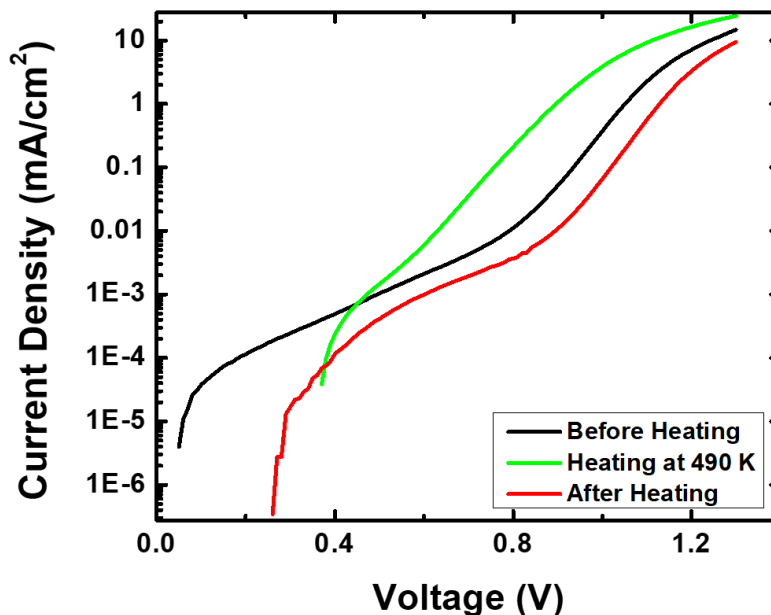


Figure 7. Dark J-V plots of a representative FACsPb(IBrCl)₃ solar cell before heating (black), at 490 K (green), and after exposure to high temperature heating (red).

5.5 Dependence of Absorber Thickness to High Temperature Stress

While high thermal stability has been demonstrated as discussed above, question remain regarding the assessment of such effects in relatively thin (200 nm) absorber layers, which were utilized in this study to enable assessment of both the device characteristics *and* the optical properties of the perovskite absorber. Since the absorber is ~ half as thick as typical perovskite layers (of the order of 400 nm) it is possible that stability of the (for example) J_{sc} recorded under high temperature exposure may not be significantly affected in these specific samples due to the low distance the carriers are required to travel for collection in the test structures with a thin absorber layer (200 nm). That is, that this short path length may be sufficient for effective collection independent of defect generation, and compensate for any decrease in diffusion length due to defects and decomposition at high temperatures, as is seen in ultrathin III-V solar cells exposed to high-energy irradiation [29]. However, it is important to note that the stability and

performance of these systems at 490 K is also observed in all structures, even those assessed with a conventional absorber thickness of 400 nm. This is shown in Figure 8, which presents the high temperature J-V results of the perovskite solar cell with 400 nm absorber layer indicating almost constant J_{SC} up to 490 K. Therefore, the observed stability cannot be solely attributed to the thinness of the absorber layer in this study.

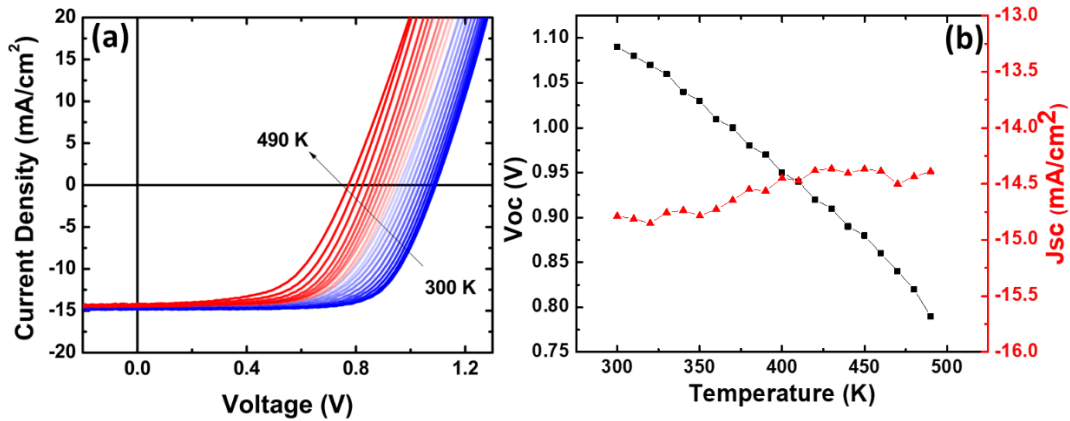


Figure 8. (a) Temperature dependent J-V from 300 K up to 490 K for an alternative optimized FACsPb(IBrCl)₃ perovskite solar cell with a more conventional 400 nm absorber layer. (b) V_{OC} and J_{SC} versus temperature extracted from (a).

It is seen (Figure 8) that for the thick absorber layer samples the J_{sc} is still the most tolerant PV parameter. The atypical J_{sc} can be explained by considering the impact of temperature on band gap renormalization and collection efficiency.

Figure 9 presents the temperature dependent EQE data for 200 nm absorber cell, which can provide additional insight into dynamics of carrier extraction in the system. By extracting J_{sc} values from the EQE data at room and high temperatures, a value of approximately 12 mA/cm² is obtained, which is consistent with the J_{sc} measured in Figure 4 under the solar simulator. The low absolute EQE at longer wavelengths (450 nm - 700 nm) reflects the non-optimal thickness of

the absorber used in this study that limits the absorption in the film resulting consequently in a reduction in the absolute EQE. Notably, Figure 9 does not show any evidence of a structural phase transition shift, which result in a significant and abrupt redshift of the band gap at $T \sim 160$ K, [30] instead of the observed thermally mediated blueshift in the EQE edge as the bandgap increases at elevated temperatures. This behavior further supports the idea that the decrease in V_{oc} or performance at higher temperatures is due to halide segregation and ion migration as iodine inclusion reduce the bandgap, rather than defect states increasing the dark current.

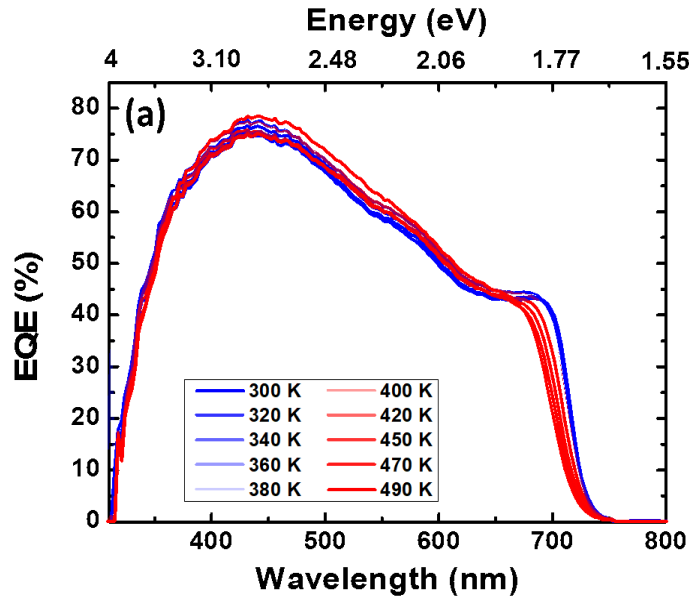


Figure 9. Temperature dependent external quantum efficiency for $\text{FACsPb}(\text{IBrCl})_3$ between 300 K and 490 K showing expected increase in the perovskite band gap as a function of temperature.

5.6 J-V Experiments Under More Practical Conditions

When performing J-V measurements for the evaluation of the thermal stability at high temperatures, the data at each temperature were recorded once the target temperature was reached and the solar cell was held in the dark until these conditions were met. While this approach enables qualitative trends and performance of the devices to be considered this

approach does not reflect the practical conditions that would be experienced by a solar cell on orbit in space, where the temperature would increase rapidly during full illumination. Therefore, to create more practical conditions for assessment the solar cells were tested under conditions in which the temperature was increased during full illumination, and the data recorded. These data are shown in Figure 10 for measurements in which the samples were held at (a) J_{sc} and (b) V_{oc} between temperatures/scans. Despite the constant exposure, the devices performed well under constant illumination at 1-Sun AM 1.5G at temperatures ranging from 300 K to 490 K under both conditions (J_{sc} and V_{oc}). This behavior was seen in both samples with thinner absorber regions, as well as those with thicker active regions, which are those show here in Figure 10. As such, these FACsPb(IBrCl)₃ solar cells once again produced exceptional tolerance to the thermal stress and importantly residual charge that is generated and held in the solar cell under V_{oc} was not observed to cause significant degradation, which has been a problem historically in the metal halide perovskites [31, 32], demonstrating further the structural stability and interfacial purity of these specific systems.

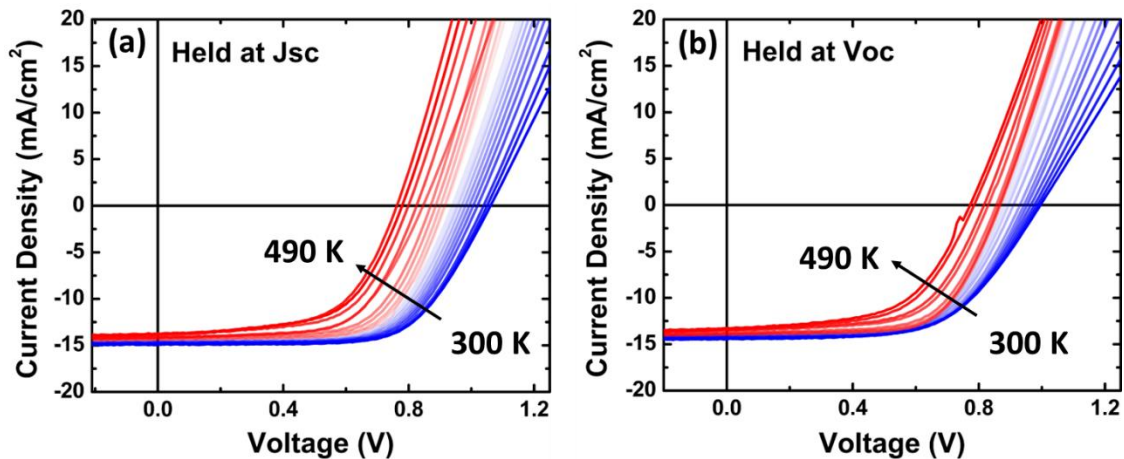


Figure 10. Temperature dependent J-V from 300 K to 490 K under constant illumination at 1-Sun AM 1.5G when (a) holding the cell at J_{sc} between scans, and (b) holding the devices at V_{oc} between temperature scans.

Previous studies have demonstrated that the perovskite materials (films) have the potential to withstand high temperatures [33, 34], although they also indicate that the organic components (FA) in the perovskite can segregate at ~ 473 K (200 °C) under very high temperature conditions [21, 33-35]. These previous studies have mainly focused on the perovskite film or absorber rather than full solar cell structures. Moreover, those few previous assessments of perovskite solar cell technologies that have been performed at higher temperature consistently demonstrate the inability of the devices to function at temperatures in excess of 100 °C [36, 37]. Nonetheless, previous studies on “bulk perovskite materials” (not solar cells) do provide valuable information to the PV community, suggesting that tailored perovskite systems could withstand temperatures as high as 200 °C [21, 38]. While high temperature degradation mechanisms indicate a significant decline in device performance above 100 °C, the use of ultra-thin perovskite material layers, less than a micron in thick, sandwiched in tightly packed structures can alter the dynamics. Furthermore, the timescales of degradation in mixed cation-based systems at high temperatures have yet to be fully explored. Our study shows that the perovskite composition used here (FACsPb(IBrCl)₃) exhibits high temperature tolerance, particularly for J_{sc} , which remains relatively constant up to 490 K (217 °C). This can be attributed to the thermal and structural stability of the FACs-triple based metal halide perovskites [39], as well as the effectiveness of the on-cell encapsulation used to package the system here. It should be noted that while the temperatures assessed here exceed some other studies of perovskite solar cells (80 °C) [40], the observed robust performance is not unique to the perovskite absorber layer. Rather, it is a result of several factors, including the absence of spiro-OMeTAD, the use of ITO as the hole transporting layer, and the incorporation of an Al₂O₃-based encapsulation layer, which acts as a chemical barrier and prevents the loss of even FA at such high temperatures [33]. In fact,

less stable MAPbI₃ thin films have been shown to withstand high temperatures (~ 150 °C) when encapsulated in glass and laminated to prevent the loss of constituent materials, supporting the hypothesis related to stabilization due to encapsulation postulated here [41]. Indeed, recent works have shown that encapsulation has the capability to enhance the stabilization of perovskite devices, especially under high fluence alpha and proton irradiation, for devices that have been encapsulated with a silicon oxide layer [42]. These encapsulated devices exhibited significantly higher stability as compared to reference solar cells that were exposed to direct irradiation of the perovskite absorber without encapsulation. These studies suggest that by preventing the constituent elements of perovskites from escaping, the inherent dynamic nature of these systems enables self-healing and inhibits detrimental decomposition [1, 42].

5.7 Assessment of the Temperature Coefficients in Perovskite Solar Cells

The PV parameters in perovskite solar cells exhibit a remarkable temperature dependence, resulting in temperature coefficients for maximum power (TPCE) as low as -0.08 % °C⁻¹ (see Figure 11) and as observed by others [40]. This surpasses the TPCE values of conventional commercial solar cell technologies such as silicon, CdTe, GaAs, and CIGS [40]. The temperature coefficient of a solar cell is the amount by which its output power changes due to a change in the ambient temperature. It is an industrially important parameter deciding which technologies of the solar panels are suitable for which environments based on the temperature. GaAs solar cell for example has very low temperature coefficient meaning its PCE drop at high temperatures (70 °C) is very small and hence is suitable for space applications in orbits which experience such high temperatures. This low temperature coefficient demonstrated in these systems is further indication that perovskite solar cells display promising performance characteristics over a wide temperature range.

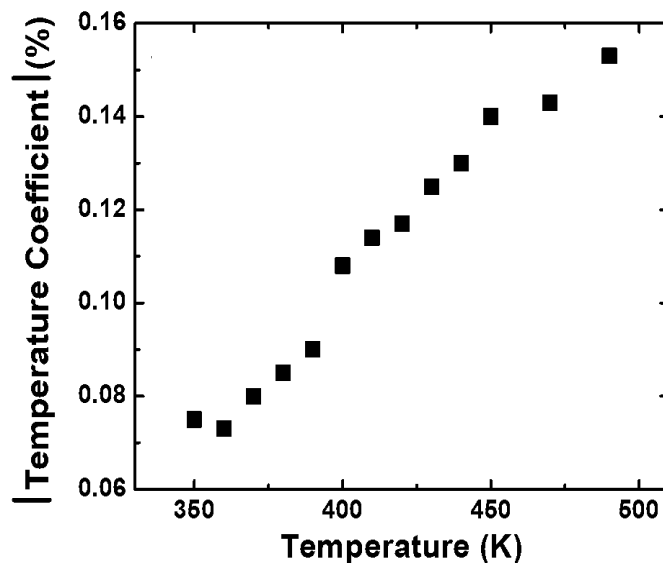


Figure 11. Temperature dependence of the temperature coefficient between 350 K and 490 K.

Although the temperature coefficient is usually determined relative to the industry standard [40] of 25 °C because there is a greater decrease in efficiency at higher temperatures the upper temperature limit has a more significant effect on the temperature coefficient. As a result, the magnitude of the temperature coefficient increases as the temperature rises, as seen in Figure 11 for the $\text{FACsPb}(\text{IBrCl})_3$ perovskite solar cell assessed here. Here, the temperature coefficient was found to scale from $-0.08\% \text{ } ^\circ\text{C}^{-1}$ to $-0.15\% \text{ } ^\circ\text{C}^{-1}$ over a temperature range of 75 °C to 217 °C. This is a favorable result when compared to previous analyses in perovskites and other solar cell technologies see Table 1, despite the evaluation being conducted at a high temperature of 490 K (217 °C) [40].

Solar Cell	Highest Temperature	Temperature Coefficient
Si	75 °C	- 0.258 % / °C
CdTe	75 °C	- 0.28 % / °C
CIGS	75 °C	- 0.38 % / °C
GaAs	60 °C	- 0.08 % / °C
Perovskites (NiOx/triple cation)	80 °C	- 0.12 % / °C
Perovskites (NiOx/triple cation) Champion Cell	80 °C	- 0.08 % / °C
Perovskite (Triple halide)	97 °C	- 0.08 % / °C
Perovskite (Triple halide)	117 °C	- 0.09 % / °C
Perovskite (Triple halide)	217 °C	- 0.15 % / °C

Table I. presenting temperature coefficient of various solar cell technologies. The temperature coefficient of the triple halide perovskite solar cell at three temperatures is also included to compare with other technologies [40].

5.8 Conclusions

Here, solar cells based on the triple halide perovskite FACsPb(I₂BrCl)₃ were exposed to extreme thermal stress ranging from – 23 °C to 217 °C. Despite the high temperature exposure, and some evidence of segregation, for the devices studied any losses observed at higher temperatures were reversible and the devices recovered and maintained their performance when returned to ambient conditions. This is attributed to the use of this highly stable perovskite, FACsPb(I₂BrCl)₃, within a architecture that incorporated a transparent conductive back contact, and nanolaminate encapsulation. These innovations in fabrication and packaging resulted in solar cells that retained

over 90% of their initial power conversion efficiency even at 400 K (127 °C). The high temperature tolerance was verified via a suite of complementary measurements including temperature dependent light and dark J-V measurements, EQE, high power photoluminescence, and subsequently an experimental assessment of the temperature coefficient, which is a measure of performance of the solar cells in response to varied temperature changes and was shown to be very high compared to more traditional systems in the case of the metal halide systems assessed here.

5.9 References

- [1] A.R. Kirmani, B.K. Durant, J. Grandidier, N.M. Haegel, M.D. Kelzenberg, Y.M. Lao, M.D. McGehee, L. McMillon-Brown, D.P. Ostrowski, T.J. Peshek, Countdown to perovskite space launch: Guidelines to performing relevant radiation-hardness experiments, *Joule*, (2022).
- [2] A.W. Ho-Baillie, H.G. Sullivan, T.A. Bannerman, H.P. Talathi, J. Bing, S. Tang, A. Xu, D. Bhattacharyya, I.H. Cairns, D.R. McKenzie, Deployment opportunities for space photovoltaics and the prospects for perovskite solar cells, *Advanced Materials Technologies*, 7 (2022) 2101059.
- [3] Y. Miyazawa, M. Ikegami, H.-W. Chen, T. Ohshima, M. Imaizumi, K. Hirose, T. Miyasaka, Tolerance of Perovskite Solar Cell to High-Energy Particle Irradiations in Space Environment, *iScience*, 2 (2018) 148-155. <https://doi.org/10.1016/j.isci.2018.03.020>
- [4] L.E. Mundt, F. Zhang, A.F. Palmstrom, J. Xu, R. Tirawat, L.L. Kelly, K.H. Stone, K. Zhu, J.J. Berry, M.F. Toney, Mixing Matters: Nanoscale Heterogeneity and Stability in Metal Halide Perovskite Solar Cells, *ACS Energy Letters*, 7 (2021) 471-480.

- [5] I.M. Pavlovec, M.C. Brennan, S. Draguta, A. Ruth, T. Moot, J.A. Christians, K. Aleshire, S.P. Harvey, S. Toso, S.U. Nanayakkara, Suppressing cation migration in triple-cation lead halide perovskites, *ACS Energy Letters*, 5 (2020) 2802-2810.
- [6] X. Wu, Y. Jiang, C. Chen, J. Guo, X. Kong, Y. Feng, S. Wu, X. Gao, X. Lu, Q. Wang, Stable triple cation perovskite precursor for highly efficient perovskite solar cells enabled by interaction with 18C6 stabilizer, *Advanced Functional Materials*, 30 (2020) 1908613.
- [7] J. Xu, C.C. Boyd, Z.J. Yu, A.F. Palmstrom, D.J. Witter, B.W. Larson, R.M. France, J. Werner, S.P. Harvey, E.J. Wolf, Triple-halide wide-band gap perovskites with suppressed phase segregation for efficient tandems, *Science*, 367 (2020) 1097-1104.
- [8] K. Xu, A. Al-Ashouri, Z.-W. Peng, E. Köhnen, H. Hempel, F. Akhundova, J.A. Marquez, P. Tockhorn, O. Shargaieva, F. Ruske, Slot-Die Coated Triple-Halide Perovskites for Efficient and Scalable Perovskite/Silicon Tandem Solar Cells, *ACS Energy Letters*, 7 (2022) 3600-3611.
- [9] R. Lin, J. Xu, M. Wei, Y. Wang, Z. Qin, Z. Liu, J. Wu, K. Xiao, B. Chen, S.M. Park, All-perovskite tandem solar cells with improved grain surface passivation, *Nature*, 603 (2022) 73-78.
- [10] J.H. Heo, S.H. Im, CH₃NH₃PbBr₃-CH₃NH₃PbI₃ Perovskite-Perovskite Tandem Solar Cells with Exceeding 2.2 V Open Circuit Voltage, *Advanced materials (Deerfield Beach, Fla.)*, 28 (2016) 5121-5125. 10.1002/adma.201501629
- [11] A. Al-Ashouri, E. Köhnen, B. Li, A. Magomedov, H. Hempel, P. Caprioglio, J.A. Márquez, A.B. Morales Vilches, E. Kasparavicius, J.A. Smith, N. Phung, D. Menzel, M. Grischek, L. Kegelmann, D. Skroblin, C. Gollwitzer, T. Malinauskas, M. Jošt, G. Matič, B. Rech, R. Schlatmann, M. Topič, L. Korte, A. Abate, B. Stannowski, D. Neher, M. Stolterfoht, T. Unold, V. Getautis, S. Albrecht, Monolithic perovskite/silicon tandem solar cell with >29% efficiency by enhanced hole extraction, *Science*, 370 (2020) 1300-1309. doi:10.1126/science.abd4016

- [12] J. Liu, M. De Bastiani, E. Aydin, G.T. Harrison, Y. Gao, R.R. Pradhan, M.K. Eswaran, M. Mandal, W. Yan, A. Seitkhan, M. Babics, A.S. Subbiah, E. Ugur, F. Xu, L. Xu, M. Wang, A.u. Rehman, A. Razzaq, J. Kang, R. Azmi, A.A. Said, F.H. Isikgor, T.G. Allen, D. Andrienko, U. Schwingenschlögl, F. Laquai, S. De Wolf, Efficient and stable perovskite-silicon tandem solar cells through contact displacement by MgFx, *Science*, 377 (2022) 302-306. doi:10.1126/science.abn8910
- [13] M. Jošt, E. Köhnen, A. Al-Ashouri, T. Bertram, Š. Tomšič, A. Magomedov, E. Kasparavicius, T. Kodalle, B. Lipovšek, V. Getautis, R. Schlatmann, C.A. Kaufmann, S. Albrecht, M. Topič, Perovskite/CIGS Tandem Solar Cells: From Certified 24.2% toward 30% and Beyond, *ACS Energy Letters*, 7 (2022) 1298-1307. 10.1021/acsenergylett.2c00274
- [14] Q. Han, Y.-T. Hsieh, L. Meng, J.-L. Wu, P. Sun, E.-P. Yao, S.-Y. Chang, S.-H. Bae, T. Kato, V. Bermudez, Y. Yang, High-performance perovskite/Cu(In,Ga)Se₂ monolithic tandem solar cells, *Science*, 361 (2018) 904-908. doi:10.1126/science.aat5055
- [15] H.A. B. K. Durant, S. Singh, B. Rout, G. E. Eperon and I. R. Sellers, Tolerance of Perovskite Solar Cells to Targeted Proton Irradiation and Electronic Ionization Induced Healing, *ACS Energy Lett.*, (2021). <https://doi.org/10.1021/acsenergylett.1c00756>
- [16] Y. Tu, J. Wu, G. Xu, X. Yang, R. Cai, Q. Gong, R. Zhu, W. Huang, Perovskite Solar Cells for Space Applications: Progress and Challenges, *Advanced Materials*, 33 (2021) 2006545. <https://doi.org/10.1002/adma.202006545>
- [17] G. Niu, W. Li, J. Li, X. Liang, L. Wang, Enhancement of thermal stability for perovskite solar cells through cesium doping, *RSC advances*, 7 (2017) 17473-17479.
- [18] L. Iagher, L. Etgar, Effect of Cs on the stability and photovoltaic performance of 2D/3D perovskite-based solar cells, *ACS Energy Letters*, 3 (2018) 366-372.

- [19] C. Besleaga, L.E. Abramiuc, V. Stancu, A.G. Tomulescu, M. Sima, L. Trinca, N. Plugaru, L. Pintilie, G.A. Nemnes, M. Iliescu, Iodine migration and degradation of perovskite solar cells enhanced by metallic electrodes, *The journal of physical chemistry letters*, 7 (2016) 5168-5175.
- [20] T.L. Leung, Z. Ren, A.A. Syed, L. Grisanti, A.B. Djurišić, J. Popović, Photoinduced Segregation Behavior in 2D Mixed Halide Perovskite: Effects of Light and Heat, *ACS Energy Letters*, 7 (2022) 3500-3508.
- [21] G. Nagabhushana, R. Shivaramaiah, A. Navrotsky, Direct calorimetric verification of thermodynamic instability of lead halide hybrid perovskites, *Proceedings of the National Academy of Sciences*, 113 (2016) 7717-7721.
- [22] P. Singh, N.M. Ravindra, Temperature dependence of solar cell performance-an analysis, *Sol. Energy Mater. Sol. Cells*, 101 (2012) 36-45. 10.1016/j.solmat.2012.02.019
- [23] A.A.A. Al-Khazzar, Behavior of four Solar PV modules with temperature variation, *Int. J. Renew. Energy Res*, 6 (2016) 1091-1099.
- [24] A.J. Barker, A. Sadhanala, F. Deschler, M. Gandini, S.P. Senanayak, P.M. Pearce, E. Mosconi, A.J. Pearson, Y. Wu, A.R. Srimath Kandada, Defect-assisted photoinduced halide segregation in mixed-halide perovskite thin films, *ACS Energy Letters*, 2 (2017) 1416-1424.
- [25] S. Mahesh, J.M. Ball, R.D. Oliver, D.P. McMeekin, P.K. Nayak, M.B. Johnston, H.J. Snaith, Revealing the origin of voltage loss in mixed-halide perovskite solar cells, *Energy & Environmental Science*, 13 (2020) 258-267.
- [26] H.A. S. Sourabh, V. R. Whiteside, and M.C. Beard, I. R. Sellers, Evidence of Hot Carrier Extraction in Metal Halide Perovskite Solar Cells *Physical Review X* (under review) (2023).
- [27] H.S. Afshari, Shashi; Chacon, Sergio; Whiteside, Vincent; Penner, Rachel ; Rout, Bibhudutta; Kirmani, Ahmad; Luther, Joseph; Eperon, Giles; Sellers, Ian, FACsPb Triple Halide

Perovskite Solar Cells with Thermal Operation over 200 °C, ACS Energy Letters, Under review (2023).

[28] Y. Guo, X. Yin, D. Liu, J. Liu, C. Zhang, H. Xie, Y. Yang, W. Que, Photoinduced self-healing of halide segregation in mixed-halide perovskites, ACS Energy Letters, 6 (2021) 2502-2511.

[29] L. Hirst, M. Yakes, J. Warner, M. Bennett, K. Schmieder, R. Walters, P. Jenkins, Intrinsic radiation tolerance of ultra-thin GaAs solar cells, Applied Physics Letters, 109 (2016) 033908.

[30] A.D. Wright, C. Verdi, R.L. Milot, G.E. Eperon, M.A. Pérez-Osorio, H.J. Snaith, F. Giustino, M.B. Johnston, L.M. Herz, Electron–phonon coupling in hybrid lead halide perovskites, Nat. Commun., 7 (2016) 1-9. <https://doi.org/10.1038/ncomms11755>

[31] H.J. Jung, D. Kim, S. Kim, J. Park, V.P. Dravid, B. Shin, Stability of halide perovskite solar cell devices: in situ observation of oxygen diffusion under biasing, Advanced Materials, 30 (2018) 1802769.

[32] M.-c. Kim, N. Ahn, D. Cheng, M. Xu, S.-Y. Ham, X. Pan, S.J. Kim, Y. Luo, D.P. Fenning, D.H. Tan, Imaging real-time amorphization of hybrid perovskite solar cells under electrical biasing, ACS Energy Letters, 6 (2021) 3530-3537.

[33] L. Ma, D. Guo, M. Li, C. Wang, Z. Zhou, X. Zhao, F. Zhang, Z. Ao, Z. Nie, Temperature-Dependent Thermal Decomposition Pathway of Organic–Inorganic Halide Perovskite Materials, Chemistry of Materials, 31 (2019) 8515-8522. 10.1021/acs.chemmater.9b03190

[34] J. Zhou, J. Zhang, S. Chen, F. Zhao, L. Qiu, Z. Meng, L. Ding, B. Wang, Q. Pan, Comparative Thermal Research on Energetic Molecular Perovskite Structures, Molecules, 27 (2022) 805.

- [35] S. Kundu, T.L. Kelly, In situ studies of the degradation mechanisms of perovskite solar cells, *EcoMat*, 2 (2020) e12025.
- [36] X. Zhao, N.-G. Park, Stability issues on perovskite solar cells, in: *Photonics*, MDPI, 2015, pp. 1139-1151.
- [37] B. Conings, J. Drijkoningen, N. Gauquelin, A. Babayigit, J. D'Haen, L. D'Olieslaeger, A. Ethirajan, J. Verbeeck, J. Manca, E. Mosconi, Intrinsic thermal instability of methylammonium lead trihalide perovskite, *Advanced Energy Materials*, 5 (2015) 1500477.
- [38] A. Ciccioli, A. Latini, Thermodynamics and the intrinsic stability of lead halide perovskites $\text{CH}_3\text{NH}_3\text{PbX}_3$, *The journal of physical chemistry letters*, 9 (2018) 3756-3765.
- [39] A. Donakowski, D.W. Miller, N.C. Anderson, A. Ruth, E.M. Sanehira, J.J. Berry, M.D. Irwin, A. Rockett, K.X. Steirer, Improving photostability of cesium-doped formamidinium lead triiodide perovskite, *ACS Energy Letters*, 6 (2021) 574-580.
- [40] T. Moot, J.B. Patel, G. McAndrews, E.J. Wolf, D. Morales, I.E. Gould, B.A. Rosales, C.C. Boyd, L.M. Wheeler, P.A. Parilla, S.W. Johnston, L.T. Schelhas, M.D. McGehee, J.M. Luther, Temperature Coefficients of Perovskite Photovoltaics for Energy Yield Calculations, *ACS Energy Lett.*, 6 (2021) 2038–2047 <https://doi.org/10.1021/acseenergylett.1c00748>
- [41] S.P. Dunfield, D.T. Moore, T.R. Klein, D.M. Fabian, J.A. Christians, A.G. Dixon, B. Dou, S. Ardo, M.C. Beard, S.E. Shaheen, Curtailing perovskite processing limitations via lamination at the perovskite/perovskite interface, *ACS Energy Letters*, 3 (2018) 1192-1197.
- [42] A.R. Kirmani, D.P. Ostrowski, K.T. VanSant, T.A. Byers, R.C. Bramante, K.N. Heinselman, J. Tong, B. Stevens, W. Nemeth, K. Zhu, I.R. Sellers, B. Rout, J.M. Luther, Metal oxide barrier layers for terrestrial and space perovskite photovoltaics, *Nature Energy*, (2023). 10.1038/s41560-022-01189-1

Chapter 6

Radiation Tolerance of FACsPb(IBrCl)₃ Perovskite Solar Cells

The increased efficiency of mixed organic-inorganic lead halide perovskite solar cells (PSCs) has led to their considerable recent attention as a disruptive technology in photovoltaics (PV), with efficiencies reaching over 25% from single digit percentages 15 years ago [1]. Solution-based depositions used for fabrication of perovskites solar cells have proven to be defect tolerant, and potentially attractive for lowering production costs and increasing throughput. It has been shown that while mixed halide lead based PSCs have higher band gaps than ideal for single junction solar cells [2], they are appropriate for the wide bandgap or front junction of multijunction devices that could have a theoretical efficiency of 46% [3, 4]. Recent A-site cation substitutions have resulted in the state-of-the-art formamidinium-cesium compositions, improving halide segregation and preventing the use of the small and volatile organic cation methylammonium, which can lead to instability and decomposition [5-9]. Due to their potential to enhance power conversion efficiencies while maintaining a flexible architecture, tandem PSCs are attractive for remote power generation on unmanned aerial vehicles and spacecraft. Although perovskites have shown remarkable and consistent tolerance to proton irradiation [10-16], there are still many technical issues left unanswered such as, the effect of simultaneous irradiation and thermal stress, and stability of the cells in the various orbits and space environments.

Continuing the investigation of the suitability of the perovskite solar cells for space applications, this chapter focuses on the effect of irradiation on a subset of metal halide perovskites. The goal is to test perovskite solar cells in harsh radiation environments similar to those experienced in space. More than 90% of the radiation in space is in form of energetic electrons and protons, but

the lower energy proton irradiation is much more destructive to the electronic components of the satellites, such as solar panels, due to the significantly higher mass of protons as compared to electrons. The solar panels used on satellites are normally the largest area and outer most component causing them to receive the most exposure to radiation and damage. Figure 1(a) summarizes the different types of stresses imposed on the perovskite system in this study, which includes continuous and extended illumination, extreme thermal cycles, and high proton irradiation at various energies. A stopping and range of ions in matter (SRIM) simulation of the trajectory of the 75 keV protons incident on the perovskite cell is shown in Figure 1(b). SRIM simulations mimic how protons interact within the device stack to create high vacancy densities. This plot shows a uniform distribution of defects created throughout the whole perovskite layer. Typically, the irradiation tolerance and high-temperature performance of perovskite solar cells have been studied separately [14, 17-21]. However, in this work, the tolerance of the perovskite cells to both irradiation and extreme temperatures is assessed at the simultaneously, providing a more thorough investigating platform to assess the viability of this technology in practical space conditions.

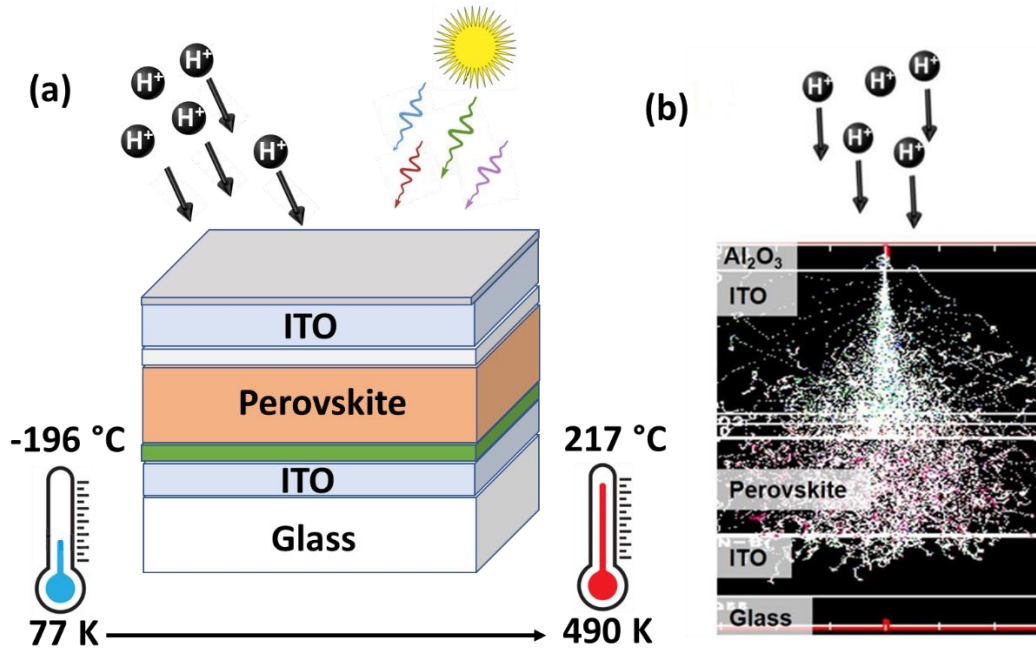


Figure 1. (a) Schematic of different types of stresses imposed on the solar cell. (b) A SRIM simulation of the trajectory of 75 keV protons in the perovskite solar cell showing a uniform distribution of defects created throughout the whole perovskite layer.

6.1 Proton Irradiation of the Solar Cells with Varied Energies and Fluences

Here, four perovskite solar cell samples underwent proton beam irradiation testing. The ion beam laboratory at the University of North Texas was responsible for performing the ion irradiation of these samples. Three of the samples were exposed to proton irradiation using different energies and fluences, including 75 keV and 10^{13} p/cm² (a flux of 3.3×10^{10} p/cm²s), 300 keV and 10^{14} p/cm² (a flux of 7.8×10^{10} p/cm²s), and 1 MeV and 4×10^{14} p/cm² (a flux of 7.8×10^{10} p/cm²s). The fourth sample was used as a traveler device to monitor changes in solar cell performance due to transit to and from the characterization and irradiation facilities. The selection of higher fluences for higher energy protons was intended to induce the same number of vacancies in the

absorber layer as low energy protons. This allows for more effective separation of the effects due to ionizing energy loss (IEL) and nuclear (non-ionizing energy loss: NIEL) mechanisms.

Figure 2 shows trajectory of protons inside the solar cell device as simulated by SRIM. As is seen in (a) in the case of 75 eV protons the particles mainly stop close to the absorber layer while protons with higher energies penetrate throughout the solar cell and reach the substrate (see Figure 2(b) 300 keV and (c) 1 MeV). In other words, the projected range of the protons is much higher for higher energy protons. Another point in these figures is that scattering events are much more pronounced for the case of 75 K eV protons while higher energy protons travel through the solar cell experiencing fewer scattering events.

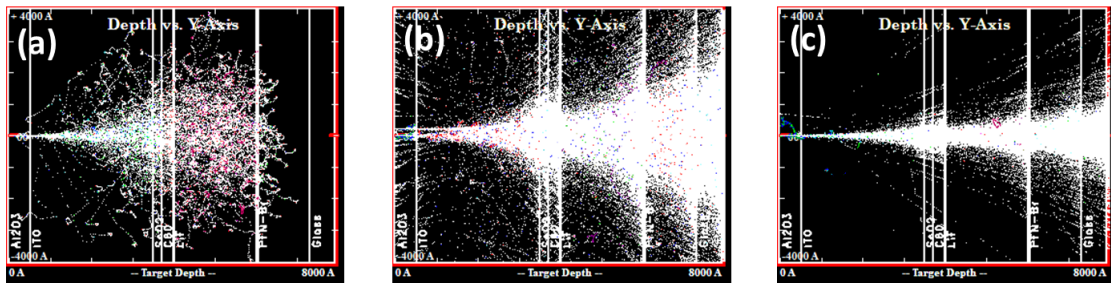


Figure 2. Trajectory of the protons with energy and fluences of (a) 75 keV: 10^{13} p/cm², (b) 300 keV: 10^{14} p/cm², and (c) 1 MeV: 4×10^{14} p/cm² in the perovskite solar cells.

This is consistent with previous research has demonstrated that protons with energies ranging from 50 keV to 1000 keV strongly interact with perovskite solar cells by stopping within them, while protons with energies greater than 1 MeV penetrate through the cell with fewer collisions with the target nuclei [22]. However, the energy values depend on the layer structure and thickness that high-energy protons encounter. In this study, high radiation fluences (above 10^{12} p/cm²) with varied energies were used to induce defects in the system and investigate the damage mechanisms, specifically, the role and effects of nuclear displacement (NIEL) and/or electron

ionization (IEL) in the PSCs under conditions that cause defects through these two different mechanisms. The goal was to induce the same total defect concentration in the absorber layer. The total number of vacancies in the absorber layer for the 75 keV, 300 keV, and 1 MeV irradiated cells, as determined by SRIM, are 1.95×10^{12} , 1.66×10^{12} , and 1.82×10^{12} , respectively (see Figure 3). As a result, equivalent defect concentrations were generated via different mechanisms (NEIL and IEL).

6.2 Elemental Analysis of the Irradiation Effect

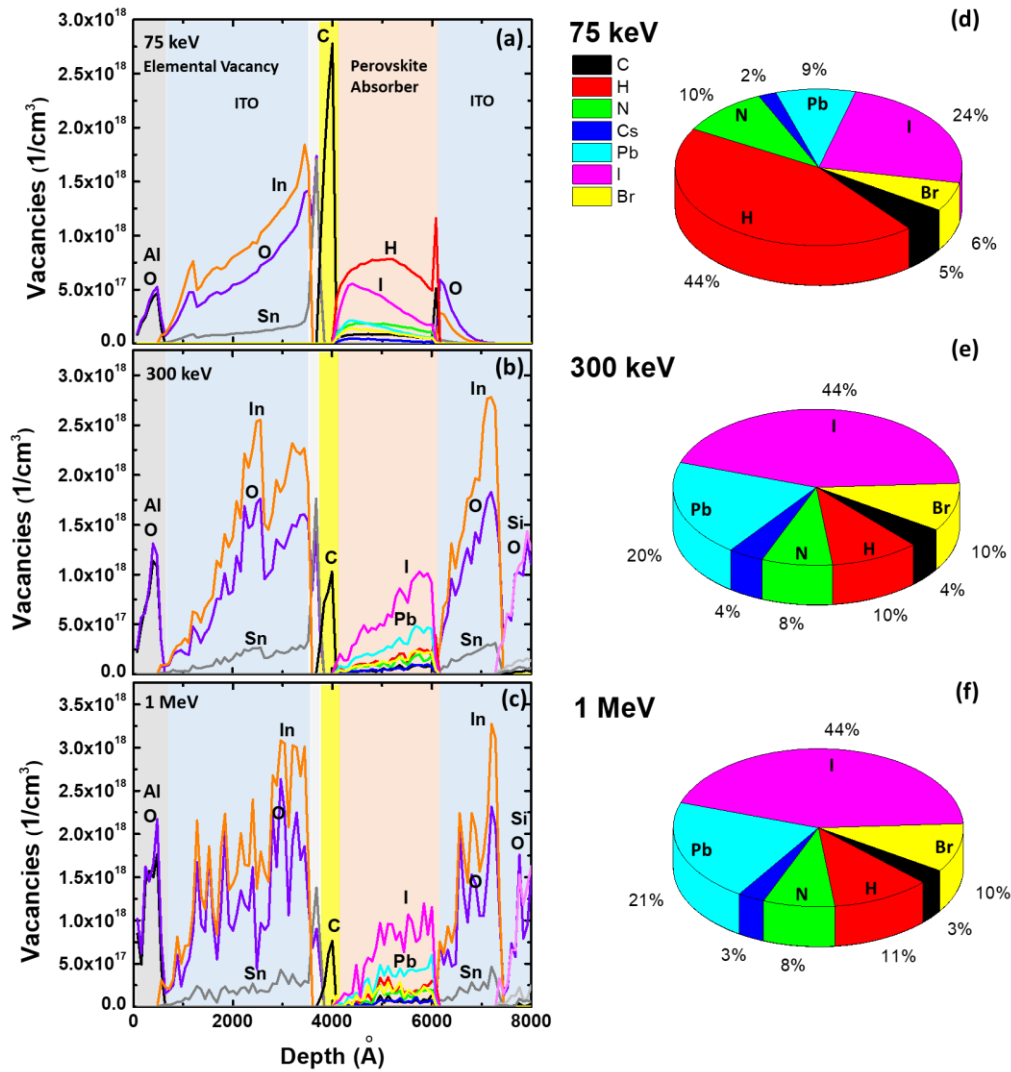


Figure 3. SRIM simulated estimation of the density of vacancies as a function of depth for energy and fluences of (a) 75 keV: 10^{13} p/cm², (b) 300 keV: 10^{14} p/cm², and (c) 1 MeV: 4×10^{14} p/cm². The elemental percentage of the vacancies in the absorber layer for each case is shown in figures (d), (e), and (f).

Figures 3 (a-c) show the density of vacancies for each element generated because of irradiation. The pie charts shown in Figure(s) 3 (d-f) present the percentage share of vacancies produced in each element with respect to the total number of vacancies produced in the absorber layer. The

protons at 75 keV lose their energy prior to reaching the end of the cell stop in the absorber (depicted in Figures 2(a) and 3(a)). On the other hand, protons with higher energy have a greater projected range and in the case of protons at 300 keV and 1 MeV pass through the solar cell. As they do so, they deposit a substantial amount of their energy near the glass substrate, inducing local heating and IEL throughout their trajectory. Regardless of the energy level simulated, the ITO layers are the most adversely affected by irradiation, which induces many In and O vacancies. Within the perovskite material itself, H atoms constitute the largest number of vacancies in the case of 75 keV irradiation (Figure 3), followed by halide-iodine atoms. At higher energies (300 keV and 1 MeV), iodine (I) vacancies are the most prevalent vacancies generated, followed by lead (Pb), as shown in Figures 3(d), (e), and (f), respectively.

The significant damage to the organic molecules induced by direct collisions (NIEL) within the perovskite are revealed by a prevalence of H vacancies under 75 keV irradiation (Figure 3). This high density of H vacancies at lower energies has been attributed previously to the abundance of hydrogen (H) in these lattices, its low displacement energy, and the fact that mass of H is nearly identical to that of a protons that irradiate the samples [22]. Previously [22], it was also observed that an increase in the energy of protons led to an increase in Pb-I vacancies as the protons increasingly interacted with the metal halide framework. This behavior is supported by the analysis presented here (Figure 3) [22].

6.3 Spectroscopic Analysis of the Effect of Irradiation

Spectroscopic measurements were conducted on both the traveler and irradiated samples, as depicted in Figure 4, to detect any changes in the samples after irradiation. The data was collected at a temperature of 4.2 K to enhance the resolution of the well-defined excitonic

complex and increase the likelihood of observing defect complexes in the absorption before thermal broadening and exciton ionization.

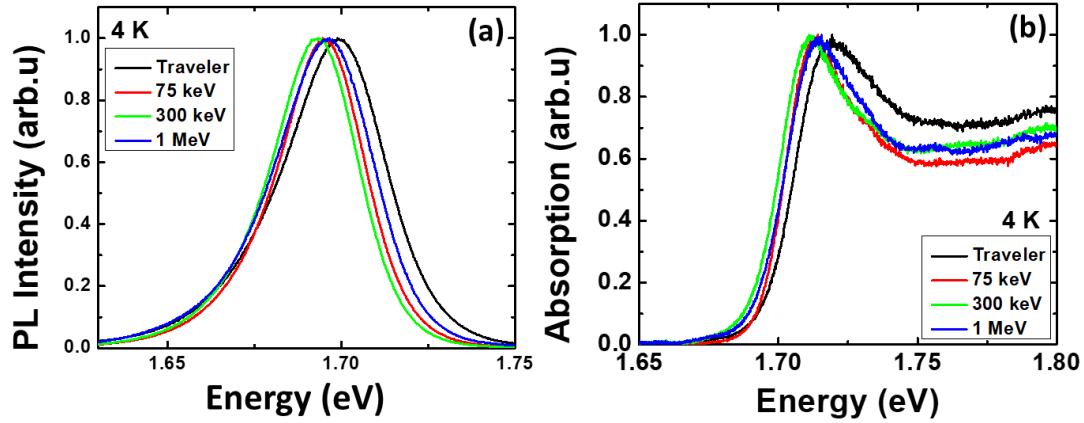


Figure 4. (a) Comparison of the normalized photoluminescence from the perovskite absorber in the solar cells at room temperature with increasing proton irradiation energy from traveler (black), 75 keV (red), 300 keV (green) and 1 MeV (blue) the black line is taken on the reference traveler cell. (b) Normalized absorption from the same devices assessed in (a) at the same irradiation levels at 4.2 K.

Additionally, temperature-dependent absorption and photoluminescence measurements were performed for all the cells showing no significant difference between pre and post irradiation. The black color shows the traveler which did not receive any irradiation and only traveled with the rest of the samples to monitor the effect of time and traveling on the cells. Red color is the result of proton irradiation with 75 keV, green color is 300 keV and blue color is 1 MeV. In Figure 4(a), the normalized photoluminescence of the cells at 4.2 K is compared, while Figure 4(b) shows the normalized absorption of the cells at the same temperature. Both the photoluminescence and absorption spectra demonstrate a redshift (~ 7 meV) after irradiation. This shift suggests that the band gap of the material has been slightly impacted by the displaced atoms, either through the localized relaxation of strain or subtle decomposition of the perovskite.

Figures 4(a) and (b) reveal that the redshift is more significant in the solar cell irradiated at 300 keV than in those irradiated at higher or lower fluences. The redshift for the lower 75 keV exposure and higher 1 MeV irradiated cells is identical. Considering the energies used one expects that the 75 keV shows the biggest redshift as it is in a regime which creates the most vacancies. But, since the higher energies 300 keV and 1 MeV have higher fluences as well the combined effect produces the observed outcomes.

6.4 Self-Healing of the Irradiation-Induced Defects in FACsPb(IBrCl)₃ Perovskite Solar Cells

Figure 5 illustrates the remaining factor, which represents the ratio between final value of a specific PV parameter (J_{sc} , V_{OC} , FF, or Eff) divided by its initial value measured from the FACsPb(IBrCl)₃ perovskite solar cells as a function of increasing proton energy and fluence at 1-Sun AM 1.5 at room temperature. Some examples of the J-V data for these measurements are also presented in Figure 6. It is clear Figure (6) that J-V responses are totally restored two months after irradiation. This illustrates the unique self-healing properties that result in perovskite solar cells [10, 12, 23, 24] when left unexposed at ambient temperatures for extended periods.

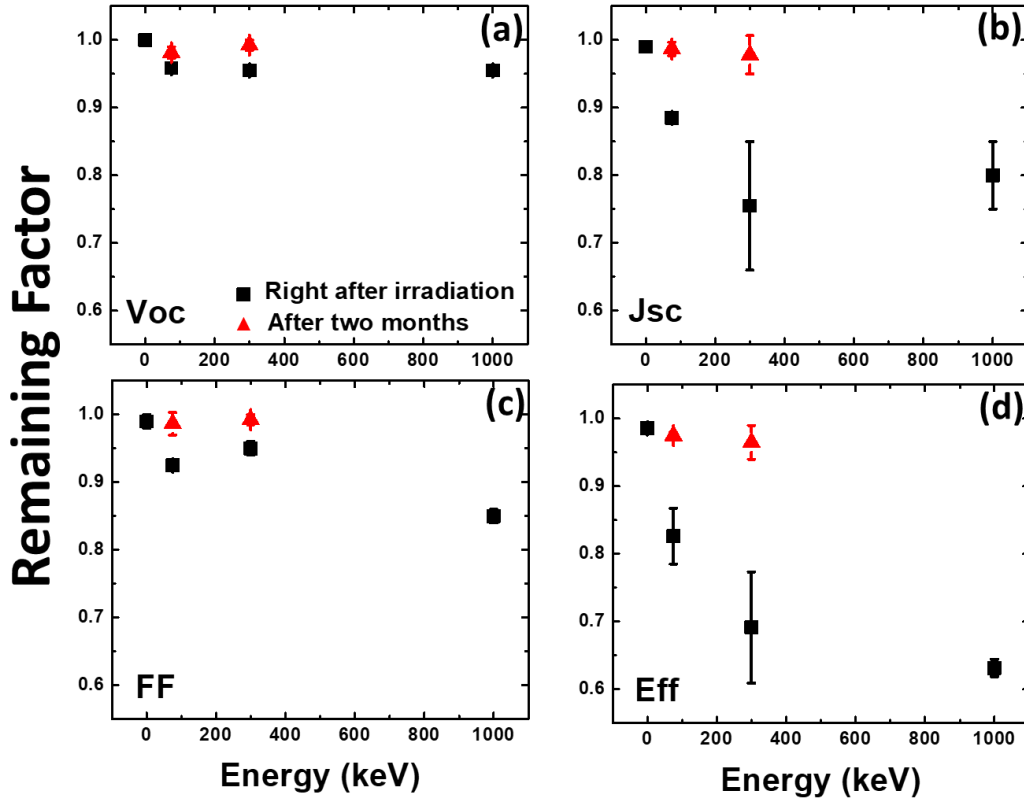


Figure 5. Remaining factors of PV parameters (a) V_{oc} , (b) J_{sc} , (c) FF, and (d) Efficiency (PCE) as a function of energy. The black squares show the remaining factors of the parameters right after irradiation. The red triangles show the results after two months kept in the dark. Multiple pixels were tested, and the bars present the distribution of the data for all pixels.

The post-irradiation data comprises two sets of measurements: (1) J-V parameters measured at room temperature immediately after irradiation (represented by black squares), and (2) the same parameters measured after two months stored in dark conditions (represented by red triangles). In Figure 5 the PV parameters are observed to degrade after irradiation (black symbols), and this degradation increases - as might be expected - with increasing energy and fluence, as shown in Figure 5. The J-V data measured immediately after irradiation exhibit more degradation when the solar cells are irradiated with higher energy and fluence protons (300 keV, 10^{14} p/cm², and 1 MeV, 4×10^{14} p/cm² conditions of energy and fluence), as evidenced by the results shown in

Figures 3 and 5. SRIM analysis indicates that these effects are due to significant generation of I and Pb related vacancies at high energy. Despite having a higher total number of vacancies, most of the vacancies observed in the 75 keV irradiated solar cell (Figure 3) are due to H displacement. As the organic molecules do not significantly impact the band gap or optical properties of the perovskite absorber [25], this solar cell exhibits the least degradation in its PV performance. Among the various irradiation energies evaluated, the solar cell exposed to 300 keV irradiation has the lowest J_{SC} (9.6 mA/cm²), but surprisingly, its fill factor (FF ~ 0.95) is superior to that of the 75 keV cell (FF ~ 0.92), See Figure 5.

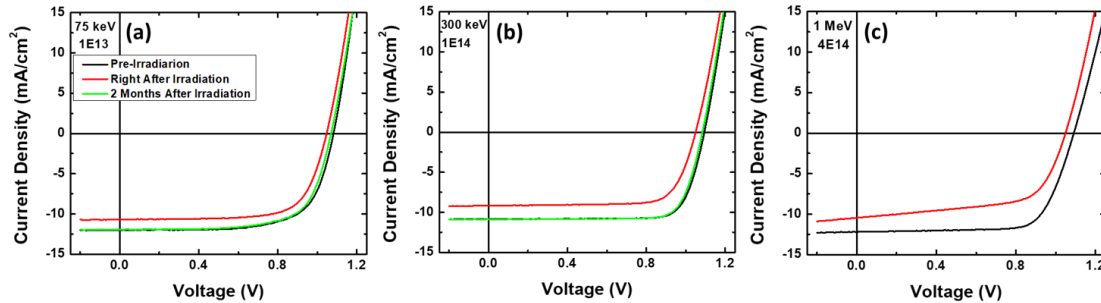


Figure 6. Light J-V plot of the solar cells irradiated with high energy protons. Irradiation conditions are (a) energy 75 keV and fluence of 10^{13} (b) energy of 300 keV and fluence of 10^{14} p/cm² (c) energy of 1 MeV and fluence of 4×10^{14} p/cm². The solar cells are measured pre-irradiation (black), right after irradiation (red), and two months after irradiation (green).

The origin of defects caused by proton irradiation, as well as the impact of NIEL and IEL processes, can be inferred from the properties of the affected materials. Perovskites have the ability to self-heal with increased energy and local heating, as observed by multiple authors [10, 12, 18]. As a result, perovskite systems have demonstrated enhanced performance in space testing protocols [26, 27] and have led to the creation of space-specific procedures for their use in power applications [22].

Figures 5 and 6 demonstrate that these systems possess the ability to self-heal and restore their initial levels of performance. The PV parameters shown in Figure 5, after a storage period of two months (solid red triangles), indicate that the solar cells regain their original performance levels for all cases except those subjected to an irradiation dose of 1 MeV: 4×10^{14} p/cm², which experienced complete loss of performance and prohibitive damage. These findings imply that despite their superior radiation tolerance, there exists a threshold beyond which irreversible damage occurs, indicating the need for the development of radiation-hard encapsulation systems for perovskite solar cells intended for long and/or harsh missions in space [28].

Upon closer examination, it is evident that the initial degradation of solar cell due to irradiation primarily affects the J_{sc} (and power conversion efficiency), with minimal impact on the V_{oc} (as shown in Figure 5). This suggests that the perovskite lattice or structure remains relatively unaffected by irradiation-induced changes such as through decomposition, segregation, or alterations to the band gap. Instead, the vacancies induced by proton exposure inhibit carrier extraction and transport, presumably by forming shallow traps or defect centers that localize carriers and reduce their diffusion length and mobility.

Despite the suggested carrier diffusion length of up to 1 μm for perovskites (much larger than the typical thickness of the absorber layer in perovskite solar cells, which is typically around 500 nm), shallow defects can result in significant localization and recombination losses upon irradiation. However, since here the V_{oc} remains relatively unaffected (see Figure 5a) by irradiation, these devices still appear to be dominated by radiative rather than non-radiative processes that are less prohibitive than defects typically induced in conventional III-V systems used in space. This is evident when assessing Figure 4 (a) and (b) which show the PL and absorption from the perovskite film in the irradiated solar cells is relatively unaffected by high

fluence irradiation. These results imply the losses in perovskite devices upon irradiation affect transporting layers and/or interfaces rather than the absorber material. This further underscores the novelty of perovskites and their potential for space applications.

6.5 Marginal Non-Radiative Recombination Centers Seen in the Dark J-V

Figure 7. presents the dark J-V data pre-irradiation (black), immediately after irradiation (green), and 2 months after irradiation (red) when stored in the dark. Immediately after irradiation the J-V response shows increase in the dark current levels reflecting the presence of irradiation induced defect states. Two months after irradiation graph clearly shows that the effect of such defects have been removed, as reflected in the much lower (very close to the pre-irradiation results) dark currents.

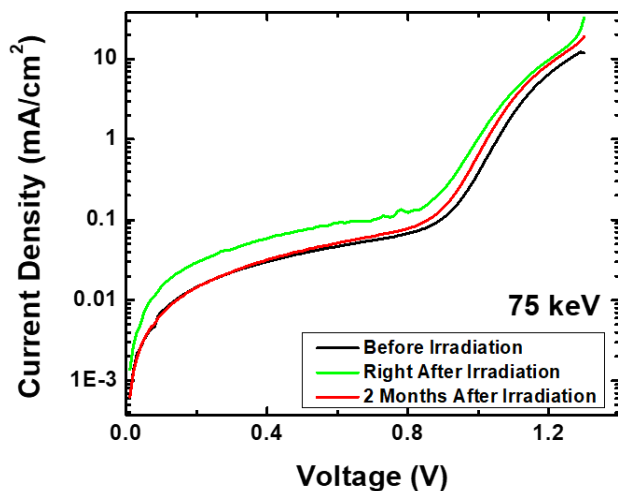


Figure 7. The dark J-V graph of a FACsPb(IBrCl)₃ perovskite solar cells pre-irradiation (black), right after irradiation (red), and two months after irradiation (green).

The soft and dynamic nature of the perovskites gives them the unique ability to self-heal and recover its performance over time. This is driven by ion motion and a low formation energy for the defect free material composition [29]. In this regard, some researchers suggest that irradiation

induced defect states should be considered temporary in the perovskite solar cells [29] unlike the III-V counterparts, which are typically prohibitively affected by stable mid gap defects upon radiation exposure [29]. The observations here, indicate that any defects that form in the lattice of the perovskite absorber are shallow and unstable, enabling the perovskite to return to its original state with minimal degradation. This finding is in line with the data presented in Figures 5 and 6, which suggest that defects induced in space environments are unstable and may even be eliminated as the temperature increases - or during dark periods - during the solar cells orbit in space. However, according to this set of data (Figure 5), it is important to note that irreversible degradation can occur if the threshold of more than 1 MeV and 10^{14} p/cm² is exceeded, although, more experiments and data are needed to further define and quantify this threshold. This level of radiation exposure is equivalent to one year at Jupiter for an unencapsulated solar cell, which is much higher than that experienced by conventional PV systems in typical low-earth-orbit (LEO) or international space station (ISS) orbits and therefore considerably higher than that experienced during a reasonable satellite lifetime.

6.6 A High Temperature Study of the Irradiated Solar Cells

An important point regarding any assessment/examination for practical applications is to expose the sample to all the involved factors, which entail radiation, environmental elements, high vacuum, lifetime etc. for the solar panels working at space it means creating the harsh environments and extreme temperatures simultaneously (experiments should actually include many cycles of extreme low and high temperatures). As usually the defect states are more activated at higher temperatures these protocols are necessary for practical space testing of the solar cells or any optoelectronic systems to be used in these environments. Figure 8 presents the temperature dependent light J-V data at 1-Sun AM0 of the FACsPb(I₂BrCl)₃ perovskite solar

cell, which had been irradiated with 75 keV protons at fluence 10^{13} p/cm². The measurement covers temperatures from 300 K to 440 K.

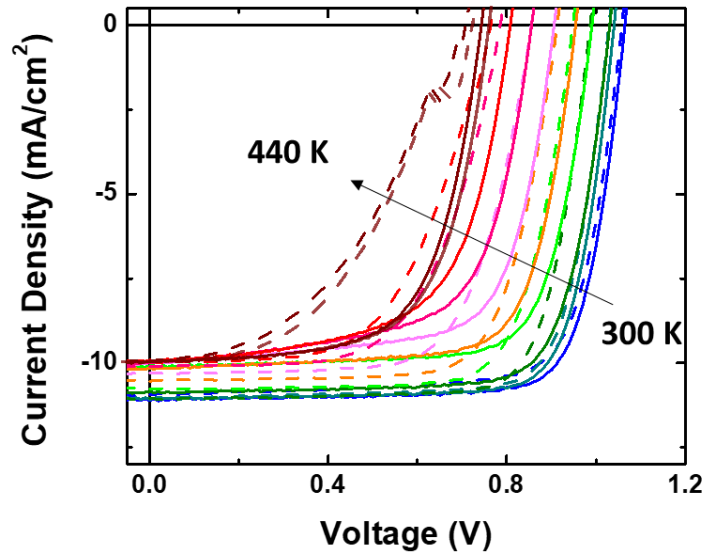


Figure 8. Temperature dependent light J-V plot of FACsPb(IBrCl)₃ solar cell irradiated with high energy protons. Irradiation conditions are 75 keV for energy and fluence of 10^{13} p/cm². The temperature spans from 300 K to 440 K. Solid and dash lines show results of reverse and forward scans respectively. Hysteresis is formed and increased at high temperatures, while low temperatures show almost no hysteresis.

It is very common in perovskite solar cells that the forward and reverse J-V scans don't lay on top of each other. Usually reverse J-V scans show better performance. The difference between the J-V results in forward and reverse scans in perovskite solar cells is known as hysteresis effect which is rooted in ion migration and charging and discharging of the interfaces and/or grain boundaries [30, 31]. More advanced perovskite solar cells do not show this behavior at least around room temperature which is the case for the cells studied here. As it is seen in Figure 8 while there is no hysteresis at 300 K, there is increasing hysteresis in the J-V which gets more pronounced at higher temperatures similar to the response of the non-irradiated cells discussed in

previous chapters. But here the PV parameters experience much higher degradation at high temperatures. Indeed, the solar cell is irreversibly damaged and stops working at the temperature of 440 K. As such, despite evidence of self-healing in low temperature higher irradiation environments, here the results show very high temperature can be prohibitive for perovskite PV performance presumably due to considerable material decomposition and subsequent defect generation. Again, however, it needs to be mentioned that the solar panels would not experience such high temperatures as 440 K (167 °C) in low earth orbits, or the outer planetary missions that the perovskites systems have been proposed for in space [16], and the high temperatures applied in this study were extreme upper limits to accelerate degradation and assess the stability of the solar cell performance, in general.

6.7 Thermal Activation of the Irradiation Induced Defects

Figure 9. provides a comparison of the high temperature performance of the pristine and irradiated FACsPb(IBrCl)₃ perovskite solar cells in terms of the remaining factor of the PV parameters.

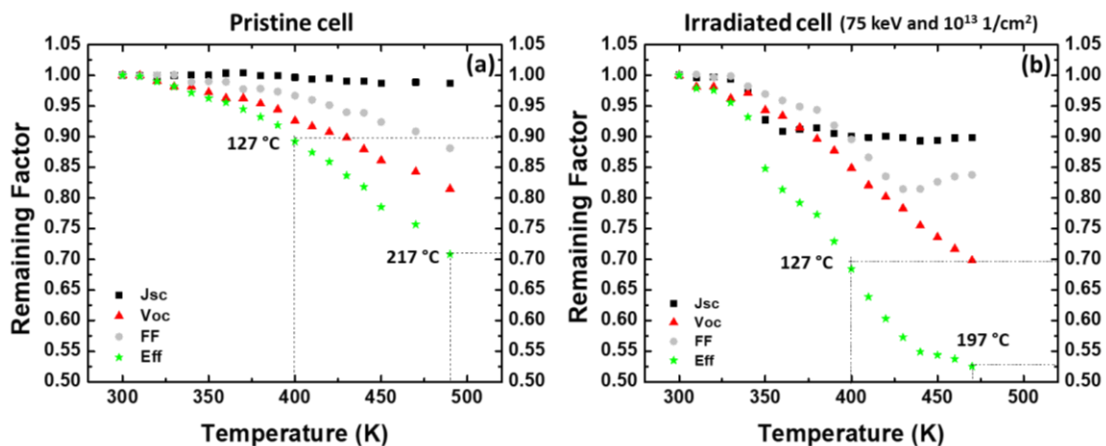


Figure 9. Comparison of the remaining factors of the PV parameters as a function of temperature for (a) the pristine FACsPb(IBrCl)₃ solar cell and (b) the solar cell irradiated with protons of 75 keV energy and fluence of 10¹³ p/cm².

As seen in Figure 9, J_{SC} is almost constant throughout the range of temperatures applied for the pristine solar cell and has a remaining factor of ~ 1 at 490 K. However, in the case of the irradiated cell the J_{SC} decreases with increasing temperature, reducing to a remaining factor of ~ 0.9 . Generally, the degradation of the PV parameters is much pronounced for the irradiated sample. At 127 °C the pristine cell continues to perform with 90% of the initial efficiency while the irradiated cell performs with 70% of its initial efficiency. At 217 °C the pristine cell performs with 70% of its initial efficiency and when returned to room temperature the efficiency is fully retained while the irradiated cell stops functioning at 167 °C permanently. These temperatures are very high when considering the practicality of these systems for space, or stability in general. Indeed, they represent the highest efficiency perovskite solar cell to date to perform at such high temperatures. This high temperature tolerance is rooted in the characteristics of the design of the cell: First, a double cation (FACs) composition is used, second, a transparent conductive back contact was used to eliminate metal migration or iodine-metal corrosion. Finally, a conformal atomic layer deposition (ALD) deposited alumina-based nanolaminate was used to prevent thermal decomposition via loss of volatile species.

6.8 Conclusions

Here, triple halide perovskite FACsPb(IBrCl)₃ solar cells were subjected to significant levels of radiation in space-like conditions, encompassing a range of proton energies (75 keV – 1 MeV) and high irradiation levels ($>10^{14}$ p/cm²). Proton irradiation has been found to cause an immediate reduction in the solar cell performance, but two months after this exposure when

stored in dark ambient conditions, the performance of the solar cell were seen to recover and that these systems have self-healing properties [10, 12, 32]. While this study further verifies the high radiation tolerance of perovskites discussed in the community, [23, 24] but it also highlights that irreversible damage can occur when the devices are exposed to 1 MeV protons at fluences of $> 3.9 \times 10^{14}$ p/cm². This level of exposure equates to $\sim 40,000$ years in orbit in the ISS or ~ 40 years on the JUNO orbit around Jupiter. The simultaneous effect of proton irradiation and extreme temperatures was also carried out to assess the multiple stresses more rigorously in space. These solar cells suffered degradation but at relatively high temperature of 167 °C demonstrating high tolerance for the system assessed. The exposure to high heat was observed to thermally activate defect states particularly at very high temperatures reducing the overall tolerance of the cells under these extreme conditions.

6.9 References

- [1] Laboratory, N. R. E. Research Cell Record Efficiency Chart. Best Research-Cell Efficiencies. html (accessed 3/15/2023). <https://www.nrel.gov/pv/cell-efficiency>
- [2] W. Shockley, H.J. Queisser, Detailed balance limit of efficiency of p-n junction solar cells, *Journal of applied physics*, 32 (1961) 510-519.
- [3] T. Leijtens, K.A. Bush, R. Prasanna, M.D. McGehee, Opportunities and challenges for tandem solar cells using metal halide perovskite semiconductors, *Nature Energy*, 3 (2018) 828-838.
- [4] M.T. Hörantner, T. Leijtens, M.E. Ziffer, G.E. Eperon, M.G. Christoforo, M.D. McGehee, H.J. Snaith, The potential of multijunction perovskite solar cells, *ACS Energy Letters*, 2 (2017) 2506-2513.

- [5] L. Shi, M.P. Bucknall, T.L. Young, M. Zhang, L. Hu, J. Bing, D.S. Lee, J. Kim, T. Wu, N. Takamure, Gas chromatography–mass spectrometry analyses of encapsulated stable perovskite solar cells, *Science*, 368 (2020) eaba2412.
- [6] D.P. McMeekin, G. Sadoughi, W. Rehman, G.E. Eperon, M. Saliba, M.T. Hörantner, A. Haghighirad, N. Sakai, L. Korte, B. Rech, A mixed-cation lead mixed-halide perovskite absorber for tandem solar cells, *Science*, 351 (2016) 151-155.
- [7] K.A. Bush, K. Frohna, R. Prasanna, R.E. Beal, T. Leijtens, S.A. Swifter, M.D. McGehee, Compositional engineering for efficient wide band gap perovskites with improved stability to photoinduced phase segregation, *ACS Energy Letters*, 3 (2018) 428-435.
- [8] A.J. Knight, J. Borchert, R.D. Oliver, J.B. Patel, P.G. Radaelli, H.J. Snaith, M.B. Johnston, L.M. Herz, Halide segregation in mixed-halide perovskites: influence of A-site cations, *ACS Energy Letters*, 6 (2021) 799-808.
- [9] A.J. Knight, L.M. Herz, Preventing phase segregation in mixed-halide perovskites: a perspective, *Energy & Environmental Science*, 13 (2020) 2024-2046.
- [10] F. Lang, N.H. Nickel, J. Bundesmann, S. Seidel, A. Denker, S. Albrecht, V.V. Brus, J. Rappich, B. Rech, G. Landi, Radiation Hardness and Self-Healing of Perovskite Solar Cells, *Adv. Mater.*, 28 (2016) 8726-8731. <https://doi.org/10.1002/adma.201603326>
- [11] V.V. Brus, F. Lang, J. Bundesmann, S. Seidel, A. Denker, B. Rech, G. Landi, H.C. Neitzert, J. Rappich, N.H. Nickel, Defect dynamics in proton irradiated $\text{CH}_3\text{NH}_3\text{PbI}_3$ perovskite solar cells, *Adv. Electron. Mater.*, 3 (2017) 1600438. <http://dx.doi.org/10.1002/aelms.201600438/full>
- [12] N.H. Nickel, F. Lang, V. Brus, J. Bundesmann, S. Seidel, A. Denker, S. Albrecht, G. Landi, H. Neitzert, Radiation hardness and self-healing of perovskite solar cells under proton irradiation

(Conference Presentation), in: Physics, Simulation, and Photonic Engineering of Photovoltaic Devices VII, SPIE, 2018, pp. 1052703.

[13] F. Lang, M. Jošt, J. Bundesmann, A. Denker, S. Albrecht, G. Landi, H.-C. Neitzert, J. Rappich, N.H. Nickel, Efficient minority carrier detrapping mediating the radiation hardness of triple-cation perovskite solar cells under proton irradiation, *Energy & Environmental Science*, 12 (2019) 1634-1647.

[14] F. Lang, M. Jošt, K. Frohna, E. Köhnen, A. Al-Ashouri, A.R. Bowman, T. Bertram, A.B. Morales-Vilches, D. Koushik, E.M. Tennyson, Proton Radiation Hardness of Perovskite Tandem Photovoltaics, *Joule*, (2020).

[15] S. Kanaya, G.M. Kim, M. Ikegami, T. Miyasaka, K. Suzuki, Y. Miyazawa, H. Toyota, K. Osonoe, T. Yamamoto, K. Hirose, Proton Irradiation Tolerance of High-Efficiency Perovskite Absorbers for Space Applications, *J. Phys. Chem. Lett.*, 10 (2019) 6990-6995. <https://doi.org/10.1021/acs.jpcllett.9b02665>

[16] Y. Miyazawa, M. Ikegami, H.-W. Chen, T. Ohshima, M. Imaizumi, K. Hirose, T. Miyasaka, Tolerance of Perovskite Solar Cell to High-Energy Particle Irradiations in Space Environment, *iScience*, 2 (2018) 148-155. <https://doi.org/10.1016/j.isci.2018.03.020>

[17] D. Hughes, S.M. Meroni, J. Barbé, D. Raptis, H.K. Lee, K.C. Heasman, F. Lang, T.M. Watson, W.C. Tsoi, Proton Radiation Hardness of Perovskite Solar Cells Utilizing a Mesoporous Carbon Electrode, (2021).

[18] B.K. Durant, H. Afshari, S. Singh, B. Rout, G.E. Eperon, I.R. Sellers, Tolerance of Perovskite Solar Cells to Targeted Proton Irradiation and Electronic Ionization Induced Healing, *ACS Energy Lett.*, 6 (2021) 2362-2368. <https://doi.org/10.1021/acsenerylett.1c00756>

- [19] Y. Zhou, Y. Yin, X. Zuo, L. Wang, T.-D. Li, Y. Xue, A. Subramanian, Y. Fang, Y. Guo, Z. Yang, Improving Thermal Stability of Perovskite Solar Cells by Suppressing Ion Migration Using Copolymer Grain Encapsulation, *Chemistry of Materials*, 33 (2021) 6120-6135.
- [20] M. Adil Afroz, N. Ghimire, K.M. Reza, B. Bahrami, R.S. Bobba, A. Gurung, A.H. Chowdhury, P.K. Iyer, Q. Qiao, Thermal stability and performance enhancement of perovskite solar cells through oxalic acid-induced perovskite formation, *ACS Applied Energy Materials*, 3 (2020) 2432-2439.
- [21] G. Niu, W. Li, J. Li, X. Liang, L. Wang, Enhancement of thermal stability for perovskite solar cells through cesium doping, *RSC advances*, 7 (2017) 17473-17479.
- [22] A.R. Kirmani, B.K. Durant, J. Grandidier, N.M. Haegel, M.D. Kelzenberg, Y.M. Lao, M.D. McGehee, L. McMillon-Brown, D.P. Ostrowski, T.J. Peshek, Countdown to perovskite space launch: Guidelines to performing relevant radiation-hardness experiments, *Joule*, (2022).
- [23] W. Nie, J.-C. Blancon, A.J. Neukirch, K. Appavoo, H. Tsai, M. Chhowalla, M.A. Alam, M.Y. Sfeir, C. Katan, J. Even, Light-activated photocurrent degradation and self-healing in perovskite solar cells, *Nature communications*, 7 (2016) 11574.
- [24] Y. Yu, F. Zhang, H. Yu, Self-healing perovskite solar cells, *Solar Energy*, 209 (2020) 408-414.
- [25] M.R. Filip, G.E. Eperon, H.J. Snaith, F. Giustino, Steric engineering of metal-halide perovskites with tunable optical band gaps, *Nature communications*, 5 (2014) 1-9.
- [26] S. Messenger, E. Burke, T. Morton, G. Summers, R. Walters, J. Warner, Modelling low energy proton radiation effects on solar cells, in: 3rd World Conference on Photovoltaic Energy Conversion, 2003. Proceedings of, IEEE, 2003, pp. 716-719.

- [27] S.R. Messenger, E.A. Burke, R.J. Walters, J.H. Warner, G.P. Summers, J.R. Lorentzen, T.L. Morton, S.J. Taylor, Quantifying low energy proton damage in multijunction solar cells, in: Proceedings of the 19th Space Photovoltaic Research and Technology Conference, 2007.
- [28] L. McMillon-Brown, K.M. Crowley, K.T. VanSant, T.J. Peshek, Prospects for Perovskites in Space, in: 2021 IEEE 48th Photovoltaic Specialists Conference (PVSC), IEEE, 2021, pp. 0222-0225.
- [29] Y. Rakita, I. Lubomirsky, D. Cahen, When defects become ‘dynamic’: halide perovskites: a new window on materials?, *Materials Horizons*, 6 (2019) 1297-1305.
- [30] C. Li, A. Guerrero, Y. Zhong, S. Huettner, Origins and mechanisms of hysteresis in organometal halide perovskites, *Journal of Physics: Condensed Matter*, 29 (2017) 193001.
- [31] P. Liu, W. Wang, S. Liu, H. Yang, Z. Shao, Fundamental understanding of photocurrent hysteresis in perovskite solar cells, *Advanced Energy Materials*, 9 (2019) 1803017.
- [32] Y. Guo, X. Yin, D. Liu, J. Liu, C. Zhang, H. Xie, Y. Yang, W. Que, Photoinduced self-healing of halide segregation in mixed-halide perovskites, *ACS Energy Letters*, 6 (2021) 2502-2511.

Summary and Outlook

In this dissertation multiple photovoltaic cells from three generations of solar cells were examined under harsh space conditions. Starting with the first-generation crystalline materials, the radiation tolerance of GaAs_{1-x}Sb_x-based solar cells was studied in various LILT conditions of the outer planets Saturn, Jupiter, and Mars. High radiation resistance was observed in photovoltaic parameters of the solar cells specifically for V_{OC} . Moreover, an unexpected improvement in the J_{SC} of the irradiated devices was observed at low temperatures, which translated in excellent performance for the solar cells measured in the environments of Saturn and Jupiter. Unlike the low temperature results, some loss of performance of the irradiated cell was observed at the higher temperature of Mars. These unusual effects at low temperatures were tentatively attributed to micro annealing of the cell upon electron irradiation.

Moving to the second generation of solar cells we studied the flexible thin film CIGS solar cells in LILT space conditions. At extreme low temperatures of the outer planets, high V_{OC} and improved fill factors improved the performance of the cell relative to terrestrial conditions. Although, evidence of a barrier to carrier collection was observed at low temperatures and ascribed to interfacial defect states and the doping contrast between the bulk CIGS and CdS window layer. The effect of this barrier is diminished with light soaking, as the system transitions from the so-called relaxed to metastable state. Also, at higher temperatures (> 200 K), the impact of this barrier to carrier extraction is reduced, as the thermal energy of carriers is increased.

Despite the existence of metastability and unintentional barrier at the CIGS/CdS interface in the CIGS systems, the low temperatures at the planetary conditions resulted in a considerably higher conversion efficiency. Moreover, concentrated illumination up to ~ 1 Sun AM0 further enhanced

the efficiency, for the temperatures of Jupiter (135 K) and Saturn (100 K), indicating effective carrier extraction under these conditions. Proton irradiation of the cells induced defect states mainly in the absorber layer reducing the minority carrier diffusion length, and lowering the shunt resistance in the system.

Moving to the third generation of solar cells we studied hybrid perovskite solar cells under space extreme conditions. Due to the strong presence of the excitons in the perovskite solar cells and their importance in opto-electric properties of the system a major project was defined related to the excitonic effects in perovskite solar cells which mainly are manifested at low temperatures. In this project the temperature dependence of PV parameters for triple cation perovskite $[\text{CS}_{0.05}\text{FA}_{0.79}\text{MA}_{0.16}\text{Pb}(\text{I}_{0.83}\text{Br}_{0.17})_3]$ solar cells was investigated focusing on the differences in performance at low and high temperatures. The signature of a barrier to carrier collection was observed at low temperatures, which resulted in a loss of performance at $T < 200$ K. The results of the intensity-dependent measurements indicate that collection of carriers at this interface barrier is limited by a combination of the exciton binding energy and thermionic emission. Low temperature loss of solar cell performance was observed to be directly correlated to an enhanced PL intensity, indicating inhibited carrier collection causes strong radiative recombination suggesting that these systems do not appear to be limited considerably by thermally activated non radiative processes. The presence of excitonic absorption in low-temperature EQE and the thermal quenching of this complex suggested binding energies of ~ 26 meV, for excitons.

In another project, several triple halide perovskite solar cells were exposed to extreme thermal stress ranging from -196 °C to 217 °C a range utilized to assess the stability of these systems in conditions relevant for ISS orbits, lunar missions, as well as for outer planetary conditions such as those at Jupiter, Saturn, and even for newly proposed missions to Neptune. At $T < 200$ K, the

PV parameters display unusual non-monotonic behavior that represents the various and competing contributions from non-ideal heterointerfaces, low thermal energy, and excitonic recombination in the perovskite absorber. Despite the unusual dynamics observed across the temperature cycle, the solar cells assessed retained their performance when returning to ambient conditions and even with some losses at high temperature *retained more than 90% of initial efficiency* at 400 K (127 °C).

In addition to high thermal stress, the samples were also exposed to high radiation dosages under space relevant conditions including: a range of proton energies (75 keV – 1 MeV) and high irradiation levels ($>10^{14}$ p/cm²). While proton irradiation led to a reduction in the performance of the solar cell immediately after irradiation, the performance of the solar cells was shown to recover two months after radiation exposure in dark ambient conditions. While this work confirmed the high radiation tolerance of perovskites, a threshold for irreversible damage was observed for 1 MeV protons at fluences of 4×10^{14} p/cm² – which represents exposure for ~ 40,000 years on the ISS orbit, or ~ 40 years at Jupiter (on the JUNO orbit).

List of Publications

Peer-reviewed Journal Papers

J1. H. Afshari, B. K. Durant, C. R. Brown, K. Hussain, D. Poplavskyy, B. Rout, I. R. Sellers, “The role of metastability and concentration on the performance of CIGS solar cells under Low-Intensity-Low-Temperature conditions”, *Solar Energy Materials & Solar Cells* 212 (2020) 110571.

J2. B. K. Durant, H. Afshari, S. Sourabh, V. Yeddu. M. T. Bamidele, S. Singh, B. Rout, G. E. Epron, D. YoungKim, I. R. Sellers, “Radiation stability of mixed tin-lead halide perovskites: Implications for space applications”, *Solar Energy Materials & Solar Cells* 230 (2021) 111232.

J3. B. K. Durant, H. Afshari, S. Singh, B. Rout, G. E. Epron, I. R. Sellers, “Tolerance of Perovskite Solar Cells to Targeted Proton Irradiation and electronic Ionization Induced Healing”, *ACS Energy Lett.* 2021, 6, 7, 2362-2368.

J4. H. Afshari, B. K. Durant; T. Thrasher, L. Abshire, V. R. Whiteside, S. Chan, D. Kim, S. Hatch, M. Tang, J. S. McNatt, H, Liu, M. R. McCartney, D. J. Smith I. R. Sellers, “Radiation Tolerance of GaAs_{1-x}Sb_x Solar Cells”, *Solar Energy Materials and Solar Cells*, 233, Article 111352.

J5. H. Afshari, B. K. Durant, A. R. Kirmani, S. A. Chacon, J. Mahoney, V. R. Whiteside, R. A. Scheidt, M. C. Beard, J. M. Luther, I. R. Sellers, Temperature-Dependent Carrier Extraction and the Effects of Excitons on Emission and Photovoltaic Performance in Cs_{0.05}FA_{0.79}MA_{0.16}Pb_{0.10}Br_{0.17} 3 Solar Cells, *ACS Applied Materials & Interfaces*, 14 (2022) 44358-44366.

J6. H. Afshari, S. Sourabh, S. A. Chacon, V. R. Whiteside, R. Penner, B. Rout, A. Kirmani, J. M. Luther, G. E. Eperon, I. R. Sellers, "FACsPb Triple Halide Perovskite Solar Cells with Thermal Operation over 200 °C", *ACS Energy Letters*, 2023, 8, 2408-2413.

J7. S. Sourabh, **H. Afshari**, V. R. Whiteside, and M.C. Beard, I. R. Sellers " Evidence of Hot Carrier Extraction in Metal Halide Perovskite Solar Cells ", Physical Review X, under review.

J8. S. A. Chacon, B. K. Durant, **H. Afshari**, T. A. Byers, B. Rout, V. R. Whiteside, D. Poplavskyy, and I. R. Sellers, "Probing the role of the interfacial properties of ACIGS with targeted proton irradiation", In preparation.

J9. **H. Afshari**, S. Sourabh, S. A. Chacon, V. R. Whiteside, R. Penner, B. Rout, A. Kirmani, J. M. Luther, G. E. Eperon, I. R. Sellers, "Proton-radiation tolerance and self-healing of FACsPb Triple Halide Perovskite Solar Cells ", In preparation.

Peer-reviewed Conference papers

C1. C. R. Brown, **H. Afshari**, V. R. Whiteside, D. Poplavskyy, K. Hossain, M. S. Dhoubhadel and I. R. Sellers, "Effect of Low-Intensity-Low-Temperature and High Radiation conditions on Flexible Cu(In,Ga)Se₂ Solar Cells", Conference: 2019 IEEE 46th Photovoltaic Specialists Conference (PVSC).

C2. **H. Afshari**, B. K. Durant, K. Hossain, D. Poplavskyy, B. Rout, and I. R. Sellers, "CIGS solar cells for outer planetary space applications: The effect of proton irradiation Conference: 2020 IEEE 47th Photovoltaic Specialists Conference (PVSC).

C3. **H. Ashfari**, B. K. Durant, T. Thrasher, L. Abshire, V. R. Whiteside, S. Chan, D. Kim, S. Hatch, M. Tang, J. S. McNatt, H. Liu, D. J. Smith and I. R. Sellers: Radiation tolerance of GaAs_{1-x}Sb_x solar cells: A candidate III-V system for space applications Conference: 2020 IEEE 48th Photovoltaic Specialists Conference (PVSC).

C4. N. P. Irvin, **H. Afshari**, C. Zhang, S. Murali, D. P. Petit, A. Chikhalkar, K. Hossain, C. T. Gregory, R. R. King, I. R. Sellers, C. B. Honsberg, “Annealing and Hydrogenation of GaNP Lattice Matched to Si”, Conference: 2021 IEEE 48th Photovoltaic Specialists Conference (PVSC).

C5. I. R. Sellers, **H. Afshari**, B. K. Durant, S. Sourabh, V. Yeddu, M. T. Bamidele, S. Singh, B. Rout, G. E. Eperon, D. Y. Kim, A. R. Kirmani, J. M. Luther, V. R. Whiteside, “The radiation tolerance, self-healing, and stability of perovskite solar cells” (Invited Paper), SPIE, Photonics West, 2022.

